# Variability Surveys in Astronomy

Vasily A. Belokurov
Keble College
University of Oxford

Trinity Term, 2003

Thesis submitted for the degree of Doctor of Philosophy at the University of Oxford

Theoretical Physics
1 Keble Road
Oxford, OX1 3NP

# Variability Surveys in Astronomy

## Abstract

Vasily Belokurov
Keble College

Doctor of Philosophy
Trinity Term 2003

To cope with the avalanche of data from future variability surveys it is essential to make object classification automatic. Conventional methods utilized by earlier optical transient searches such as MACHO lack flexibility and require vast computer time. I show how simple supervised learning algorithms can enhance greatly the lightcurve classification routine. I illustrate the advantages of the method with a number of examples and compare my results with those obtained using classical algorithms.

In the first two chapters of the thesis, I present a new method for lightcurve classification based on neural networks. I envisage that neural classifiers offer a superior way of detecting rare objects such as lightcurves of microlensed stars in big datasets (with a number of entries greater than a few hundreds of thousands). The power of the method is in the distributed processing of all available information. It is designed to reproduce complicated decision boundaries in many dimensions and so naturally the technique out-performs conventional selection procedures that approximate a decision boundary with a series of straight line cuts. Moreover, a trained network needs only a fraction of a second to yield the class membership for a large number of data patterns.

One example of such a survey is the Gaia space mission. Gaia will scan the entire sky, with the goal to compile the largest ever catalogue of stars in our Galaxy. Although directions at which Gaia will point its telescopes are pre-programmed, during the mission the light from numerous transient objects will be recorded and send to the ground. The concluding chapters of the thesis are concerned with the data-stream simulation of the Gaia satellite. The main contribution of this work is a detailed study of the microlensing and supernova signal available for Gaia. I generate both photometric and astrometric measurements. From the analysis of the dataset, I predict the detection rates and outline possible follow-up strategies.

*To Tatiana and Claudia*

# Acknowledgements

First of all, I would like to express my deepest gratitude to my supervisor Dr. Neil Wyn Evans for giving me the opportunity to work on the subject. I thank him for his invaluable insights, keen assistance and continuous encouragement throughout my DPhil years in Oxford. It has been fun to work under his supervision.

It is my pleasant duty to thank the Dulverton Fund for the financial support I received in the course of my studies. The staff of Keble College and Theoretical Physics was always there to back me up, that is why the three years in the University were so easy and so secure.

This thesis would have never been possible without the love and care I received from my family. You are my inspiration and my strength!!!

Many thanks to my colleagues in Theoretical Physics: Carole, Eric, Francesc, Graeme, James, Jonti, John, Simon, Stuart, Rachel, Ralf, Sarah, Wyn and Yann. These people made the atmosphere in the department truly friendly and stimulating. It was a pleasure to work side by side with Ralf Donner, whom I would like to thank for many interesting discussions and faultless proof-reading. I am lucky to have met and worked with Yann Le Du, the man with surely the largest brain on both sides of the Channel. I confess that I repeatedly exploited his great erudition and his ability to generate exciting ideas. He is the mastermind behind the neural networks project and the owner of the richest mine of French humour. I really enjoyed working with Martin Smith. Through this collaboration I learnt important things about gravitational microlensing and British music scene.

I am indebted to Michael Perryman who provided unceasing encouragement and support during my work on the applications for the Gaia mission.

I would like to say thank you so much to all my friends from Keble: Andrew, Blanca, Dil, Jess, Joanne, Leki, Matt, Michelle, Natalia, Nikola, Paul, Rob, Roland, Salvador, Sartaj, Steph, Thilo, Zuleikha and many others. With you around, my life in Oxford was sunny and cloudless. Special thanks to the people of DB Inc.: Sartaj, Nikola, Zu, Natalia, Blanca, Leki and Salvador. Thank you to my neighbours, Steph, Jess and Andrew and to my one and only president, Salvador Elias Venegas-Andraca. Thank you Henrik, I am proud to be your friend. Big big thanks to Carine Babusiaux for answering my endless queries about technical details related to Gaia. Thanks to the whole Gaia community. Thanks to Branden for sharing some of his buoyancy with me and for talking about things. Big thank you to Nazar, Pilar and Daniel for their warmth and hospitality. Thanks to Itai, Peter and Adrian for giving me a shelter. Thank you to Fermin for taking care of me when I needed it.

I want to thank my friends back home for I am amazed at their reluctance to give up on me. You are terrific, Slava, Lyudushka, Vera, Olga, Serge, Tony, Misha, Olenka, Vasily, Sergey, Lena, Katya, Menahim, Vika, Maya, Sergey Borisovich, Mikhail Evgenievich and all the “missing hearts”, Vitalya, Leshik, Yura, Slavik, Tanya, Sasha and Anya. Thank you to Vasily and Leshik for answering all my countless cries for help, you are real wizards.

I am happy to have extended my family to include two great guys, Leki and Nikola. Together with these two I went through the bright and the gloomy days of my DPhil in Oxford, mostly bright though, and for this I owe them a big one.

Finally, I thank Anna and Robert for providing me with a muse. She is my guiding star, she is the spin on my world and her name is Natàlia.

# Contents

# List of Figures

# List of Tables

# Chapter 1

# Introduction

This thesis is concerned with the study of rare transient events in massive astronomical surveys. A brief overview of the area of variability searches and related scientific returns is given in §1.1. Future ambitious projects concerned with optical variability are discussed in §1.2. Special attention is given to the Gaia mission (§1.3) since chapters 5 and 6 consider applications for this satellite. Microlensed stars and supernovae are particular examples of transient objects considered in detail in the thesis. Accordingly, §1.4 will review the basics of gravitational microlensing and §1.5 will describe the current status of supernovae hunt. Finally, §1.6 specifies the goals of the work presented here and explains the structure of the remainder of the thesis.

## 1.1 The era of terabyte astronomy

In the early years of the last decade of the last century a new epoch began in observational astronomy. This was the beginning of the era of massive optical variability searches. It was due to the gravitational microlensing experiments that some $10^5$ new variable stars were discovered. It was due to the *Hipparcos* space mission that fluxes and positions of some $10^5$ brightest stars were measured with unprecedented accuracy. Although completely different in their size, scope and cost, these projects faced and overcame the same problem – the necessity of processing millions of measurements in a short time. The rapid advances in CCD manufacturing, computer technology and space science made it possible for the valuable data to be recorded and reduced. However, the data analysis techniques have not evolved adequately and up to the present day a substantial part of the voluminous catalogues still remains unexplored.

The source of inspiration behind the gravitational microlensing searches was the idea of using the light deflection around massive heavenly bodies as a tool to study the mysterious dark matter. It was estimated that in order to catch a fleeting brightness increase caused by an intervening dark object it would be necessary to monitor millions of stars (Paczyński 1986). The Magellanic Clouds were chosen as the primary target with ample number of sources and lines of sight probing lenses in the Galactic halo. Another obvious location with a high source density was the bulge of the Milky Way. Thus, selected low extinction windows were monitored and faint stars in the disk and the bulge itself were counted upon to act as lenses. Typically, the stars were surveyed a few times every night over several years yielding $\sim 10^{10}$ photometric measurements. Three microlensing collaborations MACHO[1], EROS[2] and OGLE[3] reported the detection of the first candidate events in 1993, after just $\sim 2$ years of operation.

Ten years have passed but the bulk of the dark matter still has not revealed itself through gravitational microlensing. The majority of the candidate events seem to have been caused by ordinary stars. Microlensing surveys have told us a crucial fact about the Galactic dark halo: massive or otherwise, compact halo objects are ruled out as dark matter candidates (Milsztajn et al. 2000, Evans 2002). Many other important discoveries were made during the first microlensing decade and many branches of astrophysics

[1] http://wwwmacho.anu.edu.au/
[2] http://eros.in2p3.fr/
[3] http://sirius.astrouw.edu.pl/˜ogle/

benefited greatly from the survey data. Microlensing has matured as an astrophysical tool with the number of events growing from the original 3 announced in 1993 (Alcock et al. 1993, Aubourg et al. 1993, Udalski et al. 1993) to $\sim 1000$ known today. This dataset provided ample statistics to revise our knowledge of the structure of the Galaxy and its components.

Most microlensing events follow a simple form described by Paczyński in 1986. Such lightcurves can be identified using relatively straightforward procedures thanks to their featureless standard shape. It is due to the very same reason that they do not carry much information about the gravitational lens system (see §1.4). In order to estimate parameters of events one usually resorts to likelihood maximization, which implies building a model for the velocity and spatial distribution of lenses and sources. However, parameter extraction could be done in a much tidier way if we possessed so-called anomalous lightcurves. Distorted in one or another way, these lightcurves contain deviations which can be interpreted and fitted, thus allowing the lens parameters to be estimated (e.g. Gould 1992). At times, such deviations can be rather subtle and suppressed by noise. Then an early warning system has to be employed in order to start follow-up observations and resolve the fine structure of the lightcurve. In other instances, the distortions are so dramatic that the lightcurve does not look like typical microlensing anymore. Such a lightcurve will not be classified automatically, will not be included in the catalogue of gravitational microlensing candidates and as a result will be lost for further analysis.

As the microlensing 'rush' continued, it became more and more obvious that 'miners' were rewarded not only with a few grains of gold in the form of microlensing events, but also with tons of variable stars most of which were previously unknown. Numerous branches of stellar variability research were revived with a huge influx of data from MACHO, OGLE and EROS. Suddenly, the community was supplied with a great number of accurately measured and systematically calibrated samples of pulsating (Alcock et al. 1998), eruptive (Cieslinski 2003), exploding (Hardin et al.) and eclipsing (Rucinski

S. 1997) stars, quasars (Geha et al. 2003, Eyer L. 2002) and other types of objects. Some of the data still lies untouched regardless of the fact that it is open to public access. Some of it was eventually used in projects that provided new ways to measure interstellar extinction (Popowski, Cook & Becker 2003; Sumi 2003), constraints on the cosmic distance scale (Alcock et al. 1997, Groenewegen 2000), the age estimates of clusters, determination of the stellar luminosity and mass functions.

While the first microlensing collaborations monitored less than 1% of the optical sky, the telescope on board the *Hipparcos* satellite[4] scanned the entire celestial sphere recording information on all objects brighter than 12.4 magnitude. The original goal was to measure fundamental astrometric parameters - positions, parallaxes and proper motions of stars. These are the quantities vital for understanding of stellar properties and the structure of the Galaxy, however the angles involved are extremely small. The instruments had to be taken above the perturbing atmosphere, far from thermal and gravitational flexures to achieve the prerequisite high accuracy. The novel feature of this space telescope was the mirror combining the light from the two fields of view and thus achieving both large- and small-field measurements simultaneously. Therefore, it was ensured that a sufficient number of reference stars was always available for comparison. The satellite was designed to spin slowly, completing a full revolution in just over two hours. At the same time the axis of rotation was programmed to precess, in this way the telescope was able to scan the complete celestial sphere several times during its planned mission.

The telescope continually determined the relative positions of bright stars which appeared in its fields of view. Combined together, the measurements of relative angular separations made at many different orientations and at many different epochs yielded the path of a star across the sky. The *Hipparcos* ensemble of proper motions is the best available absolute set, free from systematic regional bias or global rotation (e.g.

[4]http://astro.estec.esa.nl/Hipparcos/

Binney 1997). These data were utilised for the study of local dynamics of the Galaxy, e.g. redetermination of the Sun velocity parameters (Dehnen & Binney 1998), revision of the structure and evolution of OB associations (e.g. Comeron, Torra & Gomez 1998), etc. *Hipparcos* vastly extended the sample of stars with accurately determined trigonometric parallaxes. For example, more than two hundred classical Cepheids were surveyed, making possible a new independent calibration of the Cepheid distance scale (e.g. Groenewegen & Oudmaijer 2000). A new form of variability was discovered with the detection of objects whose photo-centre undergoes position changes due to variations in unresolved brightness distribution (Wielen 1996).

Together with positional information, digitized photon counts were sent to the ground. For the first time, magnitudes of stars across the whole sky were measured with the same instrumental setup and observations were repeated on each star on numerous occasions throughout the mission. However, the scanning law, which was optimized to reach the most uniform astrometric solution, produced rather non-uniform time sampling. The total number of observations (or transits) per star depended mainly on the source ecliptic latitude. The basic time sampling of the *Hipparcos* mission can be viewed as a sequence of groups of transits with the smallest intervals of order of 20 minutes. These compact groups are usually separated by one month gaps. In total, $\sim$ 8000 variable stars were detected in spite of such an irregular coverage (e.g. Eyer et al. 1994, Grenon 1997, Koen & Eyer 2002). A still larger number could be reached if only follow-up observations from the ground had been fully exploited.

Today, it is likely that only a well coordinated joint effort by teams taking data from space and ground will lead to major discoveries. The very near future will see terabyte datasets of lightcurves routinely available to astronomers. These will include photometry collected by low cost robotic telescopes monitoring the entire observable sky several times every clear night (WASP, ROTSE, ASAS) together with the data of unprecedented quantity with sparse spatial or temporal sampling from the space missions

(Eddington, Gaia). There are crucial steps to be taken as soon as possible in order to maximize the scientific returns of the forthcoming surveys. First, powerful data mining techniques ought to be developed. This will lead to the introduction of real time alert systems in data processing pipelines and will allow integration of archives of present monitoring programs. The next step concerns the optimization of observing strategy and various follow-up schedules, which can only be done with detailed and realistic data stream modeling.

## 1.2 Future range of surveys

This section describes major ground-based and space-borne surveys that will be collecting optical data from the entire sky in the near future. As no detailed material is presented in this summary, the reader is referred to the surveys home-pages for further information.

As pointed out by Paczyński (2001), the most important achievement of the first massive variability searches was the development of hardware and software capable of handling hundreds of millions of measurements in (almost) real time. A number of variability projects was set up to capitalise on this progress. Most of them use cheap robotic instruments with modest apertures to image almost the whole sky every clear night or every few nights. Aside from the race for the faintest objects, these programmes aim to fill in the gap in our understanding of what is happening in the sky in real time. Although known and studied for thousands of years, the variability in the sky remains significantly under-explored. As judged by the number of entries in the General Catalog of Variable Stars, the majority of the types of variable objects lack completeness already at $\sim 10^{th}$ magnitude (Paczyński 1997). These include different classes of binaries, pulsating stars, novae, supernovae and a large diversity of optical flashes and flares. Complete catalogues of variable stars are vital for studies of galactic structure and stellar evolution. No discovery of a new kind of variability seems plausible without instant access to the database of previously detected and classified objects. It is envisaged, that in the coming decade such catalogues will be compiled (at least for the bright domain) with the data generated by the network of small automatic telescopes.

The Robotic Optical Transient Search Experiment (ROTSE[5]) is a set of instruments designed to search for optical flashes associated with Gamma-ray Bursts (GRB). The first ROTSE-I instrument began regular observations in 1998; the telescope had a combined field of view of $16° \times 16°$ degrees and monitored stars in the magnitude range 10.5-12.5. The ROTSE experiment has two principal observing modes: patrol mode and trigger response mode. Most of the time the telescope spends in the patrol mode, scanning the whole visible sky tiled with a set of $\sim$ 200 fields. When a GRB trigger arrives (once every ten days or so) ROTSE immediately interrupts patrol observing and obtains burst response data. Data acquisition is performed automatically as well as photometric and astrometric calibration. Exposures are taken in pairs to eliminate pollution by cosmic rays, etc. Paired measurements are also helpful for the variable star detection. At present, ROTSE identifies only periodic variables such as Cepheids, Binaries, Miras. The classification is done automatically using the technique of Welch & Stetson (1993). After the completion of the test phase, the ROTSE team (Akerlof et al. 2000) reported the discovery of $\sim$ 2000 variables. This is the result of analyzing $\sim$ 2000 square degrees of ROTSE patrol data (5.6 % of the total ROTSE-I sky coverage!); $\sim$ 90 per cent of the objects discovered are not included in the General Catalog of Variable Stars.

Another example of a fully robotic small aperture survey is the SuperWASP[6] project. SuperWASP is an ultra-wide angle photometric survey of stars in the magnitude range $\sim$ 7 to 17. The goal is to detect planetary transits and track Near-Earth Objects and optical transients. To assess the project capabilities the prototype instrument WASP0

[5]http://www.rotse.net/
[6]http://www.superwasp.org/

was built and tested (Kane et al. 2001). From the WASP0 dataset it is estimated that SuperWASP will be able to monitor 5,000 to 10,000 objects in each of its five $9.5^\circ \times 9.5^\circ$ fields of view. Every clear night, simultaneous photometry for up to 50,000 stars in a fixed set of fields will be recorded. The fields will be monitored continuously for 1-2 months before moving to the next set, yielding hundreds of measurements per star per night. The expected photometric precision is better than $\sim 1$ per cent for magnitudes $< 13$ and the expected data rate is $\sim 12$ terabyte per year. The useful by-products of the survey include accurate systematic studies of all classes of variable stars, detection of novae and supernovae, detection of near-Earth asteroids, supporting optical coverage of multi-wavelength satellite observations. Repeating shallow dips in the brightness of a star, i.e. planetary transits (e.g. Charbonneau 2002, Gould et al. 2002) have features in common with scarce events like microlensing and with classical periodic variables like binary stars. Being rare small-amplitude events usually overwhelmed by the variability of the maternal star, planetary transits are extremely tricky to spot. If transits of giant Jupiter-like planets can, in principle, be detected by ground-based surveys like SuperWASP, the more ambitious goal of detecting terrestrial planets can only be entrusted to a space-borne mission. In 2008, the Eddington[7] survey will start monitoring hundreds of thousands of stars in the range $V$=14–19 in order to detect planets in the "habitable zone". The satellite will carry a $\sim 0.6$ m$^2$ mirror size telescope, with a field of view of about 7 deg$^2$ and single-color CCD camera. The mission lifetime is five years, of which the first two are dedicated to astro-seismological observations in $\sim$ 20 preselected fields, while the following three years are dedicated to the observation of a single field, with the aim of detecting multiple transits from Earth-like planets. This way one mission will incorporate two scientific goals: to produce high quality astroseismic data necessary to understand physical processes that govern stellar evolution and, using this data, to detect and characterise habitable planets around other stars.

[7]http://sci.esa.int/home/eddington/

## 1.3 Gaia satellite

This section gives an overview of the key features of the Gaia mission as well as the description of the survey's main goals and additional scientific products. The complete study of the satellite, including technical design, mission performance assessment, data analysis and the science case can be found in survey's concept and technology study report (ESA 2000).

The Gaia astrometric mission[8] has been recently approved as one of the next two "cornerstones" of ESA's science programme and expected to be launched about 2010. Gaia will rely on the experience gained with the *Hipparcos* mission to create a precise three-dimensional map of one billion stars throughout Milky Way galaxy and beyond. This will be achieved by repeatedly measuring the positions of all objects down to $V = 20$. Objects like variable stars, supernovae, burst sources, microlensed events and minor planets will be detected on board and then cataloged on the ground. Final accuracies of 10 microarcseconds at 15 mag will provide distances to 10 per cent as far as the Galactic Centre. Combined with multi-band photometry and (limited) spectroscopy astrometric data will allow us to quantify the dynamical, chemical and star formation history of our Galaxy (Perryman et al. 2001).

The Gaia all-sky photometric survey will detect samples of variable stars of nearly all types, including detached eclipsing binaries, contact or semi-contact binaries, and pulsating stars. As pointed out in §1.2 existing samples are incomplete already at $V \sim 10$ mag. A complete sample of objects will allow determination of the rates of variable stars. A systematic variability search will also allow extensive study of stars in short-lived but key stages of stellar evolution, such as supernovae. It is crucial to devise a procedure for prompt detection of such objects as most of them are natural targets for the follow-up ground-based studies. Other contributions to extra-galactic astronomy include the

[8] http://astro.estec.esa.nl/gaia

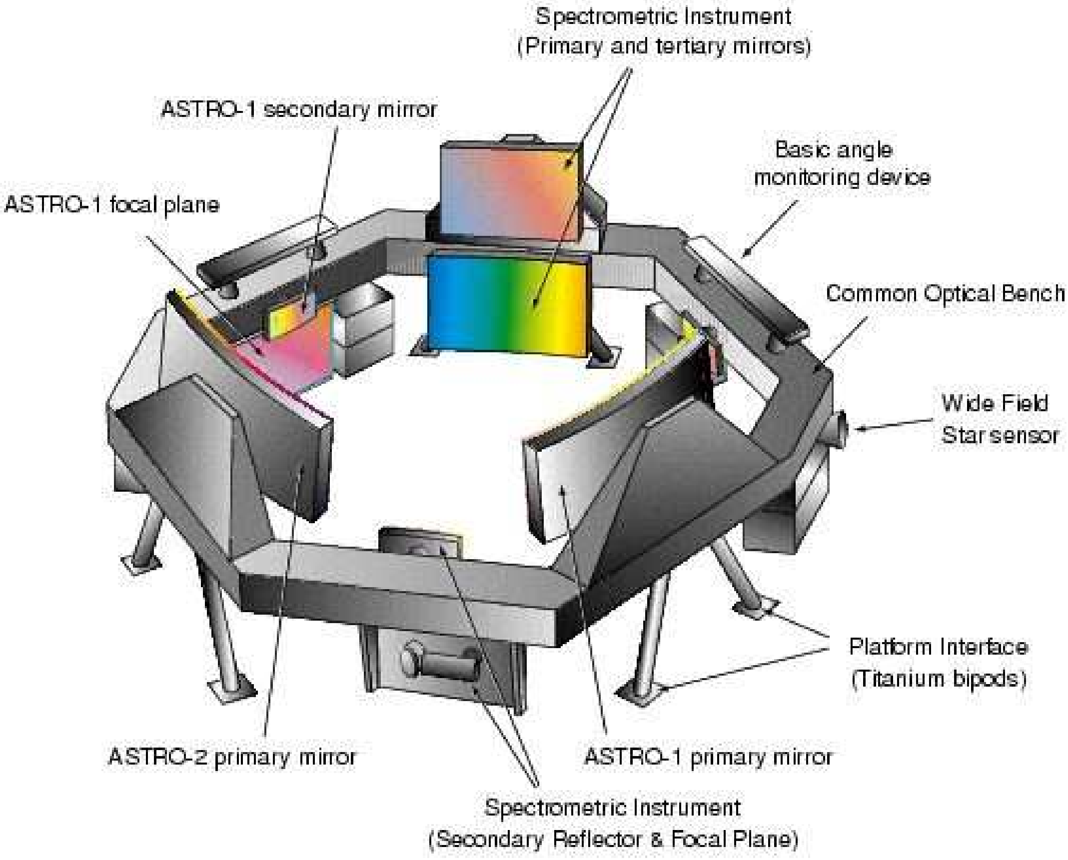


Figure 1.1: This shows Gaia's payload design. The satellite will carry two identical "Astro" instruments separated by 106° (ASTRO-1 and ASTRO-2) and a dedicated instrument for spectroscopic measurements.

structure, dynamics and stellar populations in the Local Group, a multi-colour survey of galaxies, studies of galactic nuclei and quasars. As it covers an enormous area of sky, Gaia will detect of order of $10^5$ new Solar System objects, including minor planets, Trojans, Kuiper Belt objects. Important parameters like masses, sizes, densities and albedos will be determined. The impressive astrometric capabilities of Gaia will be exploited for direct asteroid orbit determinations.

Gaia will be a continuously scanning spacecraft[9], measuring simultaneously the angular separations of thousands of star images as they pass across a field of view of about 1 $\mathrm{deg}^2$. The satellite rotates slowly on its spin axis, which itself precesses at a fixed angle to the Sun of 50°. The wide-angle measuring capability is provided by two viewing directions separated by 106° scanning the same great circle of the sky (see Fig 1.1). These are the two "Astro" instruments of Gaia, each comprising an all-reflective three-mirror telescope with an aperture of $1.7 \times 0.7\ \mathrm{m}^2$. Each astrometric field consists of an astrometric sky mapper, astrometric field proper and a broad-band photometer. Sky mappers will detect stars and measure their positions (as well as the satellite scan-speed). The astrometric parameters of stars are recovered from the time series of the one-dimensional transits distributed over the five year mission lifetime. The main astrometric field comprises an array of CCDs that will record the path of the detected star. Finally, the broad-band photometric field will provide multi-colour multi-epoch photometric measurements for each object observed in the astrometric field.

Additionally to the two "Astro" instruments, Gaia will carry a dedicated telescope for the radial velocity spectrometer and the medium-band photometer (Fig 1.1). This will be positioned mid-way between the two astrometric viewing directions. The radial velocity spectrometer will acquire spectra of all sufficiently bright sources ($\sim$ 17 mag). The medium band photometer includes two separate fields, on either side of the radial

[9]Please note that the specifics of the satellite design have changed slightly over the course of the past year. While Chapter 5 uses the original satellite scanning law, later work presented in Chapter 6 is based on the most up-to-date version.

spectrometer field, comprising a dedicated sky mapper and 11 medium spectral bands; the filters will be fixed directly onto the CCD array, which has properties similar to one of the "Astro" sky mappers.

The instrument design has evolved to match the required extraordinary precision; the payload was optimized to achieve the acquisition of radial velocities, the provision of accurate photometry and the on-board object detection. It is useful to summarize qualitatively why such a dramatic advance in astrometric accuracy over *Hipparcos* can be achieved. First, let us recall that the final accuracies are not simply given by the diffraction limit of optics, but defined by the precision on the determination of the image *centroid*. In other words, not only is it important to have as small a diffraction pattern as possible, but also it is important that the centre of this pattern can be positioned with good accuracy. Gaia's enlarged optics provides both a smaller diffraction pattern ($\lambda/D \sim 70$ mas in the scan direction) and a significantly larger collecting area (by more than a factor of 30). Together with pumped-up quantum efficiency and increased bandwidth of the detector, it contributes to improved photon statistics, significantly extending the limiting magnitude as well as the precision of the individual centroiding measurements. The total gain in parallax accuracy comprises many other factors and sums up to $\sim 150$, i.e. the parallax of a star of $15^{th}$ magnitude will be measured by Gaia with the accuracy of 10 $\mu$as, compared to 1.5 mas for $10^{th}$ magnitude star observed by *Hipparcos* (note that stars of different magnitude are compared since Gaia is optimized to observe much fainter stars than *Hipparcos*).

For essentially every application of the Gaia astrometric data, high-quality photometry will be crucial. Constraints on the photometric precision come from the specifics of stellar classification scheme. The distribution function of stellar abundances must be determined to $\sim 0.2$ dex, while the effective temperatures must be determined to $\sim$ 200 K. These requirements translate into a magnitude accuracy of $\simeq 0.02$ mag for each colour index. An optimum baseline photometric system was designed with four broad

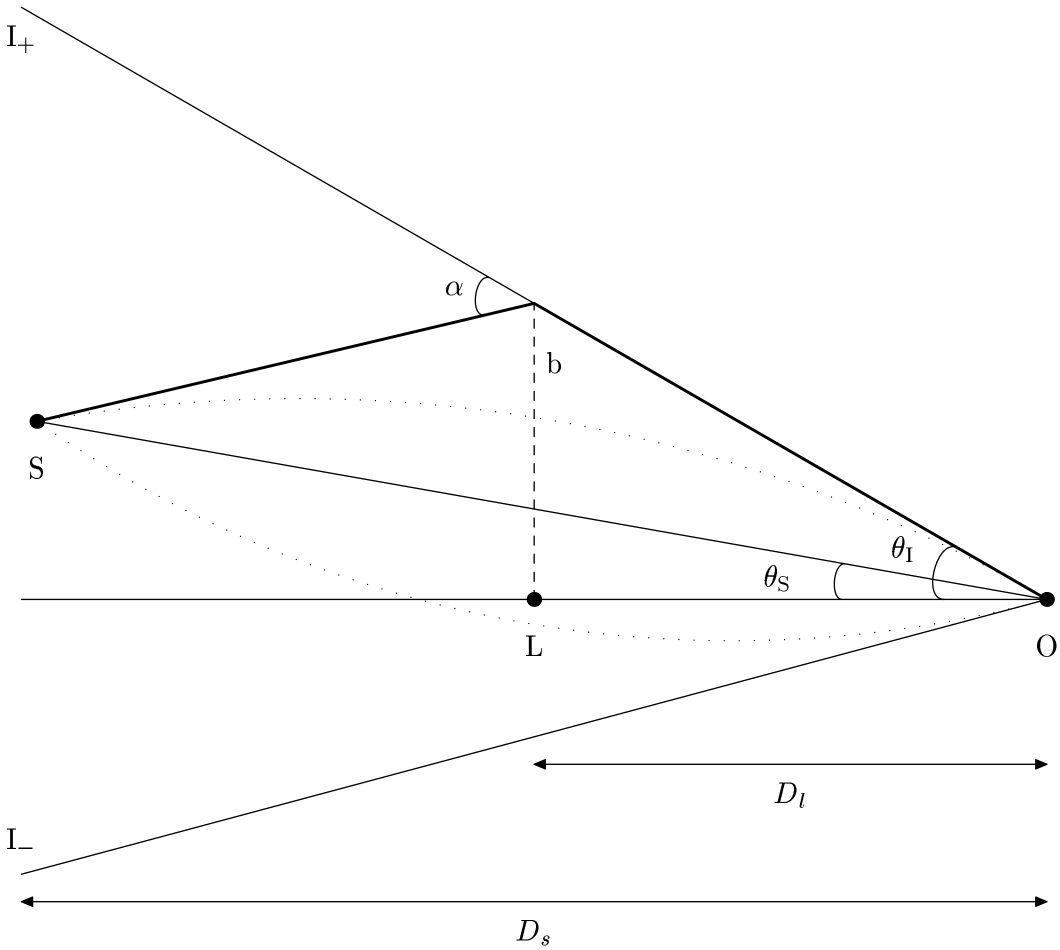


Figure 1.2: This shows the geometry of a gravitational lens system. The source (S) is at distance $D_s$ from the observer (O) and the lens is located at distance $D_l$. The observer sees two micro-images ($I_\pm$) at angular distance $\theta_I$ from the lens.

and eleven medium passbands, covering the near ultraviolet to the CCD red limit.

## 1.4 Gravitational microlensing

This section briefly summarizes the basics of gravitational microlensing. For a broader view of the field of gravitational lensing the following monographs are available: Schneider, Ehlers & Falco (1992), Mollerach & Roulet (2002). A more in-depth analysis of gravitational microlensing can be found in Paczyński (1986, 1996) and in Evans (2003).

Suppose a massive object (a dark star) is passing close to the line of sight between the source of light and the observer. This gravitating body will act like a lens bending the paths of the photons within its vicinity. A gravitational lens differs from an ordinary glass lens as it has a different "focal point" for each ray of light grazing at different impact parameter. The General Theory of Relativity predicts that the photons at distance $b$ from a mass $M$ will be deflected by (see for example Landau & Lifshitz 1971, section 98):

$$\alpha = \frac{4GM}{bc^2} \tag{1.1}$$

Note, that there is no dependence on the wavelength of radiation – gravitational lensing is achromatic. Let us assume that the source (S) and the lens (L) are point-like objects that are located respectively at $D_{\mathrm{s}}$ and $D_{\mathrm{l}}$ distance from the observer (O). In the general case, there will appear two images $I_{\pm}$ corresponding to two possible photon trajectories on either side of the lens (Figure 1.2). In an event of perfect alignment, the observer will see a bright ring with radius $r_{\mathrm{E}}$ given by

$$r_{\mathrm{E}}^2 = \frac{4GM}{c^2}\frac{D_{\mathrm{l}}(D_{\mathrm{s}} - D_{\mathrm{l}})}{D_{\mathrm{s}}} \tag{1.2}$$

The Einstein radius, as specified above, defines the amount of lensing in the system. Given its angular measure $\theta_{\mathrm{E}} = r_{\mathrm{E}}/D_{\mathrm{l}}$ it is possible to deduce the distance between the lens and the images $\theta_{\mathrm{I}}$. For a source at $\theta_{\mathrm{S}}$ angular distance from the lens, we have:

$$\frac{\theta_{\mathrm{I}}}{\theta_{\mathrm{E}}} = \frac{\sqrt{u^2+4} \pm u}{2} \tag{1.3}$$

where $u$ is normalized source position, i.e. $u = \theta_{\mathrm{S}}/\theta_{\mathrm{E}}$. For typical sources and lenses in our Galaxy, the angular separation between the images is of order of milliarcsecond. Although the images can not be resolved, changes in the total brightness and displacements of the photocentre can, in principle, be detected. The closer the lens is to the line of sight, the larger is the area taken by the two images. The relative increase in the observed source area is:

$$A = \sum \frac{\partial(\theta_{\rm I})}{\partial(\theta_{\rm S})} = \frac{u^2 + 2}{u\sqrt{u^2+4}} \tag{1.4}$$

Since the surface brightness is preserved in gravitational lensing the above ratio defines the amplification factor of the lens. If the source, the lens and the observer are all set to move linearly, then $u^2(t) = u_0^2 + (t - t_0)^2/t_{\rm E}^2$, where $u_0$ is the distance between the source and the lens at closest approach, $t_0$ is the time when it happens and $t_{\rm E}$ is the Einstein time defined as

$$t_{\rm E} = \frac{\theta_{\rm E}}{\mu_{\rm rel}}, \qquad \mu_{\rm rel} = \mu_{\rm L} - \mu_{\rm S}. \tag{1.5}$$

Here, $\mu_{\rm rel}$ is the relative proper motion of the lens. Equations 1.4 and 1.5 define the typical photometric behavior of the microlensed star. Observationally, microlensing events are limited to the ones with amplification $A > 1.34$. This is a convention that utilizes the fact that the source at the distance $u = 1$ from the lens will be magnified by a factor $3/\sqrt{5} \approx 1.34$. Microlensing lightcurves, as in the Figure 1.3, were first presented in Paczyński (1986), where also the probability that the source is magnified by more than 1.34 at any given time was deduced. This probability is proportional to the density of lenses along the line of sight and is commonly referred to as the microlensing optical depth.

Theoretically, the microlensing optical depth provides an estimate of the mass density in the Galaxy. Moreover, measured at different galactic locations it allows us to study the structure of the Milky Way. Practically, the optical depth and all subsequent inferences rest on the efficiency of the event detection. The difficulty is that the rare microlensing events are hugely out-numbered by the much more common stellar variables. The numbers of events quoted by different microlensing collaborations do not seem to agree either with the current models of the Galaxy or between each other. In order that microlensing surveys achieve their true status as the most powerful probe of galactic structure, the identification problem will need to be much more thoroughly understood

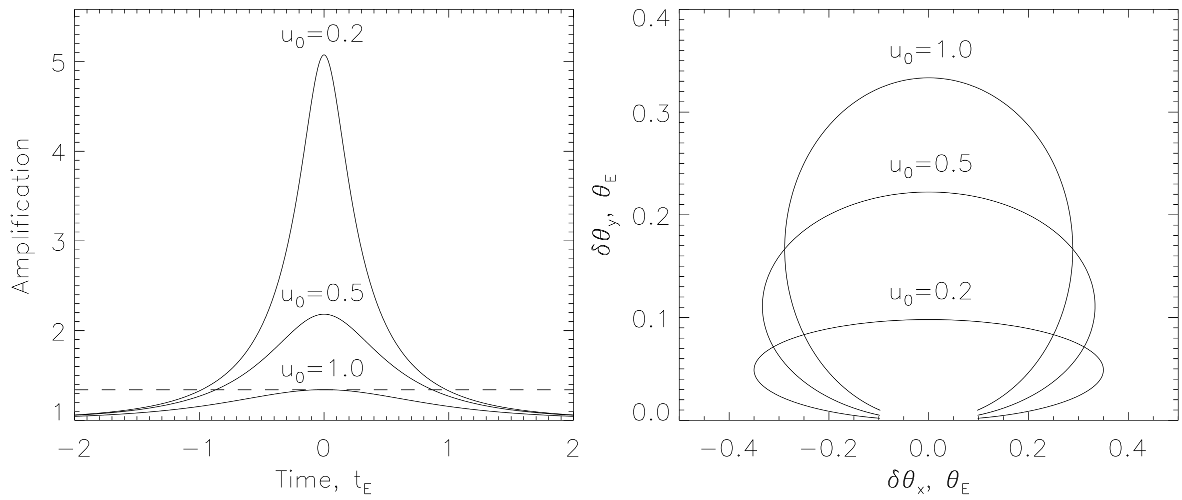


Figure 1.3: Left panel: This shows amplification during gravitational microlensing in the standard (Paczyński) model for different impact parameters $u_0$ for encounter times $-2t_{\mathrm{E}} < t < 2t_{\mathrm{E}}$. Dashed line marks the amplification of $\sim 1.34$ corresponding to impact parameter $u_0 = 1$. Right panel: This shows the trajectories of the light centroid during gravitational microlensing for different impact parameters $u_0$. Components of the centroid shift $\theta_{\mathrm{x}}$ and $\theta_{\mathrm{y}}$ are given in fractions of angular Einstein radius $\theta_{\mathrm{E}}$. Note that now the encounter times span a larger range: $-10t_{\mathrm{E}} < t < 10t_{\mathrm{E}}$.

than at present.

Suppose we have detected a microlensing event, what information can we extract from it? A standard procedure would be to fit the lightcurve with a Paczyński model. Of all four parameters, namely $u_0$, $t_0$, $t_{\mathrm{E}}$ and the baseline flux, only the Einstein time carries any physical information. In fact, it contains *all* the information about the gravitational lens system, but in a mixed up non-linear way:

$$t_{\mathrm{E}} = \frac{1}{v}\sqrt{\frac{4GMD_{\mathrm{l}}(D_{\mathrm{s}} - D_{\mathrm{l}})}{c^2 D_{\mathrm{s}}}} \tag{1.6}$$

where $v$ is relative transverse velocity between source and lens projected onto the lens plane

$$v = v_{\mathrm{L}} - v_{\mathrm{O}} - (v_{\mathrm{S}} - v_{\mathrm{O}})\frac{D_{\mathrm{l}}}{D_{\mathrm{s}}} \tag{1.7}$$

Consequently, before, for example, the mass of the lens can be determined, the spatial and velocity distributions of sources and lenses have to be modeled.

However, if the event is observed astrometrically as well as photometrically, then two additional measurements can be performed. As shown by Boden, Shao & van Buren (1998) the photocentre of the two unresolved microlensing images will be displaced from the actual source position by

$$\delta\theta = \theta_{\rm E} \frac{u}{u^2 + 2} \tag{1.8}$$

In the model of rectilinear motion the centre of light traces an ellipse with the size of the axes proportional to the angular Einstein radius $\theta_{\rm E}$ (see Figure 1.3). The major axis is aligned with the direction of the lens motion. Hence, both $\theta_{\rm E}$ and the angle of source-lens relative proper motion $\phi$ can be obtained.

Both photometric and astrometric signals are sensitive to the parallactic distortions caused by motion of the Earth about the Sun. The magnitude of the parallactic perturbation is related to the size of the Einstein ring projected onto the observer's plane $\tilde{r}_{\rm E} = r_{\rm E} D_{\rm s}/(D_{\rm s} - D_{\rm l})$. By fitting the microlensing lightcurve with a parallactic model, one can deduce a value for $\tilde{r}_{\rm E}$ and, hence, infer the mass of the lens:

$$M = \frac{c^2}{4G} \frac{\tilde{r}_{\rm E}}{\pi_{\rm rel}} \tag{1.9}$$

using some reasonable assumption about the relative source-lens parallax $\pi_{\rm rel} = 1/D_{\rm l} - 1/D_{\rm s}$. Remarkably, astrometric observations give both $\theta_{\rm E}$ and $\tilde{r}_{\rm E}$ and thus allow a *direct* estimate of all physical parameters for the lens.

## 1.5 Supernovae

This section provides a short introduction to supernova research, including the classification of supernova types, important observational characteristics and their interpretations. There are many reviews on supernova available (e.g. Leibundgut 2000, Wheeler 2003, Turatto 2003, Hamuy 2003).

Supernovae have been observed for many centuries, but recent years have seen a major increase in reliable supernova data. A number of dedicated searches were inspired by the discovery of SN 1987A. In the last decade, the interest in supernovae has risen yet further with their applications to cosmological problems. While the original experiments (e.g. Zwicky 1965) detected only a dozen supernovae each year, at present $\sim 200$ are detected yearly. Currently, data are collected in a systematic way at several places. One example is the Lick Observatory Supernovae Search conducted by the Katzman Automatic Imaging Telescope (Filippenko et al. 2001). This robotic telescope scans about 1,000 galaxies a night, the new points of light are checked by a team of undergraduate students and the objects confirmed are then followed in $BVRI$ and with spectroscopy.

The wealth of newly detected objects has revealed an increasing number of peculiar supernovae (Li, Filippenko & Treffers 2001). The uniform picture of a decade ago is breaking up into several correlations which connect maximum luminosity, lightcurve shape, spectral appearance and host galaxy morphology. Today, it is evident that at least two main classes of supernova exist. The classification originally based on observed spectral features has proven to identify physically different objects. SNe Ia are thermonuclear explosions in white dwarf stars which have accreted too much matter from a companion. It is unclear whether the companion is also a white dwarf or is a main-sequence/red-giant star. In fact, whether the progenitors of SNe Ia are doubly-degenerate or singly-degenerate binaries is one of the major unsolved problems in the subject. The spectra of type Ia supernovae are characterized by the complete absence of hydrogen and helium lines. On the contrary, SNe II all prominently exhibit hydrogen in their spectra and are believed to originate in the core collapse of massive stars. SNe Ia possess homogeneous lightcurves and spectra, while lightcurves and spectra of supernovae type II are heterogeneous. SNe Ia can be found in galaxies of all Hubble types, including ellipticals, with no evidently preferred location within the galaxy. SNe II never occur in elliptical galaxies and often chose to be born near or in HII regions and spiral arms.

Information on the frequency of supernovae explosions is the key parameter regulating the structure, kinematics and composition of the interstellar medium. The evolution of galaxies is controlled by the supernovae rate. The numbers of neutron stars, black holes, pulsars and X-ray binaries are all closely related to the SNe rates. Although the importance of the frequency measurement has been recognized, the values of SNe rates still remain rather uncertain. The main problem is that there are simply not enough objects discovered to split rates into SNe classes and galaxy types. Additionally, for a large fraction of all discoveries the supernova type is yet to be determined. Another important issue is that the control time of a survey is not easy to calculate as it depends on lightcurve shape, absolute luminosity and the absorption by dust in the host galaxy. Supernovae rates are normally expressed as the number of supernovae per century per unit blue luminosity. Since the total luminosity depends on the galaxy distance, the supernovae rates depend on $H_0^2$.

The absolute magnitudes of SNe are not only important for the computation of the SNe rates, they also provide constraints on the stellar progenitors and their explosion mechanisms as well as vital information for planning future ground- and space-based SN searches. Type Ia supernovae are the most luminous objects, with $M_V$ in the range between -18$^{th}$ mag and -20$^{th}$ mag including subluminous and overluminous events. The mean $M_V$ magnitudes of Type II-L and Type II-P supernovae are -17.6 and -16.5 respectively.

Supernovae lightcurves are the main source of information about these objects. However, only a limited number of SNe have reasonably detailed lightcurves and a very small number of supernovae have been caught before maximum. All SNe lightcurves are characterized by a sharp rise to maximum light, maximum phase and a steady decline (e.g. Leibundgut et al. 1991). Within one class, the shapes of SNe are different in different filters. In particular, the colors evolve very rapidly around maximum. In SNe Ia, the maximum phase starts about 5 days before the peak in the $B$ filter. Normally, these SNe reach maximum earlier in $I$ than in $B$, but in some objects, this is reversed. The peak phase itself can be approximated fairly well by Gaussian curves or second-order polynomials. Sometimes a second maximum can be observed in the $I$ and redder lightcurves. After about 50 days the lightcurves settle onto a steady decline which is exponential in luminosity.

Early studies of the photometric properties of the SN II separated these SNe into two classes: linear (L) and plateau (P). The subsequent increase in the photometric data revealed that these two classes are not well separated but there seems to exist a continuous transition from SN II-L shapes to SN II-P shapes (e.g. Patat et al. 1994). In 1987, there was discovered a prominent example of supernova that did not fit into an existing classification scheme. The closest and the best sampled SN, 1987A, was yet another peculiar supernova with an unexpected broad second maximum about 3 months after discovery. Although distinct at early phases, SNe II (including SN 1987A) show convergence to a unique decline rate at the epochs $> 100$ days.

SNe Ia have found ready application in cosmology. Their intrinsic brightness means that they can be detected to enormous distances. Although their peak luminosities vary by a factor of 10, Phillips (1993) found a correlation between the peak absolute magnitude and the rate of decline, which enables SNe Ia to be calibrated and used as "standard candles". Claims for an accelerating universe (e.g. Riess et al. 1998, Schmidt et al. 1998, Perlmutter et al. 1999) partly rest on their use as distance estimators, yet there are obvious concerns regarding systematic errors (e.g. Leibundgut 2000, 2001). So, a major thrust of modern SNe studies is to understand and quantify the differences in the morphology of SNe Ia lightcurves and the scatter in the Phillips relation. Recently, evidence was presented for a correlation between expansion velocities of the ejecta of Type II plateau supernovae and their bolometric luminosities during the plateau phase (Hamuy & Pinto 2002). This correlation allows one to use SNe II-P as "standard candles". This new technique requires spectra and photometric data around day 50 and some additional photometry and spectroscopy during the plateau to solve for the dust extinction in the host galaxy. The lightcurves are placed on the same time-scale using explosion times derived from "expansion photosphere method".

## 1.6 Purpose and structure of this thesis

In this introduction, we have attempted to overview the current status of the variability surveys (MACHO, OGLE, ROTSE, SuperWASP) and present the case for the future ambitious projects (Eddington, Gaia). The field of optical variability has progressed immensely over the last decade stimulated by recent technological advances. However, some of the important issues still remain unresolved. Unfortunately, there are no ready-to-use recipes to tackle these problems since most of them are concerned with phenomena never seen before.

The classification of lightcurves is a common problem confronting surveys in the era of terabyte astronomy. Perhaps the most vivid example is gravitational microlensing where event detection seems to have become a stumbling block to pioneering studies of Galactic structure. Chapters 2 and 3 will describe a new technique for lightcurve classification based on neural networks. Although tested in the context of microlensing, the method has a potential to develop into a standard classification machinery for massive variability searches.

Once microlensing event detection is made robust and unambiguous, what can we learn about inner Galaxy? How should we conduct the future microlensing searches in order to reveal the details of the Galactic structure? Chapter 4 compares the recent results of the gravitational microlensing surveys and the forecasts made with the current Galactic models. The maps of gravitational microlensing optical depth and event timescale are constructed for different bar/bulge configurations. The prospects for K-band microlensing are briefly discussed.

The huge datasets generated by forthcoming missions like Eddington or Gaia will contain complete samples of variable stars of all types, as well as measurements of extremely rare objects that are too valuable to be missed. In order to optimize the scientific returns of the planned surveys it is crucial to devise an efficient real-time alert system. A step towards the creation of such an alert dispatcher is a detailed simulation of a survey's data-stream. Chapters 5 and 6 are concerned with modeling of Gaia's observations of supernovae and gravitational microlensing.

The Gaia mission will establish a new field in the variable star research – astrometric variability. Chapter 6 presents a detailed analysis of astrometric variability caused by gravitational microlensing. It is shown how Gaia measurements combined with ground-based follow-up observations will allow the local mass function to be reconstructed with a good accuracy. Gaia is the first instrument that can determine the mass of local faint objects such as black holes and very cool white and brown dwarfs.

## 1.7 Bibliography

Akerlof C. et al., 2000, AJ, 119, 1901

Alcock C. et al., 1993, Nature, 365, 621

Alcock C. et al., 1997, ApJ, 482, 89

Alcock C. et al., 1998, AJ, 115, 1921

Alcock C. et al., 2000a, ApJ, 542, 281

Alfonso C. et al., 2003a, A&A, 400, 951

Aubourg E. et al., 1993, Nature, 365, 623

Binney J. et al., 1997, in *The Hipparcos Venice Simposium*, ed Perryman M.A.C., ESA Sp-102, 473

Boden A.F., Shao, M., van Buren, D., 1998, ApJ, 502, 538

Charbonneau D., 2003, in *Scientific Frontiers on Research of Extrasolar Planets*, eds Deming D. & Seager S., ASP Conf. Ser. (astro-ph/0209517)

Cieslinski D. et al., 2003, PASP, 115, 193

Comeron F., Torra J. & Gomez A. E, 1998, A&A, 330, 975

Dehnen W. & Binney J., 1998, MNRAS, 298, 387

ESA 2000, *GAIA: Composition, Formation and Evolution of the Galaxy*, Technical Report ESA-SCI(2000)4

Evans N.W., 2002, in *IDM 2002: The 4th International Workshop on the Identification of Dark Matter*, eds Spooner N., Kudryavtsev V. (astro-ph/0211302)

Evans N.W., 2003, in *Gravitational Lensing: A Unique Tool For Cosmology*, eds Valls-Gabaud D., Kneib J.-P., (astro-ph/0304252)

Eyer L. et al., 1994, SoPh, 152, 91

Eyer L., 2002, AcA., 52, 241

Filippenko A. et al., 2001, in *Small Telescope Astronomy on Global Scales*, eds Chen W.P., Lemme C., Paczyński B., ASP Conf. Ser., 246, 121

Geha M. et al., 2003, AJ, 125, 1

Gould A., 1992, ApJ, 392, 442

Grenon M., 1997, in *The First Results of Hipparcos and Tycho, 23rd meeting of the IAU, Joint Discussion 14*, Kyoto, Japan.

Groenewegen M. A. T., 2000, A&A, 363, 901

Groenewegen M. A. T.& Oudmaijer, R. D., 2000, A&A, 356, 849

Hamuy M. & Pinto, P., 2002, ApJ, 566, L63

Hamuy M., 2003, review for *Core Collapse of Massive Stars*, Ed. C.L. Fryer (astro-ph/0301006)

Hardin et al., 2000, A&A, 362, 419

Kane S. et al., 2001, in *Techniques for the detection of planets and life beyond the solar system*, ed Dent W.R.F., Edinburgh, Scotland, Royal Observatory, p.6 (astro-ph/0209188)

Koen C. & Eyer L., 2002, MNRAS, 331, 45

Landau L., Lifshitz E.M., 1971, *The Classical Theory of Fields*, Pergammon Press, Oxford, 3rd edition

Leibundgut B. et al., 1991, A&AS,89, 537

Leibundgut B., 2000, A&ARv, 10, 179

Leibundgut B., 2001, ARA&A, 39, 67

Li W., Filippenko A. & Treffers R., 2001, ApJ, 546, 734

Milsztajn A. et al., 2000, presented at the XIX International Conference on Neutrino Physics and Astrophysics, Sudbury, Canada (astro-ph/0011375)

Mollerah S., Roulet E., 2002, *Gravitational Lensing and Microlensing*, Word Scientific Publishing

Paczyński B. 1986, ApJ, 304, 1

Paczyński B. 1996, ARA&A, 34, 419

Paczyński B. 1997, in *Variables Stars and the Astrophysical Returns of the Microlensing Surveys*, eds Ferlet R., Maillard J.-P., Raban B., Cedex, France, Editions Frontieres, p.357 (astro-ph/9609073)

Paczyński B. 2001, in *Mining the Sky, Proceedings of the MPA/ESO/MPE Workshop*, eds Banday A., Zaroubi S., Bartelmann M., Heidelberg, Springer-Verlag, p.481 (astro-ph/0110388)

Patat F. et al., 1994, A&A, 282, 731

Gould A., Pepper, J., Depoy, D.L., 2003, ApJ, 594, 533

Perlmutter S. et al. 1999, ApJ, 517, 565.

Perryman M.A.C. et al. 2001, A&A, 369, 339

Phillips M.M., 1993, ApJ, 413, L105

Popowski P., Cook K., Becker A., 2003, submitted to AJ (astro-ph/0303075)

Riess A.G. et al. 1998, ApJ, 504, 935.

Rucisnki S., 1997, AJ, 113, 407

Schneider P., Ehlers J., Falco E.E., 1992, *Gravitational Lenses*, Springer-Verlag

Schmidt B.P. et al. 1998, ApJ, 507, 46.

Sumi T., 2004, MNRAS, 349, 193

Turatto M., 2003, to be published in *Supernovae and Gamma-Ray Bursters*, ed. Kurt W. Weiler (astro-ph/0301107)

Udalski A. et al., 1993, AcA, 43, 289

Welch D. & Stetson P., 1993, AJ, 105, 1813

Wheeler J.C., 2003, (astro-ph/0209514)

Wielen R., 1996, A&A, 314, 679

Zwicky F., 1965, in *Stellar Structure*, eds Aller L.H. & McLaughlin D.B., University of Chicago Press, Chicago, 367

# Chapter 2

# Lightcurve Classification with Neural Networks

This chapter exploits neural networks to provide a new way to classify lightcurves in massive photometric datasets. The network presented here can distinguish microlensing lightcurves from other forms of variability, such as eruptive, pulsating, cataclysmic and eclipsing variable stars. We begin the chapter by reviewing the basics of observational microlensing (§2.3) and neural computation (§2.3). Next two sections are concerned with the experiments with a neural classifier. The network architecture, details of pre-preprocessing and training are specified in §2.4. In §2.5 the committee of neural networks is tested on noisy data taken by the MACHO collaboration. The advantages of neural networks for microlensing rate calculations, as well as the future developments of massive variability surveys, are both briefly discussed in §2.6 and §2.7.

## 2.1 Introduction

Variability in the sky has been known for thousands of years, but our understanding of variable sources remains very incomplete. Some of the most interesting objects in the sky are transient. These include supernovae, microlensed stars, near-Earth or killer asteroids (which are transient because of their exceptionally large proper motions) optical flashes associated with gamma-ray bursts and stars undergoing short-lived but key stages of stellar evolution like the helium core flash and so on. All these objects are rare. To hunt them down in a systematic way means that we must record images, process the data in real-time (or nearly so), recognise the events from their lightcurves and archive them.

The earliest examples of massive transient astronomy searches are the microlensing surveys like MACHO, EROS and OGLE. Typically, the surveys monitored $\sim 5 \times 10^6$ stars a few times every night over several years in the directions of the Galactic Bulge and the Magellanic Clouds, yielding $\sim 10^{10}$ photometric measurements. Out of the $\sim 10^5$ sources which were variable, the surveys tried to identify $\sim 10^2$ true microlensing events. The selection criteria typically involved the imposition of sets of cuts to ensure good lightcurve coverage and a steady baseline flux, to require a single bump and thus eliminate common forms of stellar variability and to require a good statistical fit to the achromatic standard microlensing lightcurve and so on. Many of the cuts developed through trial and error, and evolved as the experiments progressed (e.g., Alcock et al. 1997, 2000a). Unambiguous identification of microlensing events was sometimes not possible, and the collaborations sometimes reported their results in terms of two sets, one of high quality events (any lightcurve that was undoubtedly microlensing) and one of possible events (any lightcurve with a unique peak and a flat baseline). Sometimes the cuts even eliminated interesting events – for example, the longest ever microlensing event OGLE-1999-BUL-32 was originally missed as its baseline flux was not constant and so failed one of the imposed cuts (Mao et al. 2002).

Additionally, microlensing alert or early warning systems (e.g., Udalski et al. 1994) work by reducing the number of candidates to manageable amounts. Each night's candidates are individually examined for the onset of microlensing. Even for surveys as large as OGLE II, this worked well. However, still larger surveys are planned for the future and therefore it becomes important to automate the procedure and issue alerts without human intervention.

The microlensing experiments are of course not the only massive photometry searches being conducted by astronomers at the moment. There are also collaborations primarily looking for supernovae (e.g., The Supernovae Cosmology Project), optical flashes related to gamma-ray bursts (ROTSE) and near-Earth asteroids (NEAT and LINEAR). More generally, as Paczyński (2001, 2002) has emphasised, the monitoring of the optical sky for variability is likely to enjoy a huge resurgence over the coming decade given the low cost of robotic telescopes. The very near future will see terabyte datasets of lightcurves routinely available to astronomers. Such datasets will contain complete samples of variable stars of all types, as well as the very rare objects or events which primarily motivate the search. It is an urgent and important problem to automate the classification of lightcurves in massive variability surveys.

This chapter argues that new analysis methods based on neural networks will enable us to pinpoint and identify scarce transient objects in such huge datasets. Our illustrative example is the identification of scarce microlensing events against the background of variable stars. However, we envisage that the applicability of the technique is much wider.

## 2.2 Microlensing lightcurves

At any instant, the probability that a source star in the Galaxy shows the microlensing effect is $\lesssim 10^{-6}$. Microlensing events are hugely outnumbered by stellar variability which is at least a hundred thousand times more common. The lightcurve classification problem is to devise algorithms that diagnose the different kinds of variability. For applications to microlensing, the algorithm must distinguish microlensing from other sources of variability (whether intrinsic or extrinsic).

Let us assume a single, point-like, dark lens. The microlensing lightcurve has a characteristic form written down by Paczyński (1986). The lightcurve is symmetric and achromatic. As the probability of microlensing is so low, the variability must not repeat. Microlensing is readily distinguished from some, but unfortunately not all, forms of stellar variability. A cautionary history is provide by the fate of the candidate event EROS-LMC-2. This was one of the microlensing candidates uncovered by the photographic plate search of the first phase of the EROS experiment towards the Large Magellanic Cloud (Ansari et al. 1996). Although the source star of EROS-LMC-2 was known to be variable at a low level (Ansari et al. 1995), nonetheless microlensing seemed favored by the excellent fit of the lightcurve to the datapoints. However, there was a substantial second bump in the lightcurve eight years after the first, and EROS-LMC-2 was then discarded as a microlensing candidate (Lasserre et al. 2000).

The background in microlensing databases is composed of periodic variables (e.g., Cepheids, RR Lyrae), eruptive variables (e.g., dwarf novae, classical novae), semi-regular variables (e.g., bumpers) and the supernovae occurring in galaxies behind the source population. Of these, the most troublesome in microlensing surveys towards the Magellanic Clouds and Andromeda are the bumpers and the novae-like objects. Although SNe Ia have reasonably well-understood lightcurves, the same is not true of other types of supernovae which can mimic microlensing rather well (for example, events 22 and 26 of

Alcock. et al. 2000a). Long period bumpers may be present as single bumps even in 5 seasons worth of data and they can be well-fit by the standard microlensing lightcurve.

Let us stress that the identification of microlensing events remains an awkward – and not fully solved – problem. For example, it probably lies at the heart of the seeming discord between the results of the MACHO and EROS experiments towards the Large Magellanic Cloud (LMC). The MACHO group identified between 13 and 17 events towards the LMC, whereas the competing EROS group found only 3 (Alcock et al. 2000a, Lasserre et al. 2000). Although the exposure times and field locations between the two experiments do vary, nonetheless the rate found by MACHO is at least twice than that found by EROS. This same disparity is also seen in the experiments towards the Galactic Bulge, as MACHO find an optical depth to microlensing of $\sim 3.23 \times 10^{-6}$ (Alcock et al. 2000b), whereas the EROS value is about half of this (Afonso et al. 2003). Possible explanations are that the MACHO selection algorithm may be too loose (causing contamination with other variable sources), or that the EROS selection algorithm may be too harsh (causing genuine events to be discarded). It is here that neural networks may be able to make a decisive contribution.

## 2.3 An informal introduction to neural networks

Neural networks have been used before for pattern recognition tasks in physics (e.g., Bishop 1995). In particular, they are often used in high energy physics experiments as triggers to select interesting events from large datasets (Müller, Reinhardt & Strickland 1995, chapter 8). Recent astronomical applications include classification of optical stellar spectra (Bailer-Jones et al. 1997) and galaxy type (Lahav et al. 1995), object detection in wide field imaging (Andreon et al. 2000) and predictions of astronomical time series (e.g., Conway 1998, Perdang & Serre 1998). There has also been a recent report of preliminary results on automatic lightcurve classification by the ROTSE collaboration

(Wozniak et al. 2001). An interesting review of a number of astronomical applications is in Storrie-Lombardi & Lahav (1994).

In a neural network, the neurons are arranged in layers. The input data is fed to the bottommost layer. The output value emerges from the topmost layer, the intervening layers are hidden. The values of the neurons in any layer $a_j$ are calculated via

$$a_j = \sum_i w_{ji} z_i. \tag{2.1}$$

Here, $w_{ji}$ are the synaptic weights of the jth neuron with respect to the ith neuron and $z_i$ are the activation values. The activation value is computed from the value on the neuron via an activation function $g$

$$z_i = g(a_i). \tag{2.2}$$

As an activation function, we use the logistic function (or sigmoid activation function)

$$g(a) = \frac{1}{1 + \exp(-a)}, \tag{2.3}$$

which allows us to interpret the outputs of the network as *a posteriori* probabilities (Bishop 1995, chapters 3,6).

We start with a sequence of input units (the "patterns") for which the desired values of the output (the "targets") are known. This is called the training set. Given the patterns and a set of weights, we can construct an error function $E$ which quantifies the performance of the network. We want to obtain the weights $w_{ji}$ that minimize the error function over the training set using a steepest descent scheme.

We begin with random values for the weights and perform a sequence of iterative updates using a variant of back-propagation as the learning algorithm. The error derivatives

| Variable | Reference |
| --- | --- |
| Eruptive | van Genderen (1995), AAVSO |
| Pulsating | Antonello & Morelli (1996), AAVSO |
| Cataclysmic | Hamuy et al. (1996), AAVSO |
| Eclipsing | Brancewicz, Dworak (1980) |

Table 2.1: Sources of lightcurves of variable stars. AAVSO is the American Association of Variable Star Observers.

with respect to the weights are

$$\frac{\partial E^n}{\partial w_{ji}} = \delta_j^n z_i^n, \qquad \delta_j^n \equiv \frac{\partial E^n}{\partial a_j}, \tag{2.4}$$

where $n$ labels the pattern. Using the chain rule, we obtain the back-propagation formula

$$\delta_j^n = g'(a_j) \sum_k w_{kj} \delta_k^n, \tag{2.5}$$

which shows how the values of $\delta_j^n$ propagate through the network, given the target value. In each iteration, the weights are updated according to the following rule

$$\Delta w_{ij} = -\eta \sum_n \delta_j^n z_i^n, \tag{2.6}$$

where $\eta$ is the constant learning rate. The sum is performed over all the patterns. This is equivalent to the steepest descent method of minimising the error. In practice, we use a refinement of this algorithm, called resilient back-propagation, which helps to prevent entrapment in local minima (see e.g., Bishop 1995, section 7.5.3). As the network is converging to a minimum, it it important to prevent over-training. This is done by feeding a different set of patterns (the "validation set") to the network. The errors over the patterns in the training and the validation sets are separately computed. The training process is stopped just before the error in the validation set begins to rise. Finally, the performance of the fully trained network can be assessed with a third set of patterns (the "test set"). It is important to ensure that the training, validation and test sets do not contain any identical patterns.

## 2.4 Implementation

The experiments described below use the Stuttgart Neural Network Simulator[1]. Our network is composed of one input layer, one hidden layer and one output layer. The hidden layer is fully connected to the input and output layers. There are 5 neurons in the input layer, 5 neurons in the hidden layer and one neuron in the output layer. The value of the output neuron gives the probability that the event is microlensing. The reason for the choice of 5 input neurons will become obvious shortly.

### 2.4.1 The training and the validation sets

There are three types of lightcurves in the training set – simulated microlensing events, variable star lightcurves from archival sources, and sample lightcurves from a microlensing experiment (in this case, the MACHO experiment). Simulated microlensing events are generated by randomly choosing an impact parameter, an Einstein crossing time between 7 days and 365 days and a time when the event reaches maximum. Random Gaussian noise is added with a dispersion in the range from 0.1 to 20 % of the maximum flux. The lightcurves are sparsely sampled using the MACHO sampling.

Variable stars may be divided into periodic variables and eruptive/cataclysmic variables. The former are usually easier to distinguish from microlensing than the latter, always provided more than one period can be detected in the sampled datastream. Examples of typical lightcurves for different types of variability are shown in Figure 2.1. The periodic variables include pulsating stars (such as Cepheids and Miras) and eclips-

[1] http://www-ra.informatik.uni-tuebingen.de/SNNS

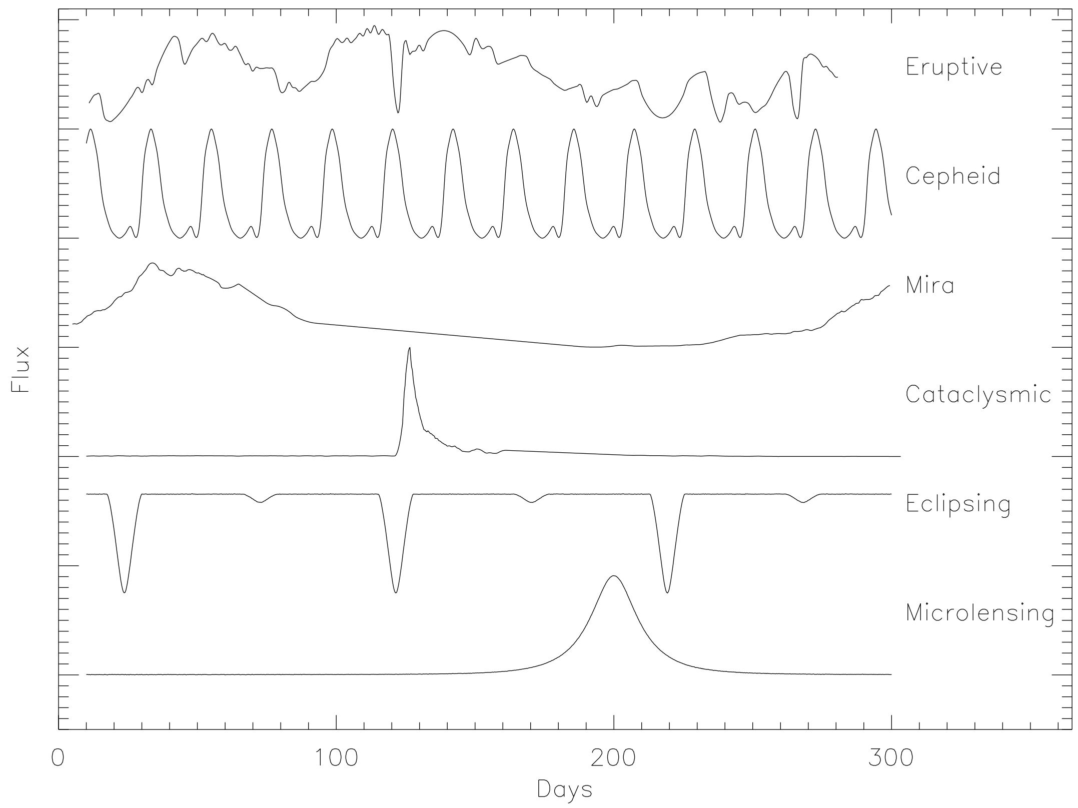


Figure 2.1: This shows sample lightcurves of different types of variability included in the training and validation sets.

ing stars. Eruptive variables include T Tauri, S Doradus and pre-main sequence stars. Cataclysmic variables include novae, supernovae and symbiotic variables. The relative frequencies with which these stars occur are not important in our analysis. All that matters is that the gamut of shapes is well-represented in the training set. We are therefore interested as much in regular representatives as in extreme examples of the lightcurves. Lightcurves for the variable stars are selected from the sources listed in Table 2.1. For long data sequences, the experimental window is placed randomly on the lightcurve. In this way, we ensure that the bumps in the lightcurves do not occur in a privileged place.

Finally, there are lightcurves randomly chosen from the MACHO database (specifically, from field 113 towards the Bulge). The rationale for this is that instrumental artifacts are certainly present in the MACHO lightcurves and it is important for the neural network to be able to recognise these.

The training set contains 400 microlensing lightcurves, 150 stellar variable lightcurves and 200 MACHO lightcurves. The validation set contains the same number of lightcurves, although the individual representatives are obviously different. The test set are the $\sim 5000$ lightcurves from MACHO tile 113.18292 which is part of field 113 towards the Galactic bulge. Let us note that – compared with real data from a variability survey – microlensing events are over-represented in our training and validation sets. The consequence of this is that the network will provide more false positives (as the prior probability of microlensing is too high). This is highly desirable, as the best approach to detecting such an intrinsically rare phenomenon as microlensing is to force fewer false negatives at the expense of more false positives.

### 2.4.2 Pre-processing

In many applications, it is both customary and advantageous to pre-process data for feeding to the neural network. The main problem with using raw photometry data is the curse of dimensionality (see Bishop 1995, chapter 8). The simplest way of overcoming this is to extract features of the lightcurve and use this as input to the network. Properly implemented, this can lead to a very efficient network, as prior knowledge can be incorporated and redundant variables can be discarded in the pre-processing. However, there are dangers as well, as important features in the lightcurves can be erased.

The aim of a neural network is not to model the patterns but to model the decision boundary between the patterns. In microlensing surveys, event identification normally proceeds by making sequences of cuts, in which case the decision boundary is formed by a set of hyperplanes. The advantage of a neural network over conventional sequences of straight line cuts is that the former offers a better chance of describing a complicated decision boundary accurately.

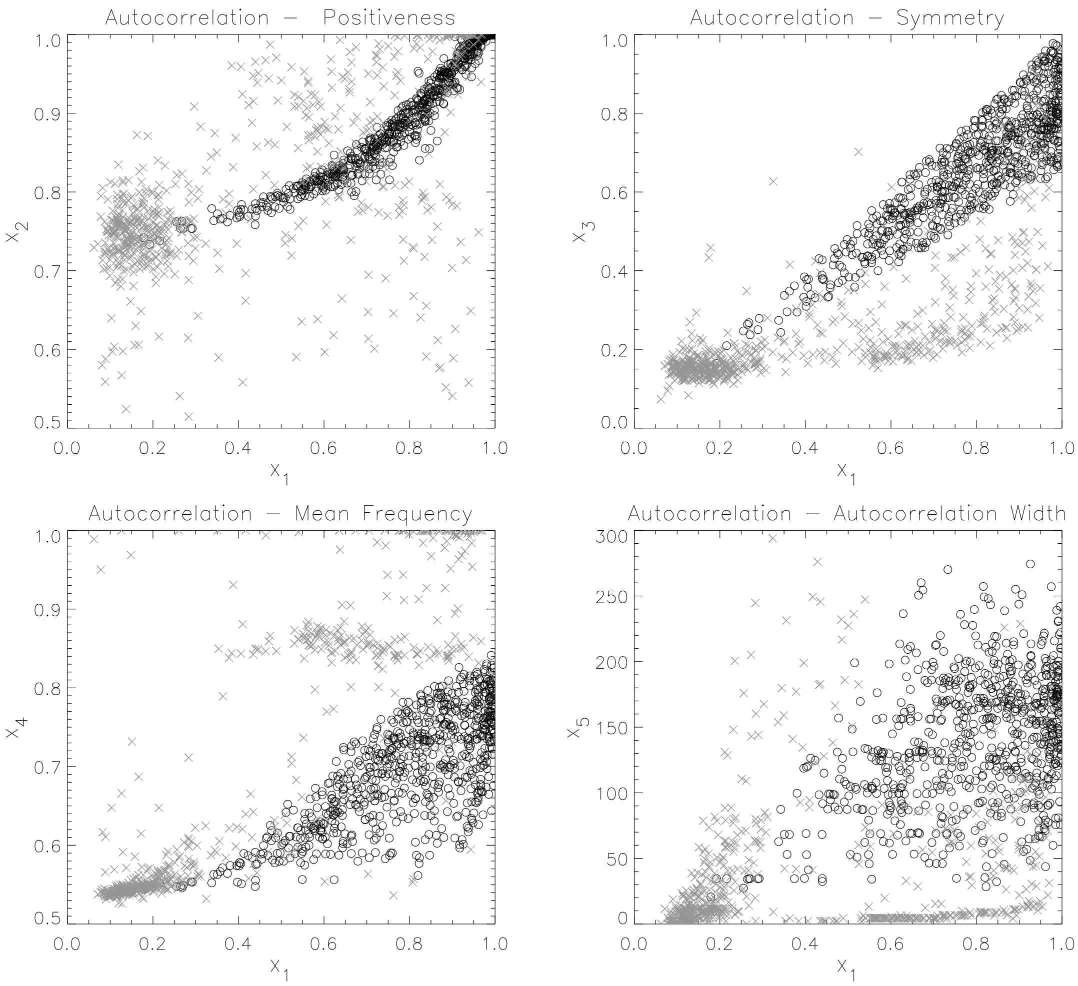


Figure 2.2: This shows projections onto the principal planes of the five-dimensional space of inputs. Bold circles show the microlensing events and grey crosses the variable stars and noise in the training and validation sets.

Microlensing events are characterised by the presence of a (iv) single, (iii) symmetric, (ii) positive (i) excursion from the baseline. The event itself is characterised by (v) a timescale. Motivated by these five features, we extract from the lightcurves the following five parameters, which are inputs to the neural networks. The first $x_1$ is the maximum value of the auto-correlation function. This helps to discriminate against noise and identify the presence of any signal. The second $x_2$ is calculated as follows. First, we compute the median of the flux measurements which gives a good approximation to the baseline. We then compute the mean of the datapoints lying above and below the median and finally take their ratio. This is then mapped on the interval [0.5,1] with the logistic function. The input $x_2$ tests for the positiveness of the excursion. The third $x_3$ is the maximum value of the cross-correlation function of the lightcurve with the time-reversed lightcurve. This provides a test for symmetric events. The fourth $x_4$ is the mean frequency $\langle\nu\rangle$ calculated with the power spectrum $P(\nu)$ as a weighting function. For a periodic variable, we expect a shift in the weighted mean frequency from zero. We compress $x_4$ with the logistic function to lie in the range $[0.5, 1.0]$. Finally, the fifth $x_5$ is the width of the autocorrelation function, as judged by its standard deviation. If the event is microlensing, then the width is a rough indication of the timescale.

To motivate this choice of inputs, Figure 2.2 shows the locations of all the patterns in the validation and training sets. The desideratum is that the choice of inputs offers a clear separation between microlensing events and other patterns in the five dimensional space $(x_1, \cdots, x_5)$. The projections of this space onto the principal planes offer grounds for believing this, as there is already good partial separation in some of the plots (e.g., $x_1$ versus $x_3$) and good evidence for regularities in others (e.g., $x_1$ versus $x_2$). The final proof that the choice of inputs is good can, however, only be provided by the performance of the network on the test set.

Note that Figure 2.2 plots unnormalized input variables; however, the neural network uses normalized inputs. Scaling of the inputs to numbers of the order of unity is often useful, as this means that the network weights also typically take values of the same order (Bishop, 1995, chapter 8). Pictorially, this can be thought of as requiring the hyperplanes associated with each hidden unit to intersect close to the origin and near the center of the data-cloud. For each input variable, this scaling is done by subtracting the mean and dividing by the standard deviation to give the normalized inputs.

So far, we have skirted round the problem of missing datapoints. For MACHO data,

$\sim 10\%$ of the lightcurves have gaps of the order of a few days (aside from the 5 month gaps when the Galactic bulge is not visible from Australia). To compute the correlation functions, the data is treated as if it were uniformly sampled. This gives rise to some errors. If the typical gap size is much smaller than the event timescale, then any errors we have introduced by this procedure will be small. If the gap size relative to the timescale is very large, then no classification can be plausibly extracted. If the gap size is of the same order as the timescale, then the experiment needs re-designing. The input most sensitive to missing data is $x_4$ because this requires computation of the power spectrum. There are, however, existing algorithms to do this for unevenly sampled data (e.g, Lomb's periodogram as implemented by Press & Rybicki (1989) and Press et al. (1992)), which we employ.

Note that pre-processing gives rise to fast and powerful neural networks, but it can also cause loss of potentially important information in the data. To check this, we can allow a neural network itself to perform the projection. This leads to much bigger neural networks which consequently take longer to converge. However, it does have the advantage that no assumptions are built in from the beginning. In this spirit, we experimented with a big neural network which takes as the two input layers the unadulterated flux measurements and errors at the sampling times and has $\sim 200$ hidden neurons. Once converged, the performance of this big network is similar to the performance of smaller networks on pre-processed data. From this, we draw the conclusion that our pre-processing has not caused any serious degradation of information in the data.

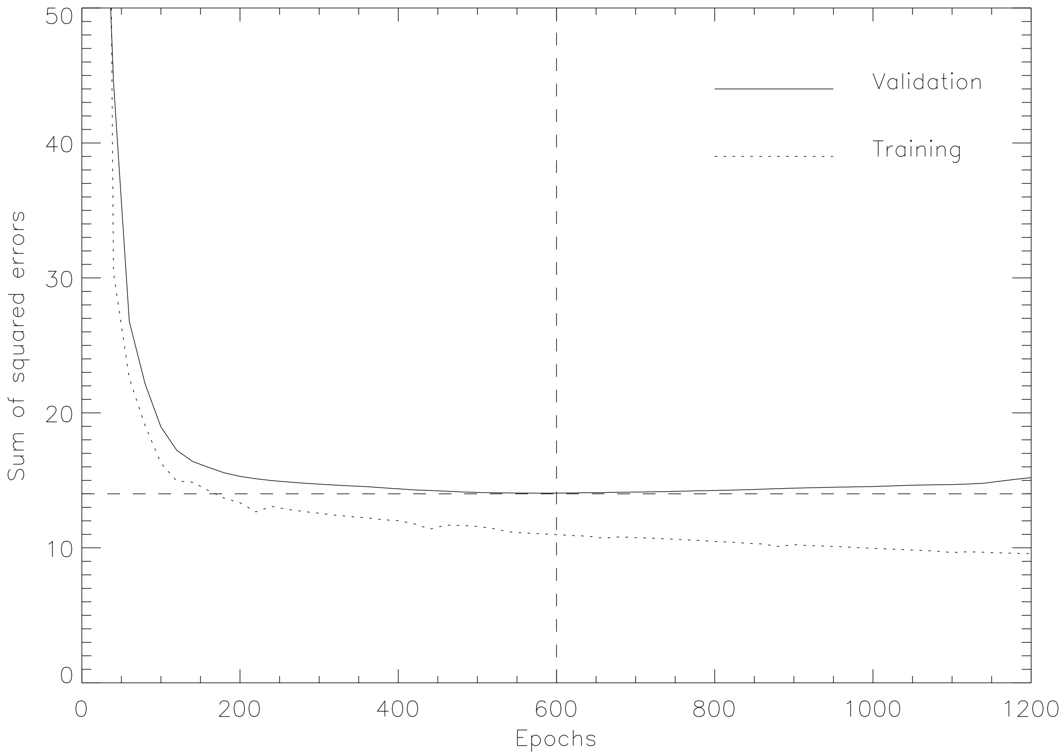


Figure 2.3: This shows the value of the cross-entropy error function versus the epochs of training (number of iterations) for the patterns in the training and validations sets. The long-dashed line shows the point at which the training is stopped. The sum of errors is $\sim 15$ out of the 700 patterns in the set.

### 2.4.3 Training

In training, the weights are initialised to random values. We then perform iterations to reduce the error function

$$E = -\sum_n \left(t^n \log y^n + (1 - t^n) \log(1 - y^n)\right) \tag{2.7}$$

where $t^n$ and $y^n$ are the target ($t = 1$ for all microlensing lightcurves in the training set and $t = 0$ for other types of variability) and the response of the output neuron for the $n$th pattern. We have chosen this form of the error function (the so-called *cross-*

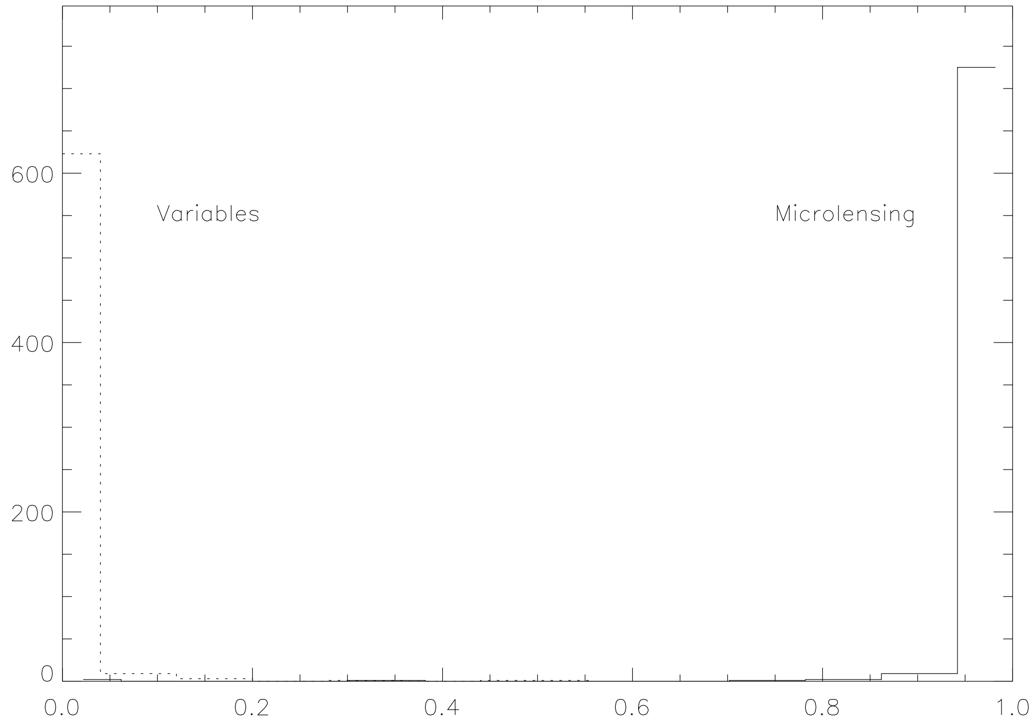


Figure 2.4: This shows the histogram of output values for the 1500 patterns in the validation and training sets. Note the clean separation between microlensing and other types of variability.

*entropy* error function) as appropriate for two class problems (see e.g., Bishop 1995, section 6.7). Given our choice of activation (2.3) and error functions (2.7), the output $y^n$ approximates the posterior probability $P(\text{microlensing}\,|\text{inputs})$. The neural network must be able to generalize from the patterns in the training set, and not merely reproduce them. A worry is that the network will be over-trained and will reproduce structures of the decision boundary in unnecessary detail. To guard against this, we use early stopping as illustrated in Figure 2.3. The performance of the network on the validation set is compared to that on the training set and the training stopped just before the error in the validation set rises. Another safeguard is provided by the introduction of a small amount of noise to the weights on each iteration, which guards against entrapment in a local minimum.

If training is started from different initial weights, we converge to slightly different final weights. This makes it advantageous to use a committee of 10 neural networks (Bishop 1995, section 9.6). There are a total of 1500 lightcurves available. For each member of the committee, the 1500 patterns are split in half randomly to give validation and training sets with 750 members. For each pattern, the final output is the average of the output of all 10 neural networks.

The histogram of the output values for the combined validation and training set is shown in Figure 2.4. There is a very clean separation of microlensing events and other forms of variability. The non-microlensing events are strongly peaked at a probability $y = 0$, but there are a few events ($\sim 10$) that extend up to $y = 0.2$. The microlensing events are strongly peaked at $y = 1$, although again there are a few ($\sim 10$) that extend down to $y = 0.7$. The probability $y = 0.5$ corresponds to the formal decision boundary (Bishop 1995, section 10.3). In fact, between $0.2 < y < 0.7$, there are almost no events in the histogram. If, when presented with a lightcurve, the neural network does give an output in this range, then the classification is in reality uncertain. This is because any error in the output can cause it to straddle the formal decision boundary. This range of outputs really corresponds to patterns that are not present in the training and validation sets. This is valuable as it offers the possibility of the detection of unexpected and novel events in variability surveys.

There are just 3 microlensing events out of 800 that are misclassified (i.e., have $y < 0.5$). These are scarcely visible on the histogram. It is interesting to locate these events in our input space (see Figure 2.2). These events have input coordinates (1.05, 0.74, 0.16, 0.54, 20.63), (0.19, 0.73, 0.16, 0.55, 34.53) and (0.22, 0.74, 0.21, 0.55, 34.53). They are small amplitude or short duration events dominated by noise, as indicated by the value of the $x_1$ input which measures the presence of the signal. There is 1 false

| ID | MACHO ID | R | B | ID | MACHO ID | R | B |
|---|---|---|---|---|---|---|---|
| 1 | 97-BLG-24 | 0.93 | 1.00 | 2 | 95-BLG-5 | 0.92 | 0.96 |
| 3 | 97-BLG-42 | 0.00 | 0.00 | 4 | 97-BLG-s4 | 0.72 | 0.00 |
| 5 | 95-BLG-15 | 0.00 | 0.00 | 6 | 95-BLG-s8 | 1.00 | 1.00 |
| 7 | 97-BLG-18 | 1.00 | 1.00 | 8 | 96-BLG-26 | 1.00 | 1.00 |
| 9 | 97-BLG-38 | 0.64 | 0.47 | 10 | 97-BLG-58 | 1.00 | 1.00 |
| 11 | 96-BLG-1 | 1.00 | 1.00 | 12 | 97-BLG-2 | 1.00 | 1.00 |
| 13 | 96-BLG-14 | 0.00 | 0.00 | 14 | 95-BLG-s9 | 0.99 | 0.91 |
| 15 | 96-BLG-21 | 0.68 | 0.00 | 16 | 95-BLG-1 | 1.00 | 1.00 |
| 17 | 96-BLG-s10 | - | 0.16 | 18 | 96-BLG-20 | 0.99 | 1.00 |
| 19 | 96-BLG-10 | 0.99 | 0.90 | 20 | 95-BLG-4 | 0.81 | 0.02 |
| 21 | 95-BLG-23 | 0.00 | 0.00 | 22 | 95-BLG-s13 | 0.64 | 0.05 |
| 23 | 95-BLG-10 | 1.00 | 1.00 | 24 | 97-BLG-4 | 0.00 | 0.00 |
| 25 | 97-BLG-16 | 1.00 | 0.23 | 26 | 96-BLG-8 | 0.96 | 0.99 |
| 27 | 95-OGLE-16 | 0.99 | - | 28 | 95-BLG-39 | 0.16 | 1.00 |
| 29 | 95-BLG-3 | 0.39 | 0.00 | 30 | 97-BLG-37 | 1.00 | 1.00 |
| 31 | 97-BLG-14 | 0.21 | 0.00 | 32 | 95-BLG-11 | 0.01 | 0.00 |
| 33 | 96-BLG-31 | 0.81 | 1.00 | 34 | 96-BLG-s16 | 1.00 | 0.83 |
| 35 | 97-BLG-s14 | 0.80 | 0.90 | 36 | 95-BLG-22 | 0.30 | 0.79 |

Table 2.2: This shows the output of the committee of neural networks on the subset of candidates towards the bulge in Alcock et al. (2000b) which are selected on the basis of the conventional PSF photometry package (SoDoPhot). The results of the analysis of the red and blue lightcurves are shown separately. The output is the probability that the event is microlensing. (Note that the red data for event 17 and the blue data for event 27 are unavailable).

positive (i.e., a non-microlensing lightcurve with $y > 0.5$), which has coordinates (0.27, 0.75, 0.21, 0.56, 40.87). This is a lightcurve from the MACHO tile which is probably neither microlensing nor variable star, but just noise.

## 2.5 Tests towards the bulge fields

### 2.5.1 Normal events

All MACHO lightcurves extracted with conventional PSF photometry (such as SoDoPhot) are now publically available (Allsman & Axelrod 2001). As a first test, we use lightcurves

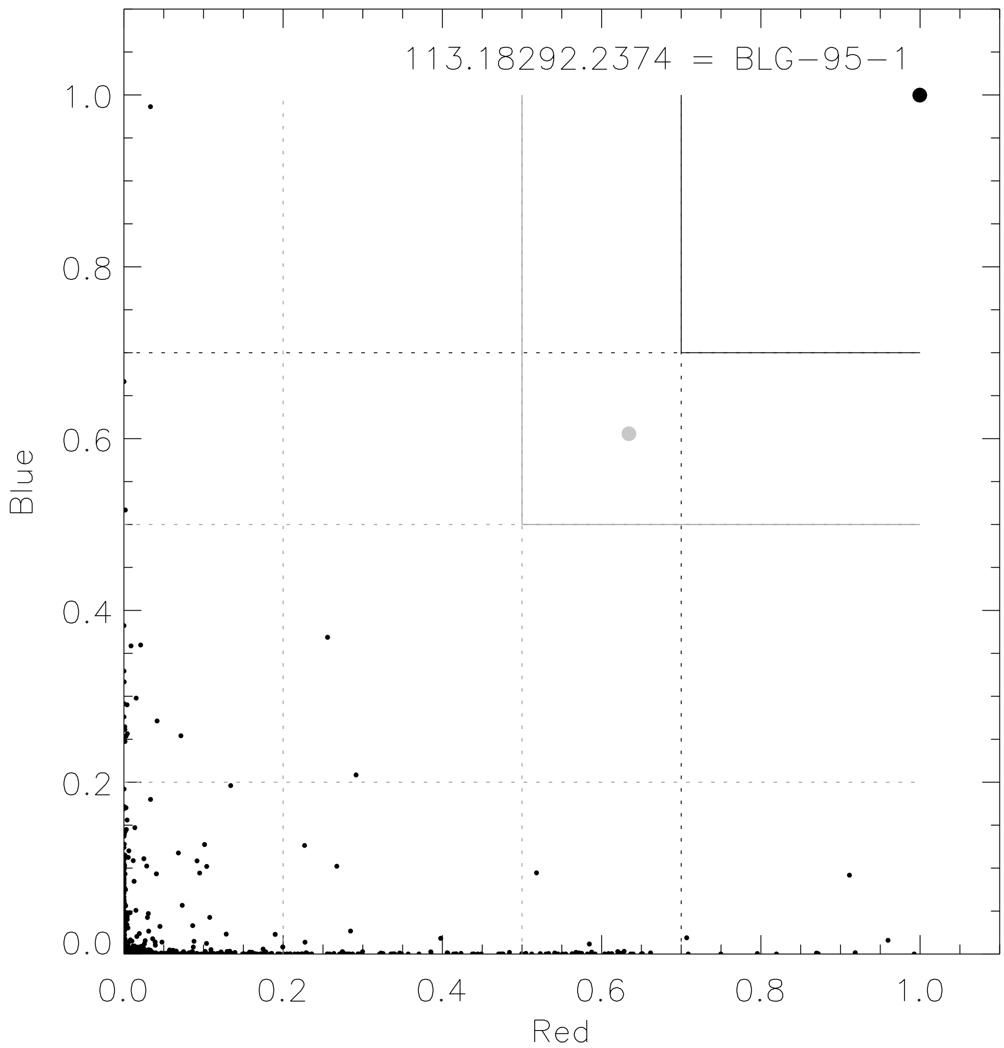


Figure 2.5: This shows the output of the committee of neural networks for all lightcurves in tile 113.18292, which is publically available from the MACHO project web-site (see Allsman & Axelrod 2001). Shown on the vertical and horizontal axes are the probabilities that the blue and red lightcurves are microlensing. There are $\sim$ 5000 lightcurves on the tile, including one event BLG-95-1 identified by the MACHO collaboration as microlensing. This is shown as the black spot.

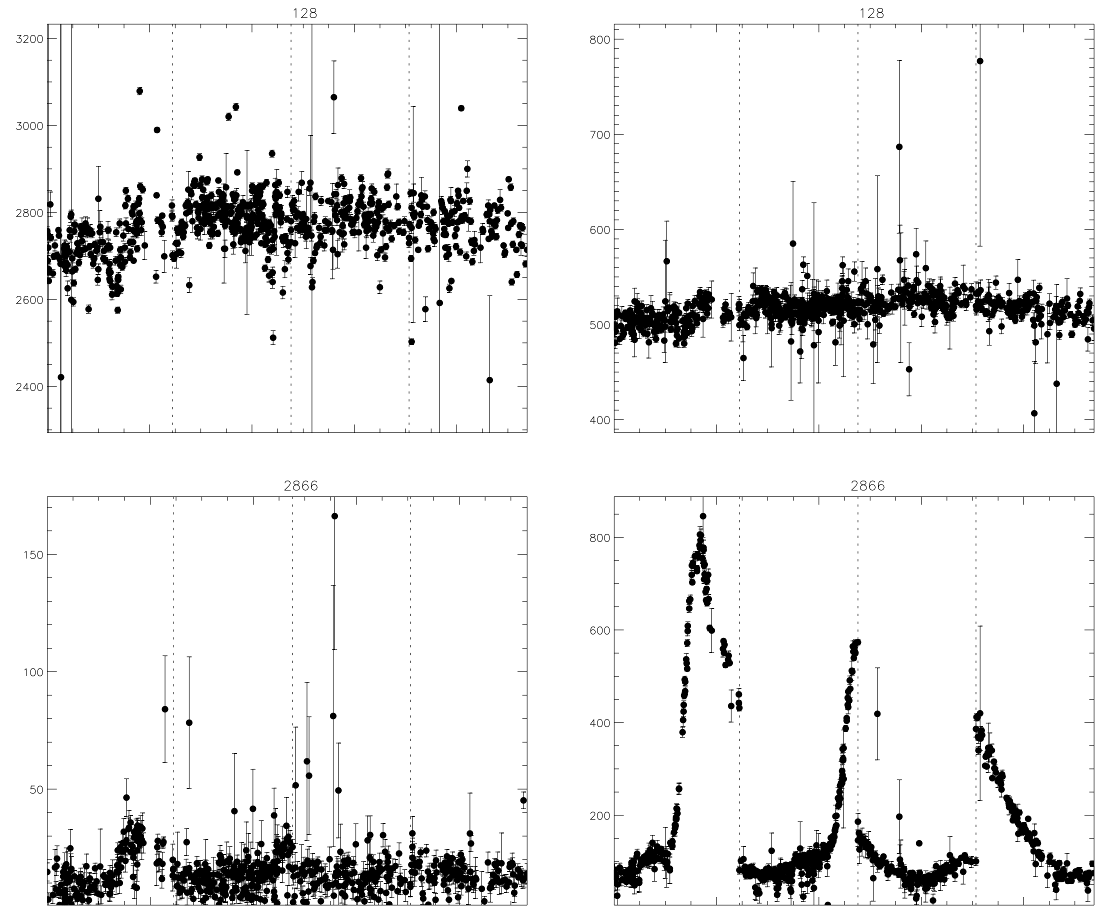


Figure 2.6: The upper panels show the blue and red lightcurves for the event identified by the grey spot in Figure 2.5. The lower panels show the lightcurves for the event securely identified in blue (left panel), but not in red (right panel). In all cases, the horizontal axis is time in days, the vertical axis is flux in ADU/s.

from tile 18292 of field number 113, which lies towards the Galactic bulge. This tile contains $\sim$ 5000 lightcurves of which one was identified by MACHO as a microlensing event. The MACHO data are taken at a site with moderate seeing. According to Alcock et al. (2000b), the median seeing is $\approx$ 2.1 arcsec. This means that the quality of the data is sometimes quite poor. To allow for this, we clean the lightcurves by removing all isolated points with more than $3\sigma$ deviation from the immediately preceding and succeeding datapoints. In general, this makes good sense as it removes outliers, but it can sometimes remove meaningful datapoints for very rapid brightness variations.

Each cleaned lightcurve is shown to the committee of neural networks. The red and blue passband data are analysed separately. In principle, it would be advantageous to analyse the red and blue data together because most variable stars show chromaticity differences. However, this option is not open to us at the moment because the publically available colour information on variable stars is still quite limited. Figure 2.5 shows the results of the deliberations of the committee. The probability of microlensing given the blue data is shown against the probability given the red data. There is only one pattern that satisfies this, namely the event identified by MACHO as BLG-95-1. It is clearly and cleanly separated from the rest of the patterns in the figure as a black circle in the topmost right corner. There is an additional pattern that has output values $y \approx 0.6$ for both the red and blue data. This falls within the regime of novelty detection. Its input coordinates are (0.43, 0.7, 0.26, 0.61, 183.14). It is a very long event since $x_5$ is higher than typical values for microlensings. It falls into a poorly-sampled region in Figure 2.2 which suggests why this low signal-to-noise lightcurve was dragged into the microlensing range. Its lightcurve is shown in the upper panel of Figure 2.6. It is most probably a form of stellar variability that does not lie in the training and validation sets. It is interesting to note that there are a number of lightcurves with output greater than 0.9 in one band, but not in the other. Shown in the lower panel of Figure 2.6 is a typical example, in this case securely identified in blue ($y > 0.95$) but not in red ($y < 0.05$). The blue lightcurve does indeed look like a microlensing event, but the better sampling in the red passband shows a highly active many-humped lightcurve which is most probably an eruptive variable.

As a second test, we analyse the lightcurves for all 36 events in Alcock et al (2000b) that were identified on the basis of conventional PSF photometry. Table 2.2 shows the results of the poll of the committee. In each case, the output of the neural network on the red and the blue data is given. Of course, it is important to bear in mind that the MACHO group's classification algorithm is itself probably not 100 per cent efficient. There are reasons to believe – both from the very high rate towards the Galactic Center that is incompatible with theoretical models of the Galaxy and from the differences between the MACHO and EROS results – that the subsample of candidates found by MACHO may have some contamination. There are total of 19 events identified with a probability $\gtrsim 0.5$ as microlensing in both the red and blue filters. In fact, these events are all beyond reproach as microlensing candidates as the probability $\gtrsim 0.9$. Events 28 and 36 are securely identified in the blue data, but the red data is corrupted. Events 4, 9, 15, 20, 22 and 25 are identified in the red data, but not in the blue. Lastly, there are 9 events for which no microlensing signal whatsoever is detected (event numbers 3, 5, 13, 17, 21, 24, 29, 31, 32). We shall examine the lightcurves of some of these events shortly, but for the moment let us emphasise that there is no guarantee that the original identification by the MACHO collaboration was correct.

Fig 2.7 shows the contours of probability for the training and validation sets in the input space. Light gray means that the probability is greater than 0.5 and corresponds to the formal decision boundary (see Bishop 1995, section 10.3). Dark gray means that the probability is greater than 0.9 and corresponds to almost certain microlensing. The irregularity of the contours is due to the fact that some regions are poorly sampled in the training and validation sets. The contours have been drawn with a view to guiding the eye. Superposed on the contours in Fig 2.7 are the events. The nine unfilled circles are those identified by the network as variable stars but by MACHO as microlensing events. The black circles are those for which both MACHO and the network agree as microlensing. There are a number of things to notice in the diagram. First, it is evident that the network has the ability to extrapolate from the validation and training sets and assign relative importance to the combinations of features extracted by the input variables. This is clear because there are events securely identified although they lie outside the contours (for example, event 18 is unambiguously identified despite lying outside the probability contours in the two top panels). Second, the $x_4$ input is the only one for which explicit allowance has been made for noise and sampling. The network seems to assign greater importance to this input, as almost all the filled circles lie within the projected 90% probability contour. This suggests that further improvements may be possible by allowing for noise in the extraction of other input parameters (for example, using extirpolation (Press & Rybicki 1989) for the correlation analysis). Third, the separation between the 0.5 and 0.9 probability contours is typically very small, so the contour surface is very steeply rising. Such outputs can correspond to novelty detection. Accordingly, they occupy only a small region of the input space and so novelty detection occurs – as is highly desirable – for only a few lightcurves. The small separation between the contours provides justification for the sizes of the training and validation sets. If there were too few patterns in these sets, then the separation would widen. Such widening happens in our network only in a few unimportant regions, which are physically inaccessible (that is, such a combination of input variables gives rise to lightcurves that do not occur in nature). Fourthly, all the unfilled circles have $x_1 < 0.4$ and so lie in the noise-dominated regime. However, the values of $x_2$ indicate the presence of substantial positive excursions. This is already enough to tell us that the noise in the MACHO data is strongly non-Gaussian. Figure 2.8 shows the lightcurves for 8 of the events corresponding to the unfilled circles. For some of these events, it looks as though there are secondary bumps (e.g., event 3). For others, the bump is not properly

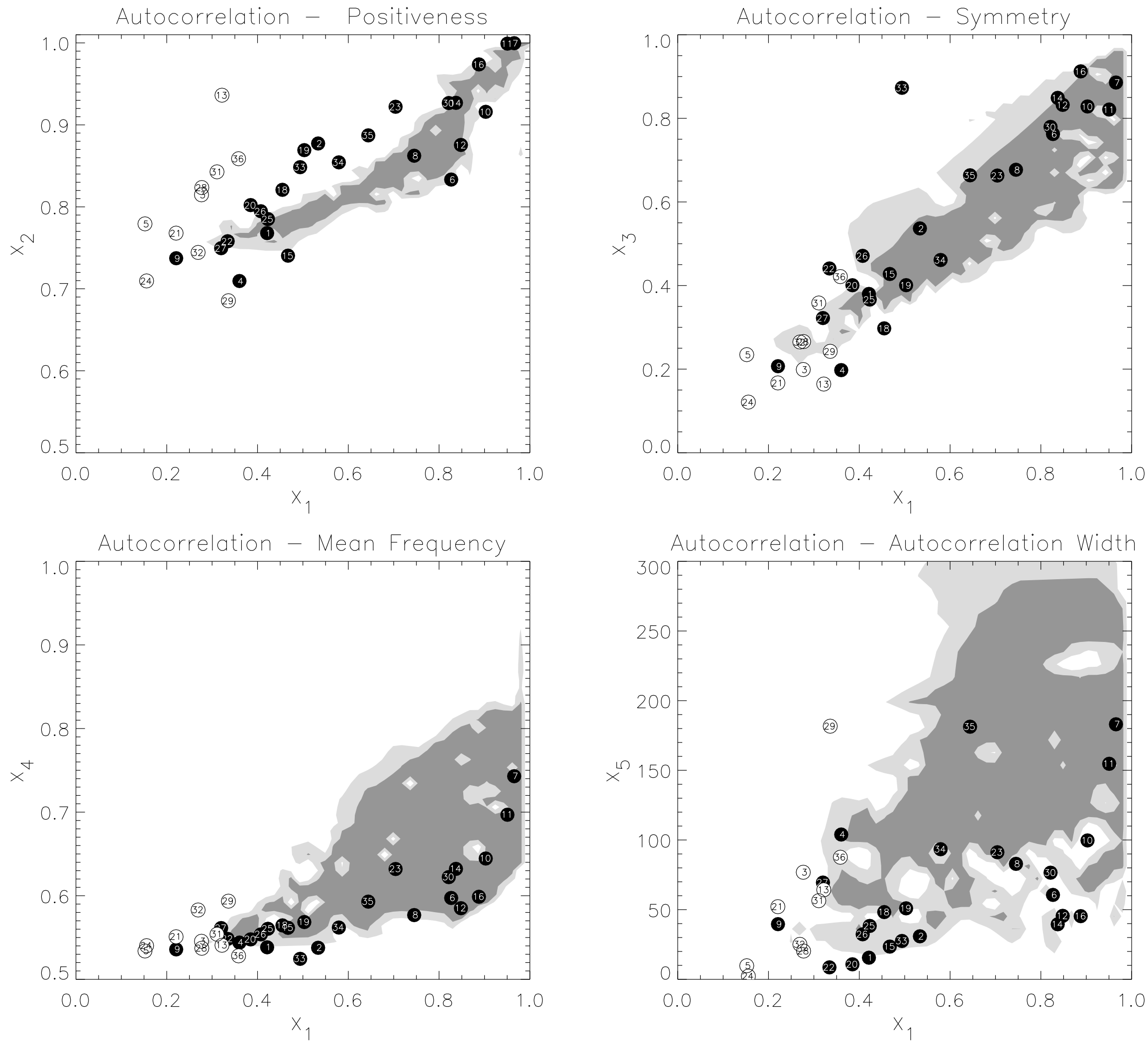


Figure 2.7: The grey-scale contours show the probability of microlensing in the input space $(x_1, \cdots, x_5)$ as judged from the patterns in the training and validation sets. The circles show the locations of the microlensing events identified by MACHO using conventional PSF photometry. Filled circles designate the events also identified in the red filter by the network. Unfilled circles are not identified. Numbers within circles refer to our event designations in Table 2. (Light grey means that the probability is greater than 0.5, dark grey greater than 0.9).

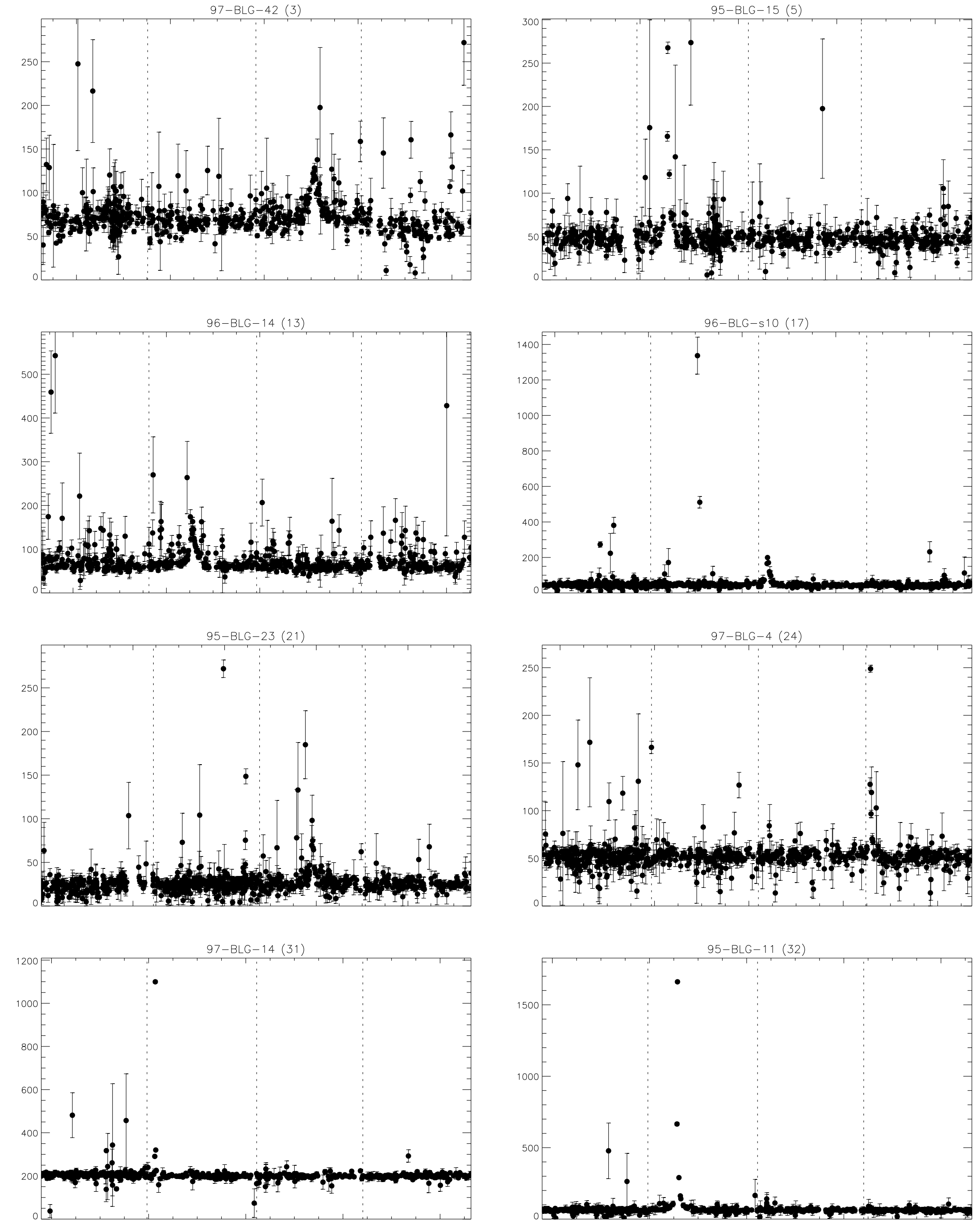


Figure 2.8: This shows the datapoints for eight of the events classified as non-microlensing by the network and as microlensing by the MACHO collaboration. The vertical axis is flux in ADU/s and the horizontal axis is time in days. The data is presented as four strips of 7 month sequences; the 5 months when the bulge is not visible from Australia is marked by the vertical dashed lines.

| ID | MACHO ID | deviation | R | B |
|---|---|---|---|---|
| 1 | 95-BLG-30 | f | 1.00 | 1.00 |
| 2 | 96-BLG-12 | p | 1.00 | 0.99 |
| 3 | 97-BLG-1 | b | 0.95 | 1.00 |
| 4 | 97-BLG-8 | p | 1.00 | 1.00 |
| 5 | 97-BLG-26 | p | 1.00 | 1.00 |
| 6 | 96-BLG-3 | b | 0.83 | 0.51 |
| 7 | 95-BLG-18 | p | 0.99 | 0.75 |

Table 2.3: This shows the output of the committee of neural networks on the exotic events identified towards the bulge in Alcock et al. (2000b). These are all exotic events selected on the basis of the conventional PSF photometry package (SoDoPhot); f stands for deviations due to finite source size, p due to parallactic effects and b due to binarity. The output is the probability that the red and blue data correspond to a microlensing event.

contained (e.g., events 5 and 31) or the bump is overwhelmed by noisy data (e.g., events 13 and 17). It seems that the performance of our network is excellent, as these events certainly need to be looked at with care before accepting a classification as microlensing. However, it is premature to conclude that MACHO have misclassified these events. This is because the MACHO group have re-processed all the lightcurves with difference image analysis (DIA) and this will improve the quality of the lightcurves, reducing noise and contamination from nearby stars. However, without having the DIA lightcurves, we cannot confirm their verdict of microlensing.

### 2.5.2 Exotic events

Some microlensing lightcurves can show deviations from the standard Paczyński form caused by parallactic or finite-source size effects or by binarity and so on (see e.g., Mao & Paczyński 1993, Mao & Di Stefano 1995, Kerins & Evans 1999, Mao et al. 2002). In Table 2.3, all the exotic events identified in Alcock et al. (2000b) using the SoDoPhot photometry package are processed with the committee of neural networks.

Parallactic events (like 96-BLG-12) occur when the Einstein radius projected onto the observer's plane is of the order of an astronomical unit. In such a circumstance, the changing motion of the Earth around the Sun during the event is detectable by an asymmetry in the lightcurve with respect to the peak. Events showing deviations caused by finite source size (like 95-BLG-30) occur whenever the angular size of the source is of the same order of magnitude as the angular Einstein radius. They are usually flatter-topped than the classical Paczyński curves for microlensing by a point source. For both these kinds of deviation, the committee of neural network performs well, as shown in Table 2.3. All the parallactic and finite source size events are identified as microlensing.

However, binarity can cause very substantial deviations. For example, strong binary events have additional peaks, although these can sometimes be missed if sampled irregularly. Weak binary events may just have distortions to the peak or the wings of the lightcurve. Accordingly, we might expect the detection of binary lightcurves to require the training and testing of a new neural network. This is supported by the results in Table 2.3. Here, 96-BLG-12 is identified by the committee, whereas 96-BLG-3 falls into the domain of novelty detection. It is reassuring that in the former case, the event is recognised, while in the latter case, the event is recognised as a new phenomenon. The development of software to recognise binary events is a problem that has not been fully solved by any of the microlensing collaborations to date. It seems reasonable to expect neural networks to play a powerful role here.

## 2.6 Conclusions

This chapter has devised a working neural network that can distinguish simple microlensing lightcurves from other forms of variability, such as eruptive, pulsating, cataclysmic and eclipsing variables. The network is structured to have five input neurons and one output neuron. The inputs and output are separated by a layer of hidden neurons. The simplicity of the network means that it can be trained very quickly and it can be used to process huge datasets in less than a second. Each lightcurve is pre-processed to provide five inputs to be fed to the network. In our application, the five inputs were chosen on physical grounds as good discriminants for microlensing. In other applications, different input variables may be optimum. Our network has been constructed so that the output is the posterior probability of microlensing.

We believe that neural networks offer three important advantages over conventional techniques used in microlensing experiments. First, the decision boundary separating microlensing from non-microlensing may be rather complicated. At present, all microlensing collaborations use a series of cuts (for example, on the goodness of fit to a Paczyński curve, on achromaticity and so on). This is the crudest form of the decision boundary. However, even simple neural networks can reproduce complicated decision boundaries and so the technique is both more efficient and more flexible. Moreover, once a lightcurve has failed to pass a cut at the early stages of a conventional selection process, it is lost for any further analysis. By contrast, neural networks assign relative importance to the input parameters, thus the decision is based on the whole of the information available.

Second, neural networks offer a superior way of calculating the event rate, avoiding the need for any kind of efficiency calculation. The classical procedure of identifying events with cuts is inefficient, and this necessitates the cumbersome Monte Carlo calculation of the numbers of synthetic events passing the cuts. However, a properly-designed neural network can reproduce the decision boundary well and can enable the event rate to be computed directly for comparison with theoretical models, thus completely sidestepping the need for any Monte Carlo calculation of the efficiencies.

Third, novelty detection is made both more precise and easier by neural networks. The conventional approach relies on examination by eye of the events left over after applying a sequence of cuts. For our neural network, we have argued that all lightcurves with outputs between 0.2 and 0.7 may be examples of lightcurves not contained within the training set. These are the events which need looking at very carefully. In the even more massive datasets of the future, it will be important to identify possible novel events as quickly and as efficiently as possible.

From the point of view of microlensing, it is interesting to extend the work in this chapter to include additional effects. Some of the ongoing microlensing experiments are working in the highly blended régime. For example, the POINT-AGAPE (Paulin-Henriksson et al. 2002a,b), WeCAPP (Riffeser et al. 2001) and MEGA (Crotts et al. 2000) collaborations are all monitoring the nearby galaxy M31. Here, the individual stars are not resolved, so the flux in a pixel or superpixel is followed (Baillon et al. 1993). The range of lightcurves in such pixel lensing experiments is very wide – for example, microlensing events can occur in the same superpixel as bright variable stars (e.g., the event PA-99-N1 described in Aurière et al 2001). So, the identification of microlensing events becomes still more daunting. As the complexity of the pattern recognition task increases, as we expect the power and flexibility of the neural network approach to pay increasing dividends. Also, in this chapter, we have concentrated on the microlensing datasets towards the bulge, for which the source stars are often bright. It is important to apply our techniques to the microlensing events towards the Large Magellanic Cloud. Here, the task is harder as the source stars are fainter and there is serious contamination from supernovae in background galaxies. This work will be the subject of a separate publication.

Although our application has been strongly focused on microlensing, the technique is of general applicability in astronomy. There are numerous ongoing or planned massive photometry surveys using robotic telescopes (ROTSE), wide field cameras (WASP and VISTA) and space-borne satellites (Gaia and Eddington). Although the goal of the surveys is different, the basic method is the same – brute force search through many terabytes of data for interesting but rare events, whether planetary transits, cataclysmic variables or optical flashes. We envisage such tasks being routinely devolved to neural networks in the astronomy of the future. In each case, cascades of neural networks could be trained to filter and identify the various classes of variable stars, to pinpoint the target events of interest and to isolate the unexpected or new classes of phenomenon which need looking at very carefully.

## 2.7 Prospects for the future

Suppose the goal is to monitor the whole sky for variability at short time intervals down to 20th magnitude (roughly a billion objects in our Galaxy). In this speculative final section, we ask what is possible now and what will be possible by 2010?

Let us consider the simple situation of a single neural network program running on a single computer. The middle-range hardware situation today is typically a processor running at 2200 Mhz (corresponding to approximately 1000 MIPS or Million Instructions per Second). In order to predict the situation in 2010, we can use "Moore's Law", which says that the numbers of transistors in a processor chip doubles every year or so. Thus, by 2010 the processor speed should be $\sim 100\,000$ MIPS, compared to about 1000 MIPS today. But, to evaluate the progress in run time, we must consider both hardware and the compiler. Benchmarking programs such as SPEC provide us with some clues as to what will be achieved in 2010. If we look at the evolution in performance results on SPEC tests for computers between 1995 and 2000, we find an approximate speed-up factor of 16, or roughly 1.74 per year. We can extrapolate this progress over the 2002-2010 period, which gives a speed-up factor of 85. In other words, both Moore's Law and the extrapolation of benchmarking suggest rather similar speed-up factors of roughly two orders of magnitude by 2010.

The time required to run the neural network itself is negligible compared to the time required to run the pre-processing, which extracts the parameters used by the neural network. Our present pre-processing program requires $10^{-4}$ s to analyse 100 data points for a single star. We have chosen 100 datapoints as it might correspond to sampling 3 times a night for one month, which is reasonable for the detection of fast transient events. Alternatively, it might correspond to sampling once a night for 3 months, which is reasonable for the detection of variability like microlensing with a characteristic timescale of $\sim 1$ month. At present, it therefore takes $\sim 10^5$ s (or over a day) to analyse such dataset for the whole sky. By 2010, it will take only 20 minutes for such a program to run on the whole sky (using the speed-up factor of 85). More generally, the time taken in seconds to analyse a set of $N_{\rm pts}$ data points for $N_\star$ stars in 2010 is

$$t \sim 2 \times 10^{-9} N_\star N_{\rm pts} \log N_{\rm pts} . \tag{2.8}$$

Let us assume there are 8 hours of observing time a night and that we wish to process a months data for the whole sky in real-time. Then we can derive the real-time equation

$$t^2 \sim 1.7 \times 10^6 \, (13.7 - \log t) \, . \tag{2.9}$$

which has a solution $t \sim 50$ minutes. In other words, real-time processing of variable phenomena across the entire sky down to 20th magnitude will be possible for sampling rates of $\gtrsim 1$ hr by 2010.

Our speculative calculation errs on the pessimistic side because we have not taken into account any correction for application of parallel processing or the fast developing GRID technology for high performance computing. However, it surely does enough to convince the reader that, properly trained, neural networks can analyse huge datasets very quickly. This will become one of the methods of choice for data-mining in the massive variability surveys of the very near future.

## 2.8 Bibliography


Afonso C. et al., 2003, A&A, 404, 145

Alcock C. et al., 1997, ApJ, 486, 697

Alcock C. et al., 2000a, ApJ, 542, 281

Alcock C. et al., 2000b, ApJ, 541, 734

Allsman R.A., Axelrod T.S., 2001, astro-ph/0108444

Andreon S., Gargiulo G., Longo G., Tagliaferri R., Capuano N. 2000, MNRAS, 319, 700

Ansari R. et al., 1995, AA, 299, L21

Ansari R. et al., 1996, AA, 314, 94

Morelli P.L., 1996, AA, 314, 541

Aurière M. et al., 2001, ApJ, 553, L137

Bailer-Jones C.A.L., Irwin M., Gilmore G., von Hippel T., 1997, MNRAS, 292, 157

Baillon P., Bouquet A., Giraud-Heraud, Y., Kaplan J., 1993, AA, 277, 1

Bishop C., 1995, Neural Networks for Pattern Recognition, Oxford University Press, Oxford

Brancewitz H.K., Dworak T.Z., 1980, Acta Astron, 30, 501

Conway A.J., 1998, New Astronomy Reviews, 42, 343

Crotts A., Uglesich R., Gould A., Gyuk G., Sackett P., Kuijken K., Sutherland W., Widrow L., 2000, In "Microlensing 2000: A New Era of Microlensing Astrophysics", eds. J.W. Menzies and P.D. Sackett, ASP Conference Series, vol. 239, p. 318, ASP, San Francisco.

Hamuy M., Phillips M.M., Suntzeff N.B., Schommer R.A., Maza J., Smith R.C., Lira P., Aviles R., 1996, AJ, 112, 2438

Kerins E.J., Evans N.W., 1999, ApJ, 517, 734

Lahav O. et al. 1995, Science, 267, 859

Lasserre, T. et al., 2000, AA, 355, L39

Mao S., di Stefano R., 1995, ApJ, 440, 22

Mao S., Paczyński B., 1991, ApJ, 374, L37

Mao S. et al., 2002, MNRAS, 329, 349

Müller B.,Reinhardt J., Strickland M.T., 1995, Neural Networks: An Introduction, Springer Verlag, Berlin

Paczynski B., 1986, ApJ, 304, 1

Paczyński B., 2001, In "Mining the Sky", eds A.J. Banday, S. Zaroubi, and M. Bartelmann, p. 481, Springer Verlag, Berlin (astro-ph/0110388)

Paczyński B., 2002, In "Small Telescope Astronomy on a Global Scale", eds W.P. Chen, C. Lemme, B. Paczyński, ASP Conference Series, vol 246, in press, ASP, San Francisco. (astro-ph/0108112)

Paulin-Henriksson S. et al. 2002a, ApJ, 576, L121

Paulin-Henriksson S. et al. 2002b, astro-ph/0207025

Perdang J., Serre T., 1998, A&A, 334, 976

Press W.H., Rybicki G.B., 1989, ApJ, 338, 277

Press W.H., Teukolsky S., Vetterling W.T., Flannery B., 1992. Numerical Recipes, Cambridge University Press, Cambridge, 2nd ed. chap. 13.

Riffeser A. et al. 2001, AA, 379, 362

Storrie-Lombardi M.C., Lahav O., 1994, Vistas in Astronomy, 38, 249

van Genderen A.M., 1995, AA, 304, 415

Udalski A., Szymanski M., Kaluzny J., Kubiak M., Mateo M., Krzeminski W., & Paczynski B., 1994, Acta Astronomica, 44, 227

Wozniak P.R. et al., 2001, American Astronomical Society Meeting, 199, 130.04

# Chapter 3

# Transient Events towards the LMC

This chapter presents a new analysis of the microlensing dataset towards the Large Magellanic Cloud. The value of the microlensing optical depth towards the LMC is of high importance since it measures the density of compact objects in the halo of our Galaxy. There is, however, some controversy regarding the numbers of candidate events presented by different microlensing collaborations (§3.1). The techniques exploited here were devised in the previous chapter. In this work, a number of modifications is introduced to improve the classifier performance. This concerns the error function calculation, network training procedure and the output error estimation (§3.2). The identification of microlensing events is performed using two neural networks – the first discriminates against variable stars and the second against supernovae (§3.3). The MACHO candidate events from both set A and set B are processed in §3.4. Finally, in §3.5, an algorithm is devised for direct calculation of the microlensing rate from the output of the neural networks.

## 3.1 Introduction

Microlensing is rare and outnumbered by stellar variability by at least a factor of ten thousand. Despite this, the selection of microlensing candidates in variability surveys seems straightforward at an optimistic first glance. Unlike almost all forms of stellar variability, microlensing is achromatic, time-symmetric and does not repeat. The theoretical form of the microlensing lightcurve is well-known (e.g., Paczyński 1986) and so events can seemingly be selected by their goodness-of-fit in two passbands.

In practice, the selection of candidates is fraught with difficulties. The lightcurves are usually sparsely sampled and noisy (for example, the median seeing at the site of one of the most prominent microlensing experiments is $\sim 2.0''$). More awkwardly still, the clear-cut set of characteristics of microlensing only holds good in the simplest case of an isolated point-mass lensing a point-source. In fact, microlensing lightcurves may show colour variations because of blending (e.g., Di Stefano & Esin 1995). They may show substantial deviations from time-symmetry because of parallax or xallarap effects (Dominik 1998; Mao et al. 2002) or because the lens is a binary star (e.g., Mao & Paczyński 1991).

As a consequence, the results of the microlensing experiments towards the Magellanic Clouds by the MACHO and EROS collaborations remain controversial (e.g., Evans 2002). From 5.7 years of data, the MACHO collaboration identified between 13 and 17 candidates towards the Large Magellanic Cloud (LMC) and reckoned that the optical depth is $1.2^{+0.4}_{-0.3} \times 10^{-7}$ (Alcock et al. 2000). The first set of 13 events comprises the most convincing candidates, whilst the second set of 17 candidates includes an additional 4 events less firmly established. This is in astonishing contrast to the results reported by the EROS collaboration, who found just 3 events towards the LMC (Lasserre et al. 2000). The two experiments are not directly comparable as EROS monitor a wider solid angle of less crowded fields than do MACHO. Even though EROS do not analyze their data in terms of optical depth, it is clear that the results point to a lower value than that claimed by MACHO. Tellingly, a similar discord prevails in the results towards the Galactic Centre; MACHO (Alcock et al. 1997) recorded that the microlensing optical depth to the red clump stars as $3.9^{+1.8}_{-1.2} \times 10^{-6}$, while EROS (Afonso et al. 2003b) found a value of $0.94 \pm 0.26 \times 10^{-6}$ at almost the same location. These discrepancies strongly suggest that the systematic effects in the experiments are not yet fully understood, with candidate selection fingered as the most likely culprit.

All this motivated us to introduce neural networks as an automatic way of classifying lightcurve shapes in massive variability surveys. In Chapter 2 we constructed a working neural network for identification of microlensing events and applied it to microlensing data towards the Galactic Centre. In this work, the ideas and methods of analysis are extended to the variability datasets taken towards the LMC. This is a harder problem, as the source stars are fainter and hence the microlensing events less clear-cut. A particular difficulty already identified by Alcock et al. (2000) is the contamination of samples of microlensing events by supernovae in distant galaxies behind the LMC.

## 3.2 Lightcurve classification with neural networks

Let us briefly review the main stages of a classification routine with neural networks (see Bishop 1995 for more details). As a first step, the lightcurves are pre-processed with the primary goal of reducing the amount of data to be examined. Features can be extracted automatically, for example, with the help of spectral analysis or principle component analysis. Alternatively, we can try to incorporate *a priori* information and use only those features that are believed to quantify characteristic properties of the lightcurve, such as shape, periodicity or colour. These features are then normalized to provide inputs for the neural network. An optimum choice of inputs is the key to success.

| Variable Type | Specific Examples | Number |
|---|---|---|
| Eruptive | S Doradus, R Corona Borealis stars | 25 |
| Pulsating | RV Tauris, Mira, Semi-Regular variables | 384 |
| | Cepheids | 124 |
| | Bumpers | 100 |
| Cataclysmic | Supernovae, novae, recurrent novae | 52 |
| Eclipsing | | 54 |
| MACHO samples | | 400 |
| Microlensing | | 800 |

Table 3.1: Composition of the training set.

The next stage involves choosing a particular architecture for the neural network (such as the number of hidden units or layers) and training the network on the set of previously classified patterns of inputs $x$. The logistic activation function is used and the output neuron takes values in the range between 0 and 1. Thus, the output $y$ models the posterior probability of the variability classes (see e.g., Bishop 1995 or Chapter 2). Training is performed by minimizing the error function, which consists of the standard cross-entropy term and the weight decay term $\alpha \sum_i w_i^2$, where the sum runs over all weights $w_i$. Adjusting a hyperparameter $\alpha$ enables one to control the magnitude of weights and hence to minimise any over-fitting. This can be done automatically during training. This differs from the procedure used in Chapter 2, as no validation set is required and the whole of the available data can be used as a training set. Further reduction of the variance in network predictions can be achieved by using a committee of networks. A very inexpensive but efficient way of introducing the committee involves simply taking the output of the committee to be the average of the outputs of the individual networks. The members of the committee are competing solutions of the classification problem, which occurred as a result of starting the search in the parameter space from different initial weights. It is also beneficial to combine networks with different numbers of neurons in the hidden layer. Finally, each new lightcurve has to be pre-processed and the features extracted have to be fed to the trained network which is defined by the most probable parameter vector of weights $w_{MP}$. The output of the network is $P(C_1|x,w)$, the probability that the lightcurve belongs to the class $C_1$ or microlensing given the inputs $x$ and the weights $w$. The output can therefore then be used to make a decision as to which class the current datum belongs. Usually, the lightcurve is assigned to the class for which the posterior probability is largest. For a two-class problem with equal priors this implies a formal decision boundary at $y = 0.5$. Although usually different classes do have roughly equal prior probabilities in the training set, in reality this need not be the case. One can correct for this by adjusting the outputs of the trained network using the ratios of prior probabilities for each class (see §3.5.2).

Once we have transformed the new input pattern into the posterior probability, it is important to have an estimate of the error in the output. The error arises through variance and through undersampling in the parameter space during training. The variance part of the output error is easiest to deal with. It can be approximated by taking the standard deviation of the output of a committee of neural networks. The second part of the output error is more awkward, but can be approximated by a method originated by MacKay (1992), which we now explain.

There will always be regions in input space with low training data density. Typically the network with parameters $w_{\rm MP}$ will give over-confident predictions in such regions. A representative output then will be an output averaged over the distribution of network weights, namely

$$P(C_1|x,D) = \int P(C_1|x,w)p(w|D)dw. \qquad (3.1)$$

Here, $C_1$ is the class (in our case, microlensing), $x$ denotes the inputs and $D$ the data in the training set. This integration cannot be performed analytically, but there is a simple approximation, namely

$$P(C_1|x,D) \approx f(k(s)a_{\rm MP}), \qquad k(s) = \left(1 + \frac{\pi s^2}{8}\right)^{-1/2}. \qquad (3.2)$$

Here, $f$ is the activation function, $s$ is the network variance and $a_{\rm MP}$ is the activation of the output neuron given the most probable distribution of weights (the one that is found during network training). The network variance is calculated using the methods of Section 10.3 of Bishop (1995). It can be shown that this marginalized or moderated prediction always has a value closer to 0.5 than the most probable one. Marginalization always drives the output closer to the decision boundary.

## 3.3 A cascade of networks

Neural networks can be arranged sequentially in a cascade to perform complicated pattern recognition tasks. Here, the lightcurve data are examined first with neural networks which eliminate the contaminating variable stars. Then, lightcurves successfully passing this first stage are analysed anew with neural networks which eliminate contaminating supernovae. Excellent microlensing candidates must pass both stages.

### 3.3.1 A network to remove the variable stars

To eliminate the variable stars, we use the techniques developed in Chapter 2, but we make some slight modifications to the training procedures. The training set contains $\sim$ 2000 patterns, 800 of which are extracted from simulated microlensing lightcurves. We generate microlenisng lightcurves choosing the impact parameter, timescale and time of the peak from uniform distributions. Random Gaussian noise is added to all the lightcurves and the experimental sampling is used. Mira-type lightcurves are produced from the long data sequences provided by the American Association of Variable Star Observers (AAVSO). Long period Cepheids are constructed from their Fourier coefficients (e.g., Antonello & Morelli 1996). Artificial bumper lightcurves of a simple sinusoid shape with period chosen randomly around the experiment lifetime are also used. Simulated microlensing events are generated by randomly choosing an impact parameter, an Ein-

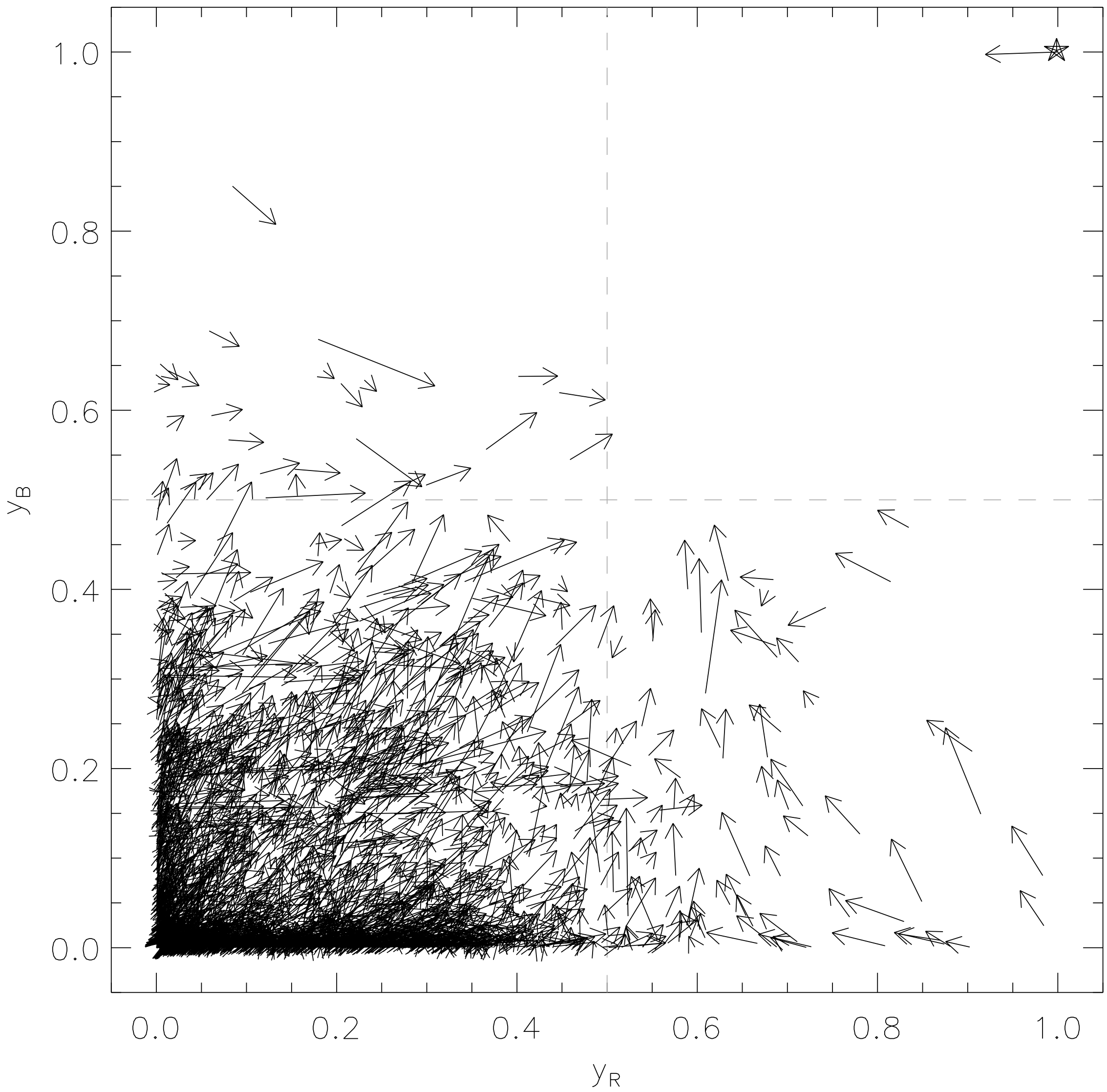


Figure 3.1: This shows the output of the committee of neural networks for $\sim$ 2500 lightcurves in tile 6.5845. Arrows connect most probable and marginalized predictions for each pattern. The star shows the location of the lightcurve 6.5845.1091, which is the MACHO candidate numbered 5 in the nomenclature of Alcock et al. (2000).

stein crossing time between 7 days and 365 days and a time when the event reaches maximum. Only those events that have five or more datapoints during the event with a signal-to-noise greater than 5 are included in the training set. (We return to this point in §3.5 dealing with the efficiencies).

All the lightcurves are subjected to a spectral analysis to extract parameters which are the inputs to the neural networks. Chapter 2 already devised 5 parameters, based on the underlying premise that microlensing events are single, symmetric, positive excursions from the lightcurve baseline. The same parameters are used here.

All networks are trained using the Netlab package (Nabney 2002). The optimization method is the variable metric or quasi-Newton algorithm with Broyden-Fletcher-Goldfarb-Shanno updates (see Press et al. 1992; Nabney 2002). The optimization is performed several times in sequence with values of fractional tolerance decreased from $10^{-3}$ to $10^{-6}$ by repeatedly halving. At the end of each convergence loop, the hyperparameter $\alpha$ is adjusted. To find the optimal network architecture, we compared different solutions with between 2 and 12 hidden neurons. The data mismatch (or difference between target and output summed over all the patterns in the training set) shows very little decline for networks with more than 7 hidden units. However, for networks with less than 5 hidden units, the data mismatch increases very quickly. Thus, we choose to combine networks with 5, 6 and 7 hidden units to form a committee comprising in total 30 networks.

The committee is then tested on the set of features extracted from the lightcurves in MACHO tile 6.5845 towards the LMC. We process only lightcurves with more than 250 measurements, which is not unreasonable for the MACHO survey which has a lifetime in excess of 7 years. This leaves us with $\sim$ 2500 lightcurves, one of which is a microlensing event. Figure 3.1 shows the probability of microlensing given the red and blue data for each lightcurve in this tile. Arrows connect the predictions using most probable distribution of weights with the marginalized outputs. Note that the single microlensing event has been unambiguously separated from the abundant variable stars.

The red and blue data for the MACHO candidate microlensing events towards the Large Magellanic Cloud given in Alcock et al. (2000) are then processed with the network and the outputs recorded in the first two columns of Table 3.2. We will discuss the results in detail in §3.4.

### 3.3.2 A network to remove the supernovae

To distinguish microlensing from supernovae occuring in background galaxies is more problematic, as clearly pointed out in Alcock et al. (2000). This is the job of the next network in the cascade.

Gravitational microlensing of a point-source on a point-mass dark lens moving with a constant velocity produces a symmetric brightness change due to distortion of spacetime near the mass. A supernova lightcurve is generated by an exploding star and is characterised by a very quick rise followed by a steady decline. Based upon this knowledge, we might hope to use the symmetry of the lightcurve as a discriminant feature. However, microlensing lightcurves can appear much less symmetric when the observational campaign has irregular time sampling or when the beginning/end of the event is missed. On the other hand, supernovae lightcurves can seem symmetric if only the top part of the lightcurve is sampled. This happens because distant supernovae are generally faint objects and only briefly enter the magnitude range of the survey.

Colour evolution during the event is another important discriminant. The colours change dramatically during a supernova explosion as a result of complicated radiation processes inside the ejecta. After a fairly constant pre-maximum epoch with $B-V \approx 0$, a supernova of type Ia typically starts turning red at the time of the maximum light, it

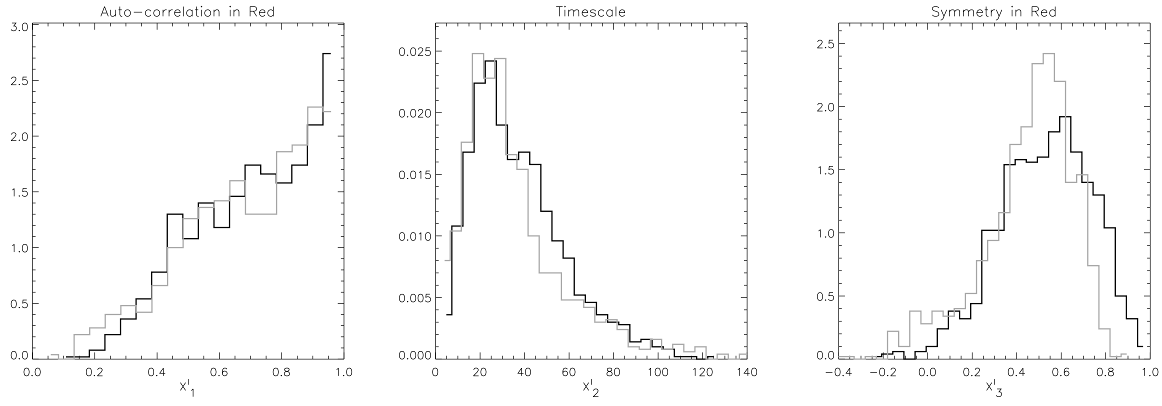


Figure 3.2: This shows the distributions of lightcurve shape features for microlensing (black) and supernovae (grey) in the training set. The timescale $x'_2$ is shown in days, while the autocorrelation coefficient $x'_1$ and the symmetry measure $x'_3$ are dimensionless.

reaches $B - V \approx 1$ in about 30 days and then drops back (see e.g., Phillips et al. 1999). This can be contrasted with the colour behaviour during gravitational microlensing. Gravity bends light irrespective of its frequency, therefore colour does not change during microlensing. However, this is only true if the source star is resolved and the lens is dark. The presence of other stars within the centroid of light or lensing by a luminous object will result in the colour change during the event. At the baseline, the colour is defined by the combined flux from all the sources. The amplified star will contribute most of the colour around the peak. The colour of a microlensing event can become redder or bluer, depending on the population of the blend, but it usually changes symmetrically about the peak with substantial correlation between passbands (see e.g., Di Stefano & Esin 1995, Buchalter, Kamionkowski, & Rich 1996).

Again, we build a training set with patterns of features extracted from simulated microlensing and supernova lightcurves. Then, a committee of networks is trained and applied to the lightcurves of all transients found at the first stage of the data mining. In the training set, simulated microlensing lightcurves have a slightly different timescale distribution as compared to §3.3.1. The value of the Einstein diameter crossing time is the absolute value of a random number drawn from a Gaussian distribution with zero

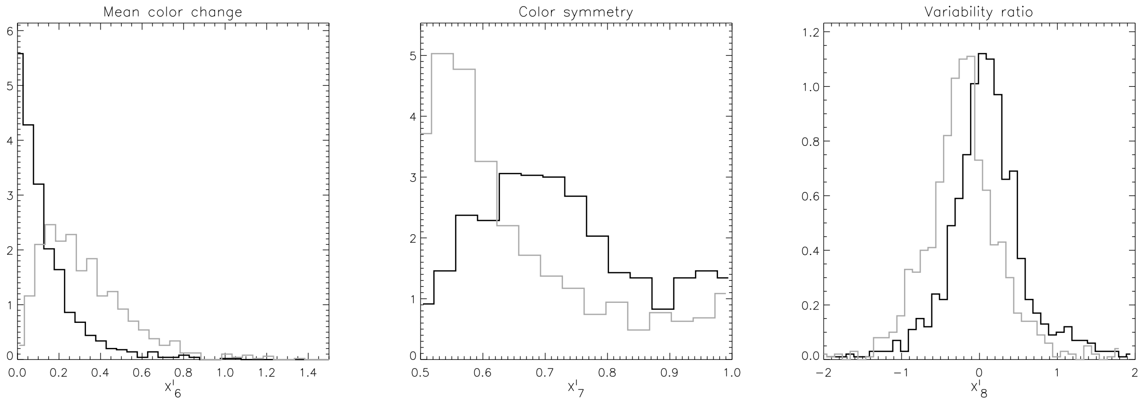


Figure 3.3: This shows distributions of colour features for microlensing (black) and supernovae (grey) in the training set. Mean colour change $x'_6$ is in magnitudes, $x'_7$ is mapped from $(0,\infty)$ to $(0.5,1)$ with the sigmoid function and $x'_8$ is in logarithmic measure.

mean and standard deviation of 75 days. This is done to ensure that the set is dominated by fast transients, for which confusion with supernova lightcurves is most problematic. Blending is also added by changing the amplification to $(1 - f_{B,R}) + Af_{B,R}$ , where $A$ is the unblended amplification and the blending fractions in blue and red pass-bands $f_{B,R}$ are the absolute values of a random number drawn from a Gaussian distribution with unit mean and standard deviation of 0.4.

We generate supernova lightcurves of type Ia only, as they are the most luminous and hence should be the dominant contaminant in any sample. For the templates, we use $R$ and $B$ pass-band data of supernova SN 1991T from Lira et al. (1998). This is an unusually bright supernova; however our algorithm chooses a random magnitude at maximum so only the shape of the lightcurve is important. The $R$ and $B$ colours from Lira et al. do not match MACHO pass-bands exactly since MACHO imaging was performed in non-standard red ($\lambda\lambda$ 5900-7800 $\AA$) and blue ($\lambda\lambda$ 4370-5900 $\AA$) filters. This should not be a serious concern since the training set data-cloud is smoothed by noise and irregular sampling. The simulated supernova lightcurve is a randomly chosen part of the top of the supernova template. We allow for extinction in the host galaxy by permitting the lightcurves in the blue and red passbands to have slightly different amplitudes. The total detected brightness change in magnitudes is $2.5 \log[(u^2+2)/u\sqrt{u^2+4}]$, where $u$ is distributed uniformly between 0 and 1. In this way, the typical signal in the subset of supernovae events in the training set correlates with the typical signal in subset of microlensing events. All the lightcurves have Gaussian noise added and are sampled with actual MACHO sampling.

To describe the shape of the lightcurve, we extract the following features. First, $x'_1$ is the maximum value of the autocorrelation coefficient. It can be regarded as a measure of the signal in the lightcurve. To make the feature extraction more robust, we take advantage of the fact that the lightcurve has already passed the first stage of classification. So we can assume that the epoch of the maximum light has been estimated by the first neural network. Thus, the second feature $x'_2$ is simply the time between the peak and an amplification of 1.34. For microlensing events, this corresponds to the Einstein radius crossing time. For supernova lightcurves, this feature is well-defined but does not correspond to anything with simple physical meaning. The third feature $x'_3$ is the cross-correlation of the lightcurve with the time-reversed lightcurve. Here, we use only the data-points within a timescale $x'_2$ of the maximum in both the forward and backward directions (the Einstein diameter crossing time for microlensing). The time of maximum brightness defines the lag of the cross-correlation, i.e. the reversed lightcurve is shifted to match the actual epoch of maximum light. The parameters $(x'_1, x'_2, x'_3)$ are all extracted from the red lightcurve. The fourth $x'_4$ and the fifth $x'_5$ features are the autocorrelation and symmetry parameters extracted from the blue lightcurves.

Additionally, we feed the network with features characterizing the colour change during the event. Note, that when the signal to noise of the transient is low or when the colour change is minuscule, then error propagation might result in the destruction of any colour signal. In other words, any signal in the colour is noisier than the corresponding signal in the red or blue passbands separately. Irregularity of the campaign time sampling can further aggravate the problem, since not all the measurements are taken simultaneously in both colours. To account for this and to stabilize the colour, we extract all the following features from lightcurves binned with a time bin-size of 2 days. To estimate the total colour change during the event, we calculate the weighted average excursion from the colour baseline:

$$x'_6 = \sum_{i=1}^{n} \frac{|(B-R)_i - (B-R)_0|}{\sigma^2_{B-R,i}} \Bigg/ \sum_{i=1}^{n} \frac{1}{\sigma^2_{B-R,i}}. \tag{3.3}$$

Here, the index $i$ runs through all measurements within the Einstein diameter crossing time and the baseline $(B-R)_0$ is the weighted average colour outside the Einstein crossing time. The next feature $x'_7$ is the ratio of total weighted absolute colour change before and after the maximum light. This tests the symmetry of the colour signal. For microlensing, this ratio takes values around 1, while for supernova lightcurves it is close to zero. Therefore, we magnify the range between 0 and 1 by transforming the ratio with the sigmoid function. Finally, the last colour feature is the variability ratio as defined by Welch & Stetston (1993). It is the ratio of the total normalized magnitude residuals in the blue and red filters:

$$x'_8 = \sum_{i=1}^{n} |\delta B| \Bigg/ \sum_{i=1}^{n} |\delta R|, \qquad \delta B(R) = \frac{B_i(R_i) - \overline{B}(\overline{R})}{\sigma_{B_i(R_i)}} \tag{3.4}$$

Here the weighted means $\overline{B}, \overline{R}$ are calculated over all epochs outside the Einstein crossing time. We take the logarithm of the variability ratio so as to compress the range. Supernovae lightcurves have, on average, smaller values of $x'_8$ than microlensing lightcurves.

The distributions of lightcurve shape features are shown in Figure 3.2. It is clear from the first two panels that $x'_1$ and $x'_2$ serve as control features. The autocorrelation and timescale distributions of supernova and microlensing lightcurves do not differ much. This is reassuring since it indicates that we are probing similar signal regimes of the two different variability classes. The distribution of $x'_3$ (the third panel of Figure 3.2) confirms our choice of this feature as a symmetry measure with microlensing dominating around values of unity.

Figure 3.3 shows the distribution of colour related parameters. From the first panel, it follows that, as expected, the amplitude of the colour change is significantly lower for microlensing. Note, however, that there is a tail in the $x'_6$ distribution that stretches as far as 1.5 magnitudes for both microlensing and supernovae. The colour signal looks very symmetric for microlensing with $x'_7$ peaking at $\sim 0.7$. Let us recall that the original colour symmetry ratio was transformed with the sigmoid function, which means that 1 is mapped onto value $\sim 0.73$. The distribution of $x'_7$ for the supernova lightcurves peaks around 0.55, which corresponds to a value of 0.2 in the symmetry ratio. Finally, the variability ratio $x'_8$ is presented in the third panel of this figure. The mean value of the logarithm of $x'_8$ for microlensing is zero and the distribution itself is symmetric, while supernovae prefer smaller values of this feature, typically by factor of $10^{-0.2} \simeq 1.6$.

The total number of patterns in the training set is 2000, one half are extracted from microlensing lightcurves and the other half from the simulated lightcurves of supernovae. For networks with more than 5 neurons, the data misfit changes from roughly exponential to monotonic decrease. We therefore choose to use 10 networks with 5 hidden units to form the committee. The candidate microlensing events towards the Large Magellanic Cloud are then processed with the network and the outputs recorded in the third column of Table 3.2. The output can be interpreted as the probability that the lightcurve is not a supernova.

| Event | $y_R$ | $y_B$ | $y'$ |
|---|---|---|---|
| 1a | 0.95 ± 0.05 | 0.76 ± 0.19 | 0.97 ± 0.01 |
| 1b | 0.95 ± 0.05 | 0.98 ± 0.02 | 0.95 ± 0.01 |
| 4 | 0.90 ± 0.13 | 0.83 ± 0.22 | 0.90 ± 0.02 |
| 5 | 0.95 ± 0.08 | 0.97 ± 0.04 | 0.74 ± 0.18 |
| 6 | 0.76 ± 0.21 | 0.99 ± 0.01 | 0.97 ± 0.02 |
| 7a | 0.97 ± 0.03 | 0.95 ± 0.05 | 0.84 ± 0.10 |
| $7b^{*}$ | 0.11 ± 0.14 | 0.11 ± 0.17 | 0.21 ± 0.05 |
| 8 | 0.97 ± 0.03 | 0.22 ± 0.14 | 0.86 ± 0.04 |
| $9^{*,\mathrm{binary}}$ | 0.50 ± 0.28 | 0.67 ± 0.24 | 0.67 ± 0.13 |
| $10a^{\mathrm{SN}}$ | 0.94 ± 0.07 | 1.00 ± 0.00 | 0.82 ± 0.12 |
| $10b^{\mathrm{SN}}$ | 0.96 ± 0.07 | 0.99 ± 0.02 | 0.88 ± 0.01 |
| $11^{*,\mathrm{SN}}$ | 0.97 ± 0.04 | 0.75 ± 0.25 | 0.05 ± 0.01 |
| $12a^{\mathrm{SN}}$ | 0.73 ± 0.24 | 0.46 ± 0.30 | 0.01 ± 0.01 |
| $12b^{\mathrm{SN}}$ | 0.17 ± 0.20 | 0.25 ± 0.25 | 0.42 ± 0.25 |
| 13 | 0.21 ± 0.20 | 0.33 ± 0.29 | 0.96 ± 0.04 |
| 14 | 0.87 ± 0.15 | 0.97 ± 0.04 | 1.00 ± 0.00 |
| 15 | 0.20 ± 0.38 | 0.08 ± 0.11 | 0.84 ± 0.03 |
| $16^{*,\mathrm{SN}}$ | 0.01 ± 0.01 | 0.13 ± 0.08 | - |
| $17^{*,\mathrm{SN}}$ | 0.01 ± 0.01 | 0.04 ± 0.05 | 0.04 ± 0.01 |
| 18 | 0.76 ± 0.11 | 0.72 ± 0.25 | 0.95 ± 0.03 |
| $19^{*,\mathrm{SN}}$ | 0.17 ± 0.15 | 0.06 ± 0.07 | 0.07 ± 0.06 |
| $20^{*}$ | 0.68 ± 0.26 | 0.16 ± 0.23 | 0.23 ± 0.20 |
| 21 | 0.96 ± 0.03 | 0.96 ± 0.03 | 1.00 ± 0.00 |
| 22 | 0.85 ± 0.19 | 0.93 ± 0.08 | 0.98 ± 0.01 |
| 23 | 0.85 ± 0.20 | 0.94 ± 0.08 | 0.96 ± 0.01 |
| $24^{*,\mathrm{SN}}$ | 0.88 ± 0.13 | 0.89 ± 0.10 | 0.61 ± 0.26 |
| 25 | 0.95 ± 0.09 | 0.95 ± 0.08 | 0.98 ± 0.01 |
| $26^{*,\mathrm{SN}}$ | 0.62 ± 0.20 | 0.33 ± 0.26 | 0.87 ± 0.02 |
| $27^{*}$ | 0.13 ± 0.09 | 0.09 ± 0.06 | 0.70 ± 0.01 |

Table 3.2: This shows the output of the committee of neural networks (the posterior probability of microlensing) on the subset of candidates towards the LMC. Stars mark events that did not pass MACHO's selection criteria A. A superscript SN marks a supernova as judged by Alcock et al. (2000). The first two columns ($y_R$ and $y_B$) are the outputs of the network of §3.3.1 on the red and blue data, the third column ($y'$) is the output of the network of §3.3.2.

## 3.4 New light on the MACHO candidates

First, let us recall that Alcock et al. (2000) used a series of conventional cuts to identify microlensing events. The set A selection criteria are "designed to accept high quality microlensing candidates". The set B criteria are "designed to accept any light curves with a significant unique peak and a fairly flat baseline". 19 lightcurves pass the set A criteria and 29 pass the looser set B. Sometimes the same source star has two lightcurve because, for example, it lies in an overlap region. Eight of the 29 events (1a, 1b, 7a, 7b, 10a, 10b, 12a and 12b) correspond to just four stars. Finally, Alcock et al. apply a supernova cut, insisting that a blended microlensing lightcurve is a better fit than a SN Ia template. This finally leaves 13 events in set A (events 1, 4-8, 13-15, 18, 21, 23 and 25) and 17 events in set B (everything in set A together with 9, 20, 22 and 27). Subsequently, event 22 was confirmed to be a Seyfert galaxy and so can be removed from set B (Sutherland, private communication).

### 3.4.1 Microlensing versus variable stars

Table 3.2 shows the predictions of committees of neural networks for the LMC microlensing candidates selected by MACHO. First, let us concentrate on the output in the first two columns which is provided by the committee of neural networks to eliminate variable stars (see §3.3.1). Let us recall that the output $y$ is the posterior probability of microlensing.

In total, 10 out of 13 candidates from MACHO set A receive $y > 0.5$ in both red and blue filters: 1, 4-7, 14, 18, 21, 23, 25. However, some of these events are not identified securely, which is reflected in the somewhat lower values of the probability and the large error-bars. For example, event 6 is identified with a probability $0.76 \pm 0.26$ in the red filter, compared to $0.99 \pm 0.01$ in the blue. This can be explained by the presence of

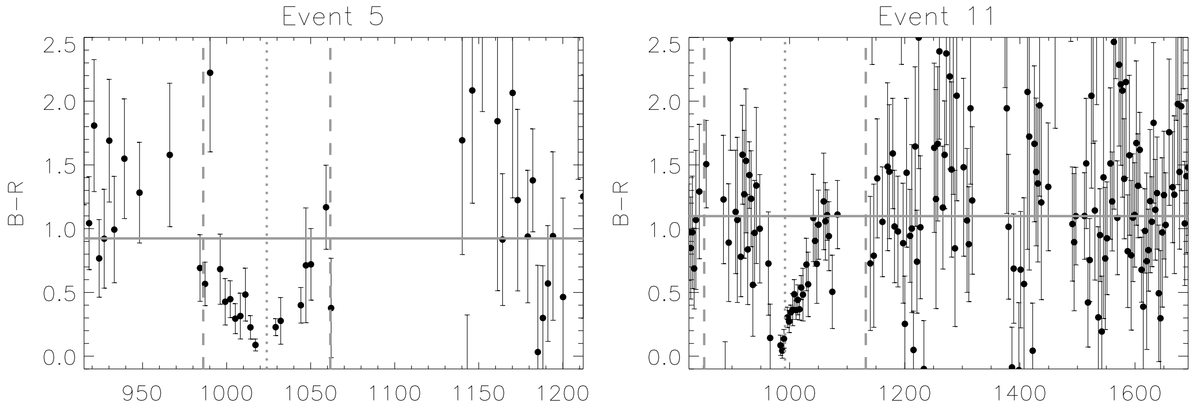


Figure 3.4: This shows the colour evolution of events 5 and 11. Event 5 shows a colour shift that changes symmetrically about the peak in the flux of the event. This is characteristic of blended microlensing events. Event 11 is a supernova candidate, as evidenced by the stable colour in the pre-maximum epoch, the rapid reddening after maximum, followed by the colour becoming increasingly blue at late times. The classical supernova colour curve as depicted in Lira et al. (1998) is shifted because of extinction in the host galaxy. The vertical axis is $B-R$ in magnitudes and the horizontal axis is date in JD-2448000. The dotted vertical line is the peak of the event, while the dashed vertical lines mark the time over which the amplification exceeds 1.34.

secondary bump in the red lightcurve $\sim 6$ years after the main peak, which is absent in the blue (see Fig 3.6). Event 14 has a dip $\sim 2$ years after the main maximum in the red pass-band. Accordingly, $y_R$ for this event is $0.87 \pm 0.15$, compared to $y_B = 0.97 \pm 0.04$. Another candidate, event 18 has $y_B = 0.72 \pm 0.25$. This is a low signal-to-noise event, with one of the smallest maximum amplifications $A_{max} = 1.54$.

Three events from MACHO set A have $y < 0.5$. Both events 13 and 15 are noisy with no stable baseline (see Fig 3.5). Candidate 8 is classified as non-microlensing with $y_B = 0.22 \pm 0.14$. Indeed, it has an asymmetric shape, as the beginning of the event is lacking due to the gap in the observational campaign (Fig 3.5). Note also that candidate 10 which has passed MACHO selection criteria A is classified with probability $y_{R,B} > 0.9$. This event was identified as a supernova by the MACHO group. The majority of the lightcurves that were selected by MACHO as a result of applying only the loose selection criteria B get an output $y < 0.5$. This includes candidate 7b, which is a 'mirage' of event 7a, the binary lens candidate 9, candidates 20 and 27 and the four

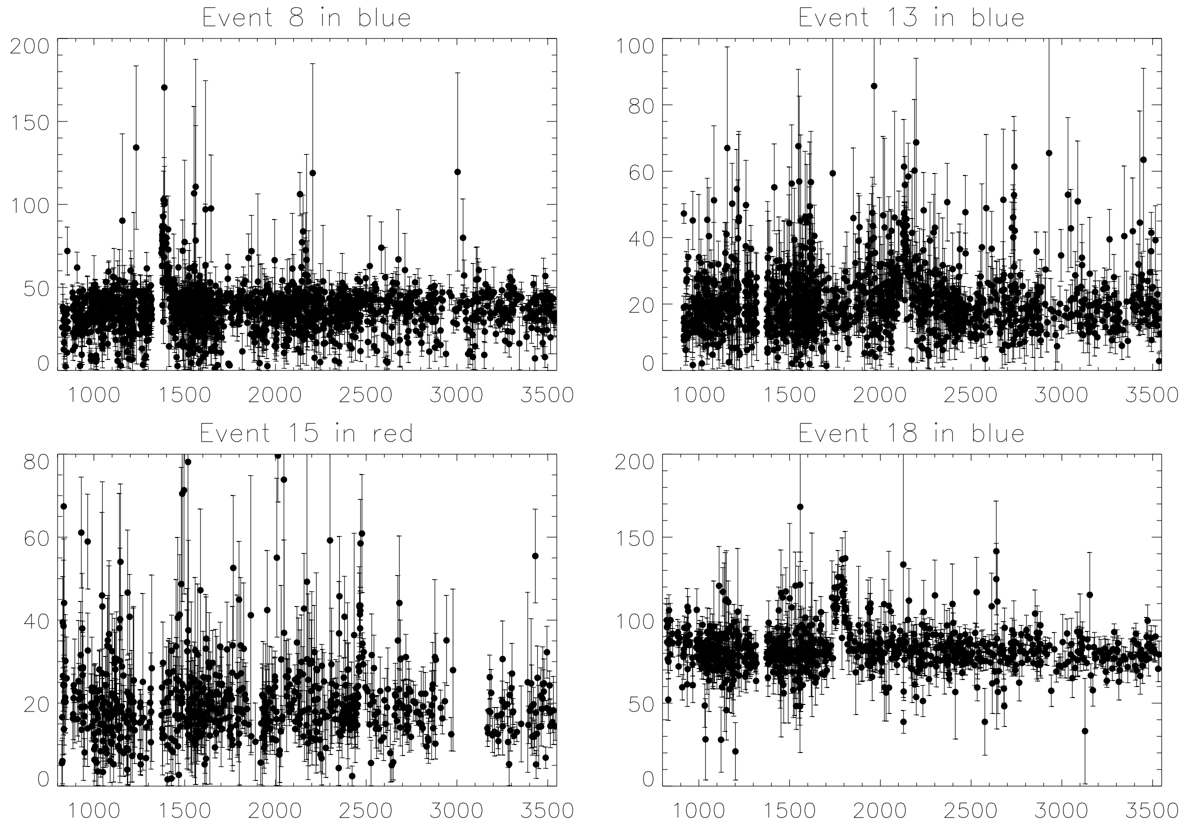


Figure 3.5: This shows the lightcurves for 4 events which received low probability values $y$ in one or both filters. These are all included in set A of Alcock et al. (2000) of convincing microlensing candidates, but are not confirmed by our neural network analysis. The vertical axis is flux in ADU $s^{-1}$ and the horizontal axis is date in JD-2448000.

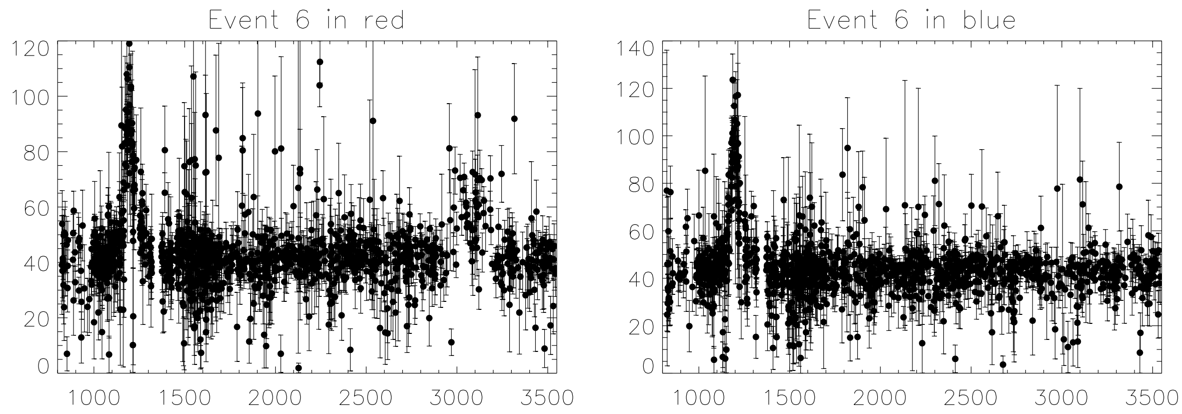


Figure 3.6: This shows the lightcurve for the event 6 which received low probability values $y = 0.76 \pm 0.26$ in the red filter compared to $0.99 \pm 0.01$ in the blue. The vertical axis is flux in ADU $s^{-1}$ and the horizontal axis is date in JD-2448000.

supernova suspects as judged by MACHO: 16, 17, 19, 26. The other two candidates also suspected by MACHO of being supernova lightcurves, 11 and 24, are classified with probability $y_{R,B} > 0.5$. They are, however, discarded after being tested by the second neural network committee.

### 3.4.2 Microlensing versus supernovae

The five lightcurves that have $y' < 0.5$ in the second test are 4 MACHO supernova suspects (11, 12, 17, 19) plus candidate 20. The colour evolution of event 11 is illustrated in Figure 3.4. Although not identified by MACHO as a supernova candidate, event 20 has a typical supernova colour evolution. MACHO claims there are four more supernovae in the dataset, namely events 10, 16, 24 and 26. Unfortunately, candidate 16 has no information in the red filter, but it is classified as non-microlensing in the blue colour by the first network. Although event 24 has probability $y' = 0.6$, the error is large enough to claim its origin is unknown.

Candidates 10 and 26 have outputs greater than 0.8. These two events have timescales of $\sim$ 40 days. If they are indeed supernovae, it means that signal is present only for $\sim$ 20 days after the maximum light. The colour reaches a maximum after $\sim$ 30 days, but even after 20 days B-V can be as much as $0.5 - 1.0$ mag (see Fig. 1 in Phillips et al 1999). Neither event 10 nor 26 shows any significant colour change.

There is just one candidate that has a substantial colour signal identified as blended microlensing by the neural networks. This is event 5. The colours evolve symmetrically during the event, which becomes $\sim$ 1 mag bluer. It has output $y' = 0.74$ and is illustrated in Figure 3.4.

### 3.4.3 Numbers of events

In conclusion, then, the committee of neural networks reckons that there are 9 convincing microlensing candidates. These are the events 1, 4-7, 14, 21, 23 and 25. All these events have an output that always lies above the formal decision boundary $y > 0.5$, even when error bounds are taken into account. Compared to Alcock et al.'s (2000) set A, we have discarded events 8, 13 and 15 (as they fail the first network) and event 18 (which is a marginal case, admittedly). The 4 events that we have excised from Alcock et al.'s sample A are shown in Fig 3.5. In each case, we show the data from the passband which yields the lowest network probability. None of the further events in set B (namely events 9, 20 and 27) are identified as microlensing by the committee, while event 22 is known to be a Seyfert on other grounds.

The neural network can distinguish between supernovae and blended microlensing without the need for multi-parameter fits and deep *Hubble Space Telescope* follow-ups to look for the host galaxy. Alcock et al. reckoned there were 8 supernova suspects. We confirm 4 of these (events 11, 12, 17, 19) and we also found 1 new one (event 20). The remainder of Alcock et al's supernova candidates are not thought to be either convincing supernova or microlensing candidates by the committee.

## 3.5 Optical depth and rate calculations

### 3.5.1 A simple estimate

It is customary to report the results of a gravitational microlensing experiment in terms of optical depth. The conventional formula for optical depth is

$$\tau = \frac{\pi}{4} \frac{1}{N_\star T} \sum_j \frac{t_j}{\epsilon(t_j)} \tag{3.5}$$

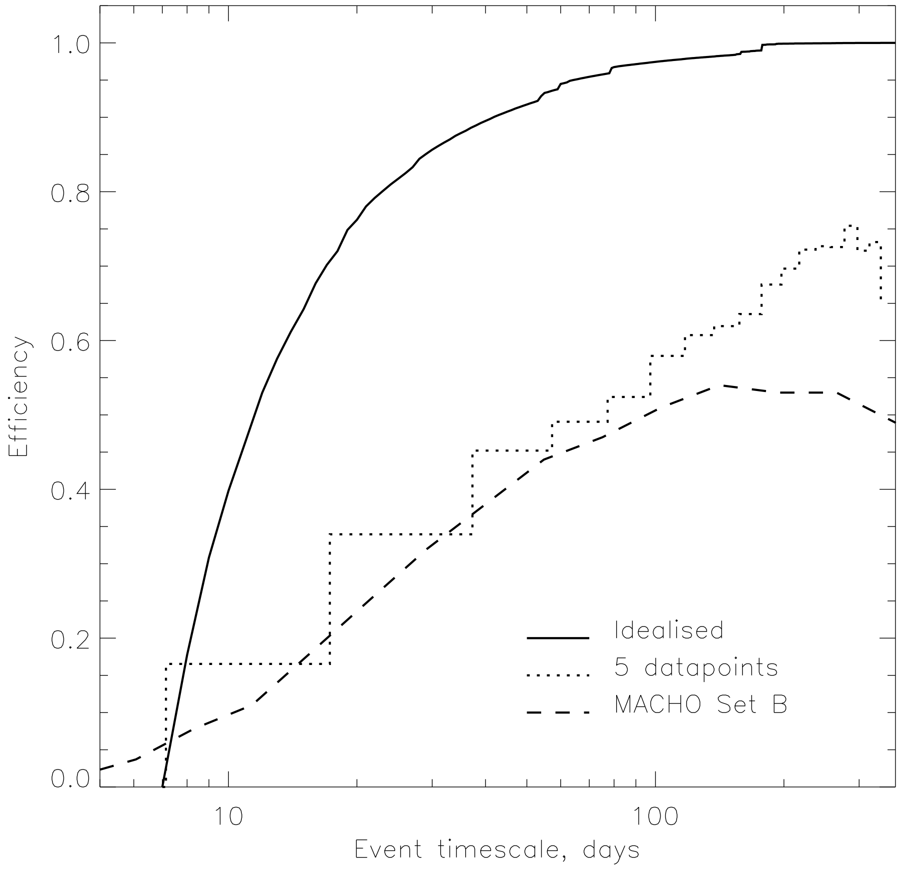


Figure 3.7: This shows three approximations to the efficiency as a function of Einstein diameter crossing timescale $t$. The full curve is the idealised efficiency calculated by integration over the distribution of sampling gaps. The dotted histogram is derived from Monte Carlo simulations of event selection in the training set (at least 5 datapoints with signal-to-noise ratio greater than 5 during the event). The dashed line is the MACHO set B detection efficiency.

where $t_j$ is the Einstein diameter crossing time of the $j$th event, $\epsilon$ is the efficiency, $T$ is the duration of the experiment and $N_\star$ is the number of stars monitored. The summation is taken over the set of microlensing events. There are two major components to the efficiency. The first arises from shortcomings in the cuts used to identify microlensing events. The second arises from the temporal sampling, as events are necessarily missed if they fall in a gap in the data-taking. A neural network, properly trained, will eliminate any contribution from the first component for the subset of events included in the training set. This can be seen from Figure 2.4 of Chapter 2, which shows that the number of misclassified patterns is negligibly small. The second component of the efficiency still remains.

Figure 3.7 shows upper and lower bounds to the efficiency as a function of timescale. An upper bound to the efficiency can be found by summing the distribution of sampling gaps over the 5.7 yr baseline and judging an event to be missed if it falls within a gap. The probability of missing an event with timescale $t$ is just

$$P(t) \propto \sum_{t' \geq t} t' n(t') \tag{3.6}$$

where $n(t)$ is the number of gaps of duration $t$. The quantity $1 - P(t)$ is an idealised efficiency which is shown as a full curve in Fig 3.7. A lower bound to the efficiency is given by the published efficiency results of Alcock et al. (2000) for set B (dashed curve). This is because the neural networks provide a cleaner set of microlensing candidates, uncontaminated by spurious events.

A realisation of the actual efficiency is found from Monte Carlo simulations of the training set, finding the fraction of all events that are included (and hence will be inexorably characterised as microlensing by the network). In the simulations, microlensing events are generated with uniform priors. Only those events with 5 or more datapoints with a signal-to-noise greater than 5 are incorporated into the training set. The efficiency is therefore the ratio of events accepted into the training set to all events. The result is shown as a dashed histogram in Fig 3.7, and lies between the upper and lower bounds.

Applying formula 3.5 to the set of 9 events unambiguously found by the neural network, we obtain lower and upper bounds $3.1 \times 10^{-8} < \tau < 6.1 \times 10^{-8}$ for the optical depth. Here, we have used the timescales corrected for blending given in third column of Table 7 Alcock et al. (2000). The uncorrected timescales are smaller and therefore will give a still lower values.

### 3.5.2 A refined estimate

The knowledge of the optical depth towards the LMC is clearly limited by the size of the dataset and more elaborate calculations are unnecessary. Nonetheless, it is interesting to develop methods of calculating the theoretical microlensing quantities directly from the outputs of neural networks. These can of course be applied to lines of sight for which the dataset is larger.

Let us define $E(x)$ to be the ratio of the within-class probability density of microlensing events in the training set to the true probability density, i.e.,

$$E(x) = \frac{P(x|C_1)}{\hat{P}(x|C_1)} \tag{3.7}$$

Here $\hat{P}(x|C_1)$ is the conditional probability of microlensing (i.e., class 1) in the real world.

The output of the neural network is the posterior probability, and relies on the prior probabilities of different classes of variability in the training set. As follows from Table 3.1, the prior probability of microlensing in the training set is at least $10^6$ times larger than that in the real world. Indeed, the training set contains a large number of microlensing lightcurves to ensure a good variety of training examples. Therefore, the outputs of the trained neural network need to be adjusted with respect to the real-world priors. It has been shown (e.g., Saerens et al. 2002) that a simple iterative procedure can help to tackle the problem. For microlensing, it follows from Bayes' theorem that:

$$\frac{P(C_1|x)P(x)}{P(C_1)} = E(x)\frac{\hat{P}(C_1|x)\hat{P}(x)}{\hat{P}(C_1)} \tag{3.8}$$

We assume that for variable stars, the same equation holds good without the correction for input space sampling, namely

$$\frac{P(C_2|x)P(x)}{P(C_2)} = \frac{\hat{P}(C_2|x)\hat{P}(x)}{\hat{P}(C_2)} \tag{3.9}$$

This assumes that the sampling never causes the misclassification of a variable star as a microlensing event. Let us now recall that the activation $a$ of the output neuron can be interpreted as a logarithm of the ratio of posterior probabilities:

$$a \equiv \log \frac{P(C_1|x)}{P(C_2|x)} \tag{3.10}$$

This is simply the consequence of using the sigmoid function for activation. Combining formula (3.8), (3.9) and (3.10) we easily obtain:

$$\hat{a} = a(x) - \log \frac{E(x)P(C_1)}{\hat{P}(C_1)} + \log \frac{P(C_2)}{\hat{P}(C_2)} \tag{3.11}$$

Typically, $P(C_1)/\hat{P}(C_1) \sim 10^7$. If the activation was originally $\lesssim 7$, then this transformation maps it to below the decision boundary. Only if the output is originally $> 0.999$ does the event remain above the decision boundary.

Thus, having initialized $P(C_k)$ by the frequencies of the classes in the training set, we perform the following iterative steps. Firstly, the formula

$$\hat{P}(C_1) \approx \frac{1}{N} \sum_i y_i \tag{3.12}$$

is used to estimate the true probability of microlensing. Here, $i$ runs through all $N$ patterns in the data set. Then, for each pattern in the data set activation $a_i$ is adjusted using formula (3.11) and the output $y_i$ is re-calculated. The process is repeated until convergence. At the beginning of the iteration, $P(C_1)/\hat{P}(C_1)$ is $O(10^7)$ so that the sampling factor $E(x)$ does not play an important role. However, after a few iterations, it becomes important. $E(x)$ is really a higher dimensional analogue of the temporal efficiency $\epsilon$. It can be calculated by generating events with uniform priors. In every cell of input space, we calculate the ratio of accepted events to generated events.

The output of this procedure is the true probability of microlensing in the experiment monitoring $N_\star$ stars and lasting for a duration $T$. From this, the microlensing rate is

$$\Gamma = \frac{N_\star \hat{P}(C_1)}{T} \tag{3.13}$$

The advantage of this algorithm is that the rate can be computed directly from the dataset, with the intervening steps of lightcurve classification and efficiency estimation.

## 3.6 Conclusions

This chapter has demonstrated the power of machine learning techniques, such as neural networks, for the classification of events in massive variability datasets. Using the specific example of the microlensing surveys, committees of neural networks have been devised to discriminate against common forms of stellar variability and against supernovae. The output of the neural network is the posterior probability of microlensing, given the prior distribution in the training set. The output can be transformed by adjusting the activation to give the posterior probability, given the prior distribution in the real world. Additionally, the error on the probability can be straightforwardly calculated.

The networks have been used to process some of the data taken towards the Large Magellanic Cloud by the MACHO collaboration (Alcock et al. 2000). They provide a set of 13 events whose identification as microlensing is believed to be secure and a further 4 events whose identification is possible. The neural networks confirm the microlensing nature of only 9 of these possible 17 events. In fact, this is a generous estimate as the the 9 events have an output that lies above the formal decision boundary $y > 0.5$, before any correction to the real world priors.

From these 9 events, we compute an upper limit to the optical depth towards the Large Magellanic Cloud of $6.1 \times 10^{-8}$. This is a low value – for example, Alcock et al. (1997) estimate the optical depths of the thin disk, thick disk and spheroid to be $2.2 \times 10^{-8}$, whilst the optical depth of the stellar content of the LMC to be $3.2 \times 10^{-8}$ on average. In other words, our total optical depth matches the contribution from the known stellar populations in the outer Galaxy and the LMC. This implies that there is no contribution needed from compact objects in the halo.

There is supporting evidence for this belief from the exotic events and from the lensing signal towards the Small Magellanic Cloud (SMC). First, the exotic events yield additional information that can break some of the microlensing degeneracies and thus give indirect evidence on the location of the lens. There are two exotic events towards the LMC and two towards the SMC (Bennett et al. 1996; Palanque-Delabrouille 1998; Kerins & Evans 1999; Afonso et al. 2000; Alcock et al. 2001a; Evans 2002). In all cases, the exotic events favour an interpretation in which the lens lies in the Magellanic Clouds. Additionally, Alcock et al. (2001b) imaged one of the events towards the LMC and identified the lens as a nearby low mass disk star.

Second, as Afonso et al. (2003a) point out, the duration of the events towards the SMC is very different from the duration towards the LMC. The EROS collaboration constrain the optical depth towards the SMC to be $< 10^{-7}$ at better than the 90 % confidence level, based on an admittedly small sample. Both these facts militate against the idea that a single population of objects in the Milky Way halo is causing the microlensing events. The mass function, internal kinematics and proper motions of the SMC and LMC are different, so that differences in the distributions of microlensing events are expected if the lenses lie predominantly in the Magellanic Clouds. Based on roughly spherical models of the dark halo, the optical depth towards the SMC is expected to be greater than that towards the LMC if the halo provides most of the lenses. Hence, the paucity of events towards the SMC is beginning to be highly problematic for halo interpretations of the events.

## 3.7 Bibliography

Afonso C. et al. 2000, ApJ, 532, 340

Afonso C. et al. 2003a, AA, 400, 951

Afonso C. et al. 2003b, AA, 404, 145

Alcock C. et al. 1997, ApJ, 479, 119

Alcock C. et al. 2000, ApJ, 542, 281

Alcock C. et al. 2001a, ApJ, 552, 259

Alcock C. et al. 2001a, Nature, 414, 617

Antonello E., Morelli P.L. 1996, AA, 314, 541

Bennett D.P. et al. 1996, Nucl. Physics, 51B, 131

Bishop C., 1995, Neural Networks for Pattern recognition, Oxford University Press, Oxford

Buchalter A., Kamionkowski M., Rich R.M. 1996, ApJ, 469, 676

Di Stefano R., Esin A.A. 1995, ApJ, 448, L1

Dominik M. 1998, AA, 329, 361

Evans N.W., 2002, In "IDM:2002 Fourth International Conference on the Identification of Dark Matter", eds N. Spooner, V. Kudryavtsev, p. 144, World Scientific, Singapore, (astro-ph/0211302)

Kerins E.J., Evans N.W. 1999, ApJ, 517, 734

Lasserre T. et al. 2000, AA, 355, L39

Lira P. et al. 1998, AJ, 115, 234

Mao S. et al. 2002, MNRAS, 329, 349

Mao S., Paczynski B. 1991, ApJ, 374, L37

MacKay D.J.C. 1992, Neural Computation, 4, 720

Nabney I.T. 2002, Netlab: Algorithms for Pattern Recognition, Springer Verlag, New York

Paczynski B. 1986, ApJ, 304, 1

Palanque-Delabrouille N. et al. 1998, AA, 332, 1

Phillips M.M., Lira P., Suntzeff N.B., Schommer R.A., Hamuy M., Maza, J. 1999, AJ, 118, 1766

Press W.H., Teukolsky S., Vetterling W.T., Flannery B. 1992. Numerical Recipes, Cambridge University Press, Cambridge, 2nd ed. chap. 10.

Saerens M., Latinne P., Decaestecker C. 2002, Neural Computation, 14, 21

Welch D.L., Stetson P.B. 1993, AJ, 105, 1813

# Chapter 4

# Microlensing maps for the Milky Way galaxy

This Chapter compares different models of the Milky Way galaxy and investigates their ability to reproduce the recent results from the microlensing surveys. The maps of microlensing optical depth and microlensing event timescale are constructed. The models are introduced in §4.2 which also presents the results of the optical depth calculation. The dynamical model and event timescale distribution are discussed in §4.3.

## 4.1 Introduction

Microlensing surveys of the Galaxy are important because they delineate the mass distribution directly. The total number of events identified by the OGLE and MACHO collaborations towards the Galactic Bulge now exceeds a thousand (e.g., Wozniak et al. 2001; Alcock et al. 2000). The identification of events towards spiral arms has been reported by the EROS and OGLE collaborations (Mao 1999; Derue et al. 2001). Maps of optical depth as a function of Galactic latitude and longitude were first drawn by

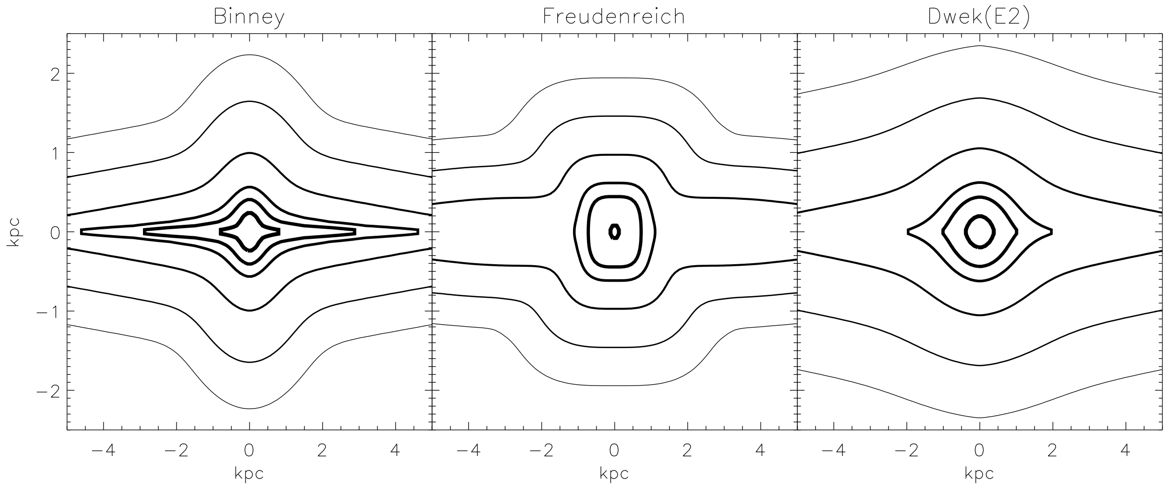


Figure 4.1: Models of the inner Galaxy of Binney et al., Freudenreich and Dwek et al. when viewed along the major axis of the bar. The contour levels are $(10^{-3}, 10^{-2}, 10^{-1}, .5, 1, 2.5) M_\odot$ pc$^{-3}$ and heavier lines correspond to higher density.

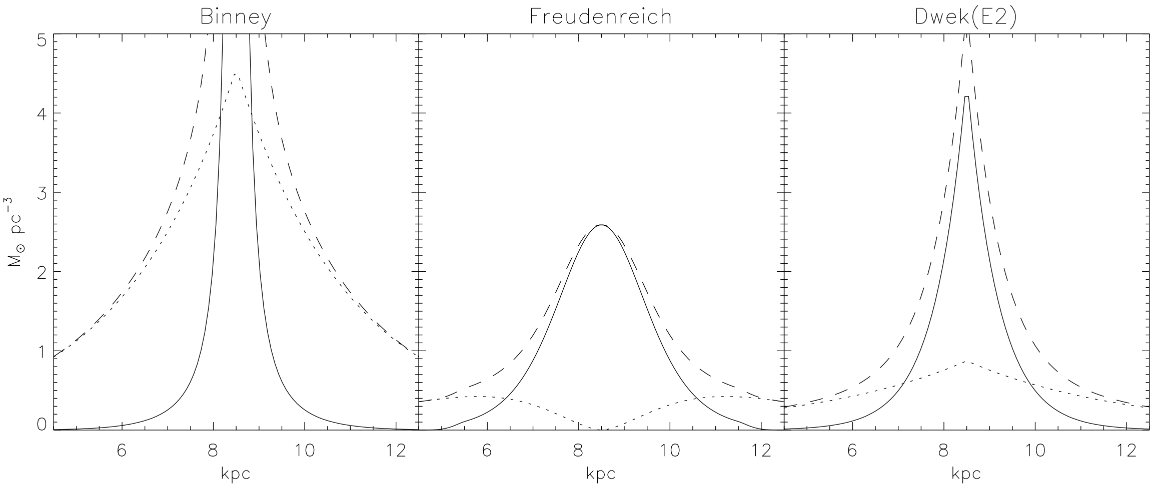


Figure 4.2: Panels show the density contributions of the bar (full line), disk (dotted line) and total (dashed line) along the line of sight to the Galactic Center

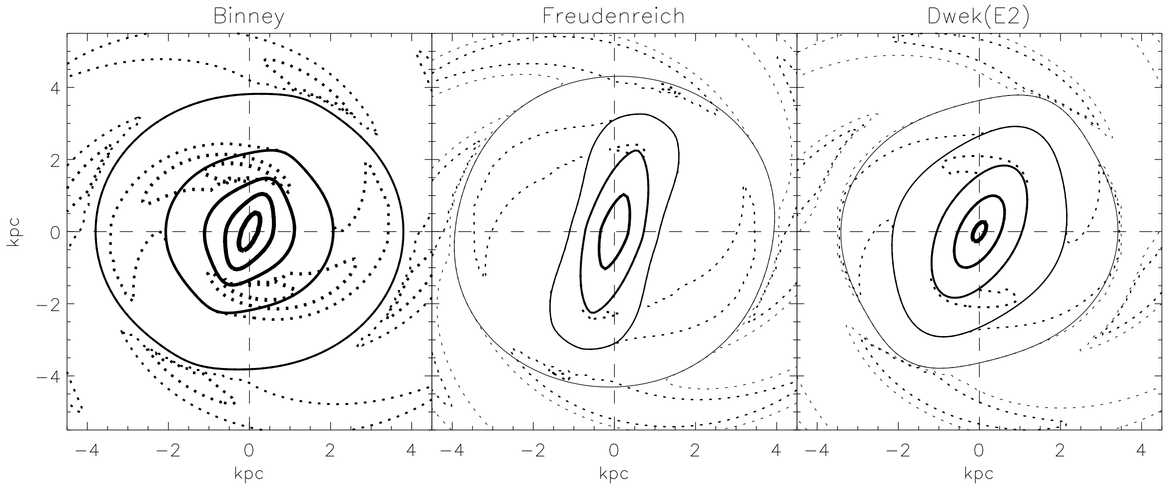


Figure 4.3: Models of the inner Galaxy of Binney et al., Freudenreich and Dwek et al. when viewed from the Galactic Pole. Solid (dotted) lines exclude (include) spirality and Sun-center direction is marked with vertical dashed line (Sun is located at $y = -8.5$ kpc). The contour levels are $(0.33, 0.5, 1, 2, 3, 4, 7) M_\odot$ pc$^{-3}$ and heavier lines correspond to higher density

Evans (1994). Subsequently, a number of authors emphasised the importance of exploiting information on the spatial variation of the optical depth (e.g., Han & Gould 1995; Zhao, Spergel & Rich 1996; Gyuk 1999).

Microlensing searches are being done, or will be done in the near future, in almost any longitude direction. The first of the next generation experiments is the OGLE III venture (see "http://sirius.astrouw.edu.pl/˜ogle/") which uses an 8k×8K MOSAIC camera with a field of view equal to $35' \times 35'$. The future holds still greater promise with the advent of the new class of survey telescopes like the VST ("http://www.eso.org/projects/vst/") and VISTA ("http://www.vista.ac.uk"). VISTA has a field of view of 2.25 square degrees in the optical, while the VST has a smaller, but still substantial, field of view of 1 square degree. So, there is a need for large-scale maps of both the microlensing optical depth and the mean timescale for the Galaxy. These maps can be used to pick target fields, to plan search methodologies for future experiments and to assess what can be learnt about the structure of the Milky Way from the distribution of microlensing events.

| Model | bar < 2.5 kpc | disk < 2.5 kpc | bar+disk < 2.5 kpc | disk < 8.5 kpc | inner spiral 3.5 kpc | outer spiral 8.5 kpc |
|---|---|---|---|---|---|---|
| Binney et al | 0.5 | 1.0 | 1.5 | 3.2 | 0.3 | 0.9 |
| Freudenreich | 1.1 | 0.4 | 1.5 | 3.1 | 0.2 | 1.2 |
| Dwek et al | 0.8 | 0.7 | 1.5 | 3.0 | 0.2 | 1.0 |

Table 4.1: This table shows the mass (in units of $10^{10} M_{\odot}$) in different components of the Galaxy in the three models. The fifth column is the additional mass within 3.5 kpc caused by the inner spiral alone. The sixth column is the additional mass within 8.5 kpc caused by the outer spiral alone.

## 4.2 Optical depth maps

We study three models of the inner Galaxy. The starting point of all three models is the same, namely the infrared surface brightness maps seen by the DIRBE instrument on the COBE satellite. The first is the model of Binney, Gerhard & Spergel (1997), which is partially revised in Bissantz et al. (1997). Here, the observed luminosity at $\sim 240$ microns, which is dominated by thermal emission from dust, is used to deduce the three-dimensional spatial distribution of the dust. This gives a short, flattened, cuspy bar with axis ratio 1 : 0.3 : 0.3 and with a viewing angle $\phi_0 = 20°$. The second is the model of Freudenreich (1998). Here, a mask of areas believed to be contaminated with dust is constructed from maps of color variations. The mask is used to excise portions of the DIRBE data and the remainder of the data is fitted. Note that the mask removes almost all of the data within $|b| \lesssim 5°$ for longitudes within 90° of the Galactic Center (see Figure 1 of Freudenreich's paper). This gives an extended, diffuse, swollen bar with axis ratio 1 : 0.37 : 0.27 and with a viewing angle $\phi_0 = 14°$. The disk has a central hole with a radius of $\sim 3$ kpc. The third is the E2 model of Dwek et al. (1995), as partially revised by Stanek et al. (1997). The density contours are stratified on concentric ellipses with axis ratio 1 : 0.42 : 0.28 with a viewing angle $\phi_0 = 24°$. In correcting for dust, Dwek et al. assumed a uniform foreground screen. The bar is less massive and less elongated than Freudenreich's and the disk does not have a central hole. To ensure a fair comparison, all

| source<br>lens | bar<br>bar | bar<br>disk | bar<br>bar+disk |
|---|---|---|---|
| Binney et al | 0.28 | 0.60 (0.88) | 0.88 (1.16) |
| Freudenreich | 0.93 | 0.92 (1.38) | 1.85 (2.31) |
| Dwek et al | 0.48 | 0.73 (1.03) | 1.21 (1.51) |

Table 4.2: Optical depth to the red clump giants towards $\ell = 3^\circ.9$, $b = -3^\circ.8$ in units of $10^{-6}$. Recall that Popowski et al.'s (2000) value for the optical depth to the red clump is $2.0 \pm 0.4 \times 10^{-6}$, which should be compared to the numbers in the last column. The figures in parentheses include the effects of spiral structure (the extra enhancement in the optical depth comes mainly from the extra mass in the spiral models).

| source<br>lens | bar<br>bar | bar<br>disk | disk<br>bar | disk<br>disk | bar+disk<br>bar+disk |
|---|---|---|---|---|---|
| Binney et al | 0.13 | 0.31 (0.37) | 0.13 (0.13) | 0.26 (0.37) | 0.83 (0.98) |
| Freudenreich | 0.66 | 0.70 (0.92) | 0.13 (0.15) | 0.13 (0.22) | 1.62 (1.87) |
| Dwek et al | 0.25 | 0.40 (0.49) | 0.25 (0.27) | 0.30 (0.43) | 1.21 (1.42) |

Table 4.3: Optical depth to the main sequence stars towards $\ell = 2^\circ.68$, $b = -3^\circ.35$ in units of $10^{-6}$. The total microlensing optical depth reported by Alcock et al. (2000) is $2.43 \pm 0.39 \times 10^{-6}$, which can be compared to the numbers in the last column. The figures in parentheses include the effects of spiral structure.

three models are normalized to have the same total mass of $1.5 \times 10^{10} M_\odot$ within 2.5 kpc. Optical depths scale in rough proportion with total mass, and so our results can be easily converted to other preferred values. The three models are illustrated in Figures 4.1, 4.2 and 4.3. Figures 4.1 and 4.3 show cuts through the principal planes of the bar, while Figure 4.2 shows density contributions of different Galactic components along the line of sight to the Galactic Center. Table 4.1 shows the masses of the components in the three models. Freudenreich's bar is the most massive, Binney et al.'s the least massive.

EROS and OGLE are looking towards spiral arms. Accordingly, we include the effects of spiral arms in our calculations. We assume that the inner spiral pattern is two-armed and given by multiplying the density by eqn (2) of Binney et al. (1997), namely

$$1 + \epsilon \cos^6(\phi - 0.95(r - r_{\min}) - \phi_0), \qquad \epsilon = \tanh(r - r_{\min}). \tag{4.1}$$

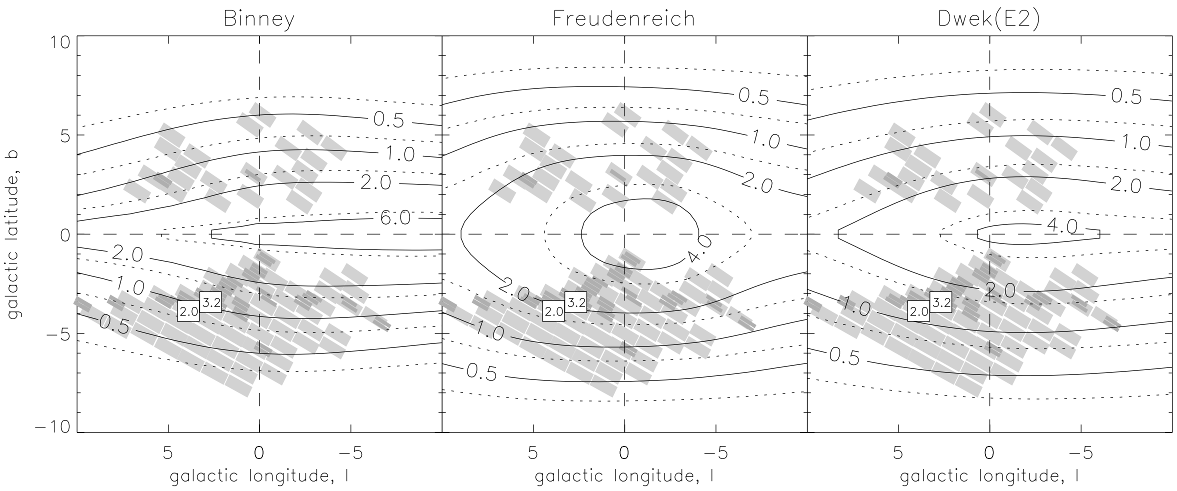


Figure 4.4: Contours of microlensing optical depth to the red clump giants (in units of $10^{-6}$) in the three bar models, excluding (full lines) and including (dotted lines) spirality. The optical depths reported by Alcock et al. (2000) and Popowski et al. (2000) are shown in boxes. Light (dark) gray boxes correspond to EROS (OGLE II) fields.

Here, $r_{\rm min}$ is proportional to the length of the bar and is 1.5 kpc for Binney et al.'s bar, 2.25 kpc for Freudenreich's and 1.7 kpc for Dwek et al.'s. This density factor is applied between $r_{\rm min}$ and $r_{\rm max} = 3.5$ kpc. The outer spiral pattern is four-armed and given by $1+2\epsilon\cos^6(2\phi-1.1(r-r_{\rm min})-15°)$ between $r_{\rm min} = 4.1$ kpc and $r_{\rm max} = 8.5$ kpc. The phase and the wavenumber of the inner and outer spirals are chosen to match the longitudes of the principal spiral arms given by Englmaier (2000). The arm/interarm contrast is 2 for the inner and 3 for the outer spiral (cf. Rix & Rieke 1993). This is reasonable for a young population, but an overestimate for old low mass stars that may make up the bulk of the lensing population. Our results on the effects of spirality are upper limits. Figure 4.3 illustrates the effects of spirality (dotted lines) on the density distribution for all three models. Microlensing maps show contours of the source-averaged microlensing optical depth $\langle\tau\rangle$ computed via (Kiraga & Paczyński 1994)

$$\langle\tau\rangle = \frac{\int_0^\infty \rho(D_{\rm s})\tau(D_{\rm s})D_{\rm s}^{2+2\beta}dD_{\rm s}}{\int_0^\infty \rho(D_{\rm s})D_{\rm s}^{2+2\beta}dD_{\rm s}}, \tag{4.2}$$

where $D_{\rm s}$ is the source distance and $\rho$ is the density of deflectors. For red clump stars,

| Direction | $\theta$ Mus | $\gamma$ Nor | $\gamma$ Sct | $\beta$ Sct |
|---|---|---|---|---|
| EROS | $< 0.68$ | $0.27^{+0.30}_{-0.17}$ | $1.64^{+0.92}_{-0.74}$ | $< 1.03$ |
| Binney et al | 0.34 (0.44) | 0.56 (0.93) | 0.80 (1.11) | 0.65 (0.85) |
| Freudenreich | 0.44 (0.50) | 0.86 (1.45) | 1.13 (1.49) | 1.00 (1.30) |
| Dwek et al | 0.39 (0.52) | 0.63 (1.00) | 0.94 (1.28) | 0.75 (1.00) |

Table 4.4: Optical depth towards spiral arms in units of $10^{-6}$. The figures in parentheses include the effects of spiral structure. The numbers should be compared with the experimental data provided by the EROS collaboration (Derue et al. 2001) in the second line.

$\beta \approx 0$; for main sequence stars, $\beta \approx -1$. Red clumps stars are bright and distinctive residents of the bar (e.g., Paczyński & Stanek 1998). In other words the estimates of the optical depth to these standard candles are free from systematic uncertainties such as blending and contamination by disk stars. Figure 4.4 shows contours of optical depth to the red clump in the three models. The dotted contours show the effect of including the spiral structure. The amplification caused by spirality varies according to the line of sight but it is typically $\sim 20\%$. Of the three, Binney et al.'s gives the least symmetric microlensing map, especially close to the Galactic plane where the gradients are very steep. Freudenreich's is the most symmetric, as it possesses the smallest viewing angle. The boxes mark the two locations where the optical depth of bar stars has been measured. The first is $\ell = 3.9°, b = -3.8°$ where Popowski et al. (2000) report $2.0 \pm 0.4 \times 10^{-6}$ for the optical depth to the red clump stars. The second is $\ell = 2.68°, b = -3.35°$ where Alcock et al. (2000) report $3.2 \pm 0.5 \times 10^{-6}$ for the optical depth to bar stars. The value of the optical depth at $\ell = 3.9°, b = -3.8°$ contributed by each component in the three models is recorded in Table 4.2. Freudenreich's model is in good agreement with the two measurements of optical depth to the bar sources. The value of the optical depth to the main sequence stars at the location $\ell = 2°.68$, $b = -3°.35$ is given in Table 4.3. This can be compared to the total microlensing optical depth of $2.43 \pm 0.39 \times 10^{-6}$ reported by Alcock et al. (2000). Even though all three models have the same total mass within 2.5 kpc, Freudenreich's model has the higher optical depth because the bar is more extended.

Notice that the shape of the contours in Figure 4.4 becomes very similar for all three models once $|b| > 4°$. This makes it challenging to characterize the bar morphology on the basis of data from the observed fields. One qualm is that Freudenreich excised most of the DIRBE data within $|b| \lesssim 5°$ of the Galactic plane. In this region, his model is entirely extrapolated from the light distribution at higher latitudes and so may be unreliable. Binney et al.'s model reproduces the strong concentration in the light near the Galactic plane. It lies within $\approx 2\sigma$ of Popowski et al.'s measurement when spiral structure is included. Dwek et al.'s model with spiral structure is just outside $1\sigma$. Can we modify Binney et al.'s model to reproduce the microlensing optical depth data? To get agreement with the data, the bar needs to be made both longer and fatter. For example, changing the axis ratio to 1 : 0.6 : 0.4 (as originally envisaged in Binney et al. 1997) and increasing the total mass within 2.5 kpc by 50% gives a model in reasonably good agreement (namely $\tau = 1.5 \times 10^{-6}$ at $\ell = 3.9°, b = -3.8°$ excluding spiral structure; this rises to $1.8 \times 10^{-6}$ when spiral structure is included). Figure 4.5 shows the contours of optical depth to all sources in the inner Galaxy using Freudenreich's bar. The Galactic disk has a sech-squared vertical profile with scaleheight 167 pc and an exponential horizontal profile with scalelength 2.5 kpc. The insets show the details of three areas towards the Scutum, Norma and Musca spiral arms that are being monitored by the EROS group. We see that there is a factor of $\sim 6$ variation in the optical depth across the EROS fields towards all three spiral arms. Freudenreich's bar is so distended that it causes a thickening of the optical depth contours even at longitudes well away from the center. We can exploit the maps to estimate the number of ongoing microlensing events of stars brighter than 20th magnitude in the Milky Way. At any instant, there are $\sim 500$ microlensing events, where we have allowed for extinction in the same manner as in Chapter 5 and Chapter 6. Table 4.4 compares the predictions of the three models with the data provided by EROS. Notice that all three models are in a reasonable agreement with the EROS measurements (although Freudenreich's model

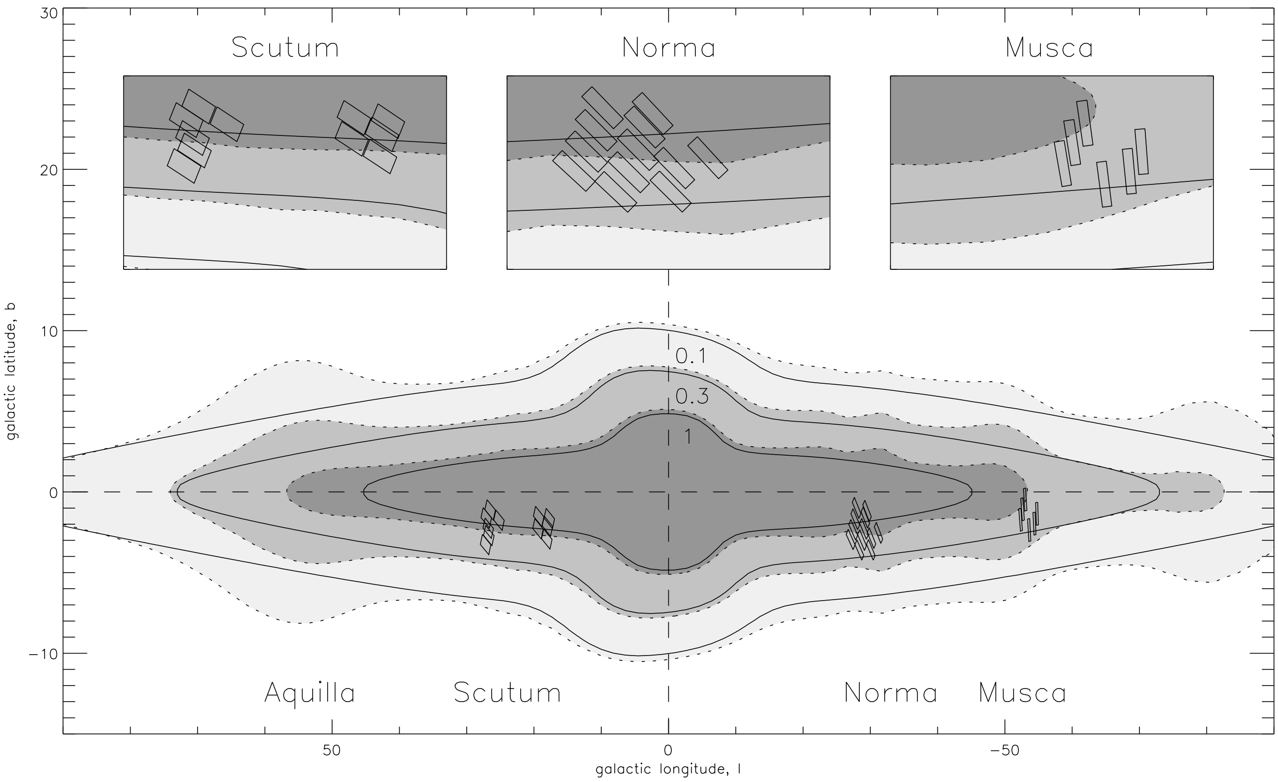


Figure 4.5: Contours of microlensing optical depth to all sources (in units of $10^{-6}$) in Freudenreich's model, excluding (full lines) and including (dotted lines) spiral structure. The insets show the details of EROS fields towards the Scutum, Norma and Musca spiral arms.

performs somewhat better) except for the field $\gamma$ Norma. This field – located at $\sim 30^\circ$ from the Galactic centre – is believed to provide a measure of disk lensing in the Galaxy. All three models give a value of optical depth about $1-2\sigma$ above the data which indicates that the bar contribution is probably over-estimated.

## 4.3 Timescale map

It is also interesting to build maps of the mean Einstein crossing timescale. We assume that the mass function of the bar (or disk) is a power-law between $0.01M_\odot$ and $0.5M_\odot$ with index $-1.33$ (or $-0.54$) as suggested by Zoccali et al. (2001). Let $(x, y, z)$ define coordinates along the major, intermediate and minor axis of the bar. We calculate the average velocity dispersions required to reproduce the shape of Freudenreich's bar guided by the tensor virial theorem (e.g., Han & Gould 1995, Blum 1996), however the pattern speed of the bar is not taken into account. The velocity distribution is Gaussian with dispersions $\sigma_x = 100\,\mathrm{km\,s^{-1}}$, $\sigma_y = 80\,\mathrm{km\,s^{-1}}$, $\sigma_z = 68\,\mathrm{km\,s^{-1}}$. For the disk lenses, the random component has $\sigma_R = 34\,\mathrm{km\,s^{-1}}$, $\sigma_\phi = 21\,\mathrm{km\,s^{-1}}$, $\sigma_z = 18\,\mathrm{km\,s^{-1}}$ about a mean velocity $\langle v_\phi \rangle$ of $214\,\mathrm{km\,s^{-1}}$ (see Chapter6). The velocity of the Sun has the following components: $v_{\odot R} = -10\,\mathrm{km\,s^{-1}}$ $v_{\odot\phi} = 219.25\,\mathrm{km\,s^{-1}}$ and $v_{\odot z} = 7.17\,\mathrm{km\,s^{-1}}$ (Dehnen & Binney 1998). Although small velocity perturbations will be associated with the spiral arms, these are neglected in our calculations. Figure 4.6 shows contours of the source-averaged timescale for events with sources and lenses in either the disk or Freudenreich's bar, including (dotted lines) and excluding (full lines) the spiral structure. The timescale is shortest towards the Galactic Center and becomes longer at increasing Galactic longitudes. This is easy to understand because the motion of the lens is directed more and more along the line of sight at larger longitudes and so the transverse velocity is typically smaller. Notice that spiral structure has a dramatic effect on the timescale. For example, at Baade's Window, the timescale is increased by a factor of $\sim 50\%$ on

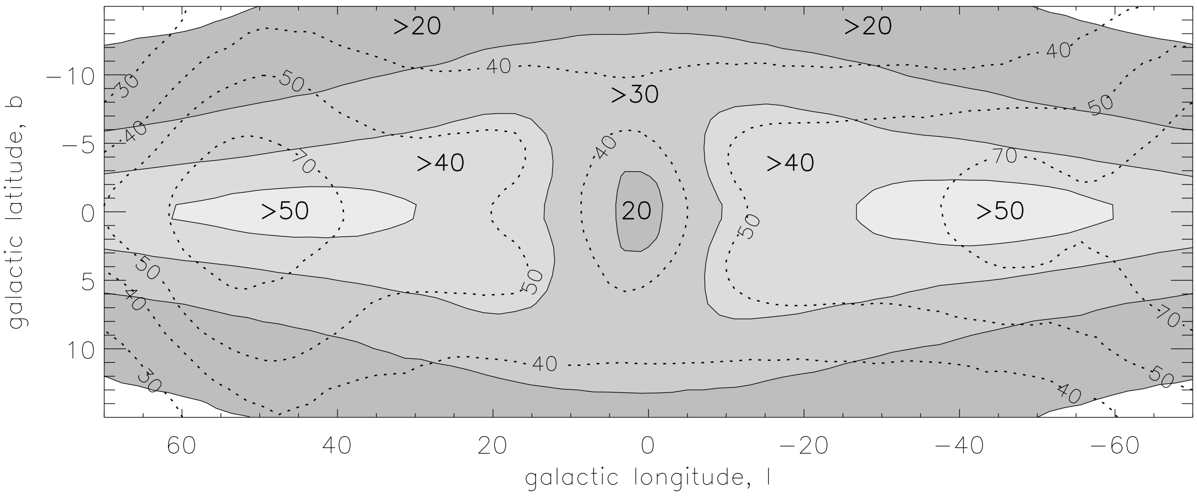


Figure 4.6: Contours of source-averaged timescale (in days) for microlensing events with sources and lenses lying in either the disk or Freudenreich's bar. The timescale is the time taken to cross the Einstein radius. The full lines exclude the contribution of spiral structure, the dotted lines include the contribution. The contour levels are at $20, 30, 40, 50, 60$ and $70$ days .

incorporating the effects of spirality. At the locations around $|l| \sim 60^\circ$ the timescale is doubled by the effect of spirality.

## 4.4 Conclusions

We have drawn large scale maps of the optical depth and timescale distribution for microlensing in the Galaxy. Freudenreich's bar does give a reasonable representation of the microlensing data to the Bulge. It recovers the optical depth towards the spiral arms (with the exception of $\gamma$ Norma). However, Freudenreich's model is hollow. Stars otherwise expected to be in the central parts of the disk can instead be used to augment the bar where they are efficient at microlensing.

As pointed out by Gould (1995), microlensing surveys in the K band would be very valuable to distinguish between models. This is all the more true given the capabilities of the new generation of survey telescopes. VISTA has a field of view of 0.5 square degrees in the K band. Assuming that the seeing is $0.8''$ in Chile and scaling the results of Gould (1995), then we estimate that VISTA will monitor $\sim 1.5 \times 10^6$ stars in a single field of view for crowding-limited K band images towards the Bulge. This means that we are probing the luminosity function down to $K \sim 16$, assuming 3 magnitudes of extinction. Photometry accurate to 3% for a $K \sim 16$ star will take $\sim 1$ minute on VISTA. Hence, a K band survey of a $5° \times 5°$ field close to the Galactic Center will take $\sim 100$ minutes every night, allowing 50 minutes for readout, slew and guide star acquisition time. So, a K band microlensing survey of the inner Galaxy is an attractive and feasible proposition with VISTA.

## 4.5 Bibliography

Alcock C. et al. 2000, ApJ, 541, 734

Binney J., Gerhard O., Spergel D. 1997, MNRAS, 288, 365

Bissantz N., Englmaier P., Binney J., Gerhard O.E. 1997, MNRAS, 289, 651

Blum R. 1995, ApJ, 444, L89

Derue F. et al. 2001, AA, 373, 126

Dwek E. et al. 1995, ApJ, 445, 716

Edvardsson B., Andersen J., Gustafsson B., Lambert D.L., Nissen P.E., Tomkin J. 1993, A&AS, 102, 603

Englmaier P., 2000, Rev Modern Astronomy, 13, 97

Evans N.W., 1994, ApJ, 437, L31

Gould A. 1995, ApJ, 446, L71

Gyuk G. 1999, ApJ, 510, 205

Han C., Gould A. 1995, ApJ, 449, 521

Kiraga M., Paczyński B. 1994, ApJ, 430, L101

Mao S. 1999, AA, 350, L19

Paczyński B., Stanek K.Z. 1998, ApJ, 494, L219

Popowski P. et al. 2000, In Menzies J.W., Sackett P.D. eds, Proc. Microlensing 2000, ASP Conference Series, in press (astro-ph/0005466)

Rix H.W., Rieke M.J. 1993, ApJ, 418, 123

Stanek K.Z., Udalski A., Szymanski M., Kaluzny J., Kubiak M., Mateo M., Krzeminski W. 1997, ApJ, 477, 163

Wozniak P.R., Udalski A., Szymanski M., Kubiak M., Pietrzynski G., Soszynski I., Zebrun K. 2001, Acta Astronomica, 51, 175

Zhao H.S., Rich R.M., Spergel D.N. 1996, MNRAS, 282, 175

Zoccali M., Cassisi S., Frogel J.A., Gould A., Ortolani S., Renzini A., Rich R.M., Stephens A.W. 2000, ApJ, 530, 418

# Chapter 5

# Supernovae with the Gaia satellite

In this Chapter we analyze the capabilities of the Gaia satellite (introduced in §1.3) for supernovae (SNe) detection. The Monte-Carlo simulations of SNe observations with Gaia are described in §5.2. In §5.3 we calculate how many SNe are detectable as a function of the phase of the lightcurve and discuss possible identification strategies. The scientific returns from Gaia's SNe sample are summarized in §5.4.

## 5.1 Introduction

A brief review of the supernovae research was given in Chapter 1. The observational characteristics of SNe and the classification of SNe types can be found in §1.5. Let us recall that SNe are divided into type I and II primarily on the basis of their spectra, with lightcurve shape as a secondary diagnostic. Perhaps only as many as $\sim 300$ SNe have reasonably detailed lightcurves (e.g., Leibundgut et al. 1991, Hamuy et al. 1996, Leibundgut 2000). Even with the limited dataset available, there is a considerable spread in the intrinsic properties and uncertainty as to the rate, type and location of SNe as a function of host galaxy. At the moment, there is some, al-

| | E-S0 | S0/a, Sa | Sab, Sb | Sbc-Sd | Sdm-Im |
|---|---|---|---|---|---|
| Type Ia | 0.42 | 0.21 | 0.21 | 0.21 | 0.21 |
| Type Ib/c | - | 0.01 | 0.11 | 0.33 | 0.38 |
| Type II | - | 0.07 | 0.57 | 1.66 | 1.78 |

Table 5.1: SNe explosion rates (in units of SNe per $10^{10}L_\odot$ per century) according to Hubble type, adapted from the van den Bergh & Tammann (1991) values using a Hubble constant of 65 $\mathrm{kms^{-1}Mpc^{-1}}$. The galaxy types follow the classification scheme of de Vaucouleurs (1959; see also van den Bergh 1998).

beit limited, information on $\sim$ 2000 SNe available in the standard catalogues (see Tsvetkov et al. 1998 or "http://www.sai.msu.su/sn/sncat/" and Barbon et al. 1999 or "http://web.pd.astro.it/supern/").

Gaia is an ideal tool to study nearby SNe (within a few hundred Mpc). Gaia will provide a huge dataset of high quality local SNe Ia in which any deviations from "standard candles" can be analysed. As the dataset is so large, there will be good numbers of rarer phenomena, such as subluminous SNe and SNe Ib/c. Some authors (Høg, Fabricius & Makarov 1999; Tammann & Reindl 2002) have already provided rough estimates of the numbers of SNe Ia that Gaia will discover. Here, we carry out detailed simulations using a Galactic extinction model and the satellite scanning law to compute the numbers of SNe detected as a function of the phase of the lightcurve. We show that Gaia will record data on at least 21 400 SNe during the five-year mission lifetime. This breaks down into $\sim$ 14 300 SNe 1a, $\sim$ 1400 SNe Ib/c and $\sim$ 5700 SNe II. These SNe span a redshift range up to $z \sim 0.14$. Gaia will probably alert on all SNe detected before maximum. These numbers are $\sim$ 6300 SNe Ia, $\sim$ 500 SNe Ib/c and $\sim$ 1700 SNe II during the whole mission. In other words, Gaia will issue $\sim$ 1700 SNe alerts a year or $\sim$ 5 alerts a day. Roughly 75% of all alerts will be SNe Ia, the remainder will be SNe Ib/c and II. All these numbers are lower limits and may be increased by a factor of $\sim$ 2 depending on the SNe contribution from low-luminosity galaxies.

| | E-S0 | S0/a, Sa | Sab, Sb | Sbc-Sd | Sdm-Im |
|---|---|---|---|---|---|
| N (galaxies) | 1200 (4850) | 679 (3024) | 867 (3694) | 1993 (6957) | 1798 (3701) |
| Type Ia | 29 (80) | 7 (11) | 11 (31) | 19 (52) | 16 (16) |
| Type Ib/c | 0 (0) | 1 (1) | 6 (16) | 30 (80) | 29 (29) |
| Type II | 0 (0) | 2 (4) | 31 (85) | 152 (412) | 135 (135) |

Table 5.2: Number of galaxies of each Hubble type within 75 Mpc in the CfA catalogue. Also shown is the number of SNe within 75 Mpc during the 5 year mission lifetime. For comparison, the figures in parentheses are based on an extrapolation of the galaxy LF that is flat down to an absolute magnitude of $-14$.

## 5.2 Monte Carlo simulations

Gaia's G band is very close to the conventional V band for a wide colour range (ESA 2000). Richardson et al. (2002) use the Asiago Supernova Catalogue to study the V band absolute magnitude distributions according to type. They find that the mean absolute magnitude of SNe Ia at maximum is $-18.99$. This figure includes the contribution from the internal absorption of the host galaxy, as well as a correction to our preferred value of the Hubble constant of 65kms$^{-1}$Mpc$^{-1}$, which we use henceforth. As Gaia's limiting magnitude is $G \sim 20$, this means that the most distant SNe Ia accessible to Gaia are $\sim$ 630 Mpc away. Similarly, the mean absolute magnitude of SNe Ib/c at maximum is $-17.75$, so that the most distant SNe Ib/c detectable by Gaia are $\sim$ 355 Mpc away. SNe II are subdivided further according to lightcurve into linear (L) and plateau (P) types. The mean absolute magnitude of II-L type is $-17.63$ and of II-P type is $-16.44$ (Richardson et al. 2002). These correspond to distances of $\sim$ 335 Mpc and $\sim$ 195 Mpc respectively. Such distances emphasise that Gaia is the ideal tool to discover relatively nearby SNe, but will not make any contribution to the searches for high redshift SNe.

The rates with which SNe occur in different galaxies at low redshift are given in Table 5.1, inferred from van den Bergh & Tammann (1991). This gives the number of SNe per century per $10^{10}L_{\odot}$. Although the data come with substantial uncertainties, there are three recent studies that provide some supporting evidence. First, the EROS

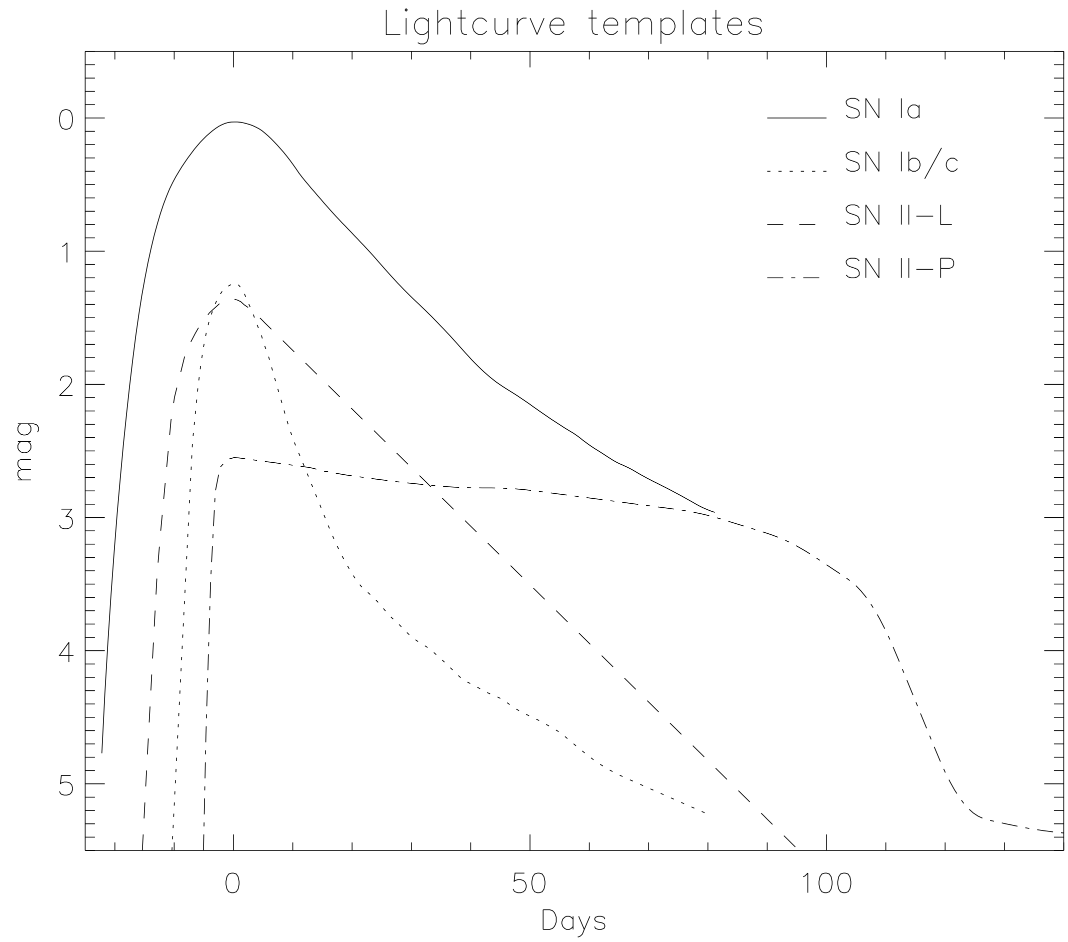


Figure 5.1: This shows the templates adopted for SNe Ia, Ib/c, II-L and II-P in the Monte Carlo simulations. The templates come from data on SN 1991T by Lira et al. (1998), on SN 1994I by Richmond et al. (1996), on SN 1990K by Cappellaro et al. (1995) and SN 1999em by Hamuy et al. (2001). The graphs show relative magnitude versus time in days.

collaboration (Hardin et al. 2000) found a SNe Ia rate of $\sim 0.18$ per century per $10^{10}\mathrm{L}_\odot$ for redshifts $z$ in the range 0.02 to 0.2. Second, Pain et al. (1996) found a SNe Ia rate of $\sim 0.36$ per century per $10^{10}\mathrm{L}_\odot$ at the somewhat higher redshift of $z \sim 0.4$. Third, the rates in Cappellaro et al. (1997) are of the same order as van den Bergh & Tammann (1991), although typically lower by a factor of two. The host galaxies follow the local large-scale structure. We use the latest version of the CfA redshift catalogue[1](Huchra et al. 1992). This contains the sky positions and heliocentric velocities of $\sim 20\,000$

[1]http://cfa-www.harvard.edu/~huchra/zcat/

galaxies. On plotting numbers of galaxies versus distance, the graph peaks at $\sim 75$ Mpc and thence shows a steady decline. This suggests that the catalogue can be used out to at most $\sim 75$ Mpc. The number of galaxies of each Hubble type in the CfA catalogue within 75 Mpc is listed in Table 5.2. These numbers must be regarded as lower limits to the true numbers within 75 Mpc, as the luminosity functions (LFs) derived from the CfA catalogue are incomplete at faint magnitudes. To take this into account, we assume that after reaching maximum, the galaxy LF remains flat down to an absolute magnitude of $-14$. Given in parentheses in Table 5.2 are the number of galaxies and SNe within 75 Mpc assuming such a flat LF. These numbers can be regarded as upper limits. Beyond 75 Mpc, we assume that the distribution of galaxies is homogeneous and that the number scales like $D^3$ where $D$ is the heliocentric distance. Given the numbers of galaxies and the observed rates, we can then straightforwardly compute the total number of SNe that explode during the five-year Gaia mission lifetime and are brighter than the limiting magnitude. In all, there are at least $\sim 48\,000$ SNe Ia and $\sim 7000$ SNe Ib/c. The numbers for SNe II depend on the relative frequency of II-L with respect to II-P, which is not very well-known. Henceforth, we denote the fraction of all SNe II that are L-type by $f_{\mathrm{II}}$. Then, the numbers of SNe II that explode are $\sim 28\,500 f_{\mathrm{II}} + 5600(1 - f_{\mathrm{II}})$. These numbers are lower limits for two reasons – first because no contribution from faint galaxies is included and second because Gaia's limiting magnitude may be deeper than 20th in practice. Allowing for faint galaxies with the flat LF gives results a factor $\sim 2$ times larger. To assess the efficiency of SN detection, we perform Monte Carlo simulations (e.g., Li, Filippenko & Riess 2001). First, the distance to the host galaxy is picked from the $D^3$ distribution. If $D < 75$ Mpc, then the galaxy is chosen from the CfA catalogue. If $D > 75$ Mpc, then the galaxy positions are distributed uniformly over the sky. Next, we choose the SN absolute magnitudes from Gaussian distributions with means and dispersions given in Table 5.3. These numbers already includes the effects of absorption in the host galaxy. The contribution to dimming of the SN from Galactic

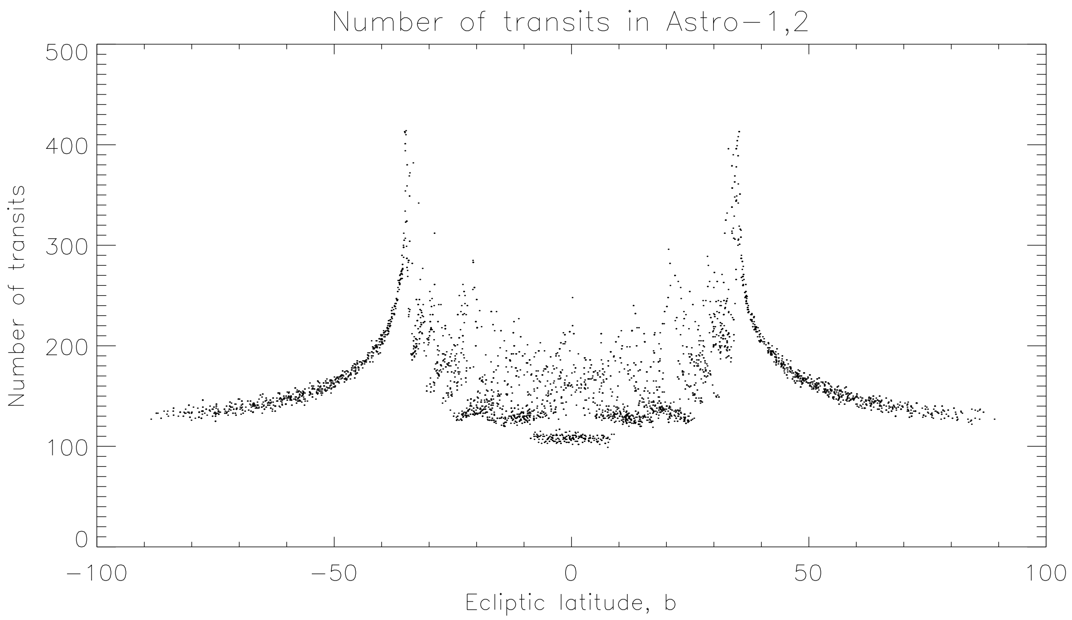


Figure 5.2: This shows the number of transits made by the ASTRO-1 and ASTRO-2 telescopes as a function of ecliptic latitude. The figure is drawn by choosing 5000 random directions on the sky, and computing the ecliptic latitude and number of transits using software supplied by L. Lindegren. The transits are strongly clustered into groups of between two and five.

absorption is calculated using software kindly supplied by R. Drimmel, which is based on the extinction model of Drimmel & Spergel (2001).

The lightcurve can now be generated using the templates illustrated in Figure 5.1. For SNe Ia, we use the data of Lira et al. (1998) on SN 1991T as a standard template. This is an unusually bright SN Ia with a peculiar spectrum (Saha et al. 2001). However, our algorithm chooses the magnitude at maximum from a Gaussian distribution and so only the shape of the template is important. Therefore, although SN 1991T is overluminous, this does not cause exaggeration of our results. We reconstruct the rising part of the lightcurve of SNe Ia using the fact that luminosity is proportional to the square of the time since explosion (e.g., Riess et al. 1999). For SNe Ib/c, we use the photometry on SN 1994I from Richmond et al. (1996). This is a SN Ic, but we use it as a template for all SN Ib/c, taking the view that there is little point in trying to distinguish between SN Ibs and SN Ics in our simulations. It is not even clear that they are intrinsically

| SN Type | $M_G$ | $\sigma_G$ |
|---|---|---|
| Type Ia | -18.99 | 0.76 |
| Type Ib/c | -17.75 | 1.29 |
| Type II-L | -17.63 | 0.88 |
| Type II-P | -16.44 | 1.23 |

Table 5.3: The means and dispersions in SNe absolute magnitude at maximum adopted for the Monte Carlo simulations. The numbers are derived from the uncorrected distributions in Richardson et al. (2002), but are adjusted to our preferred Hubble constant of 65 $\mathrm{kms^{-1}Mpc^{-1}}$.

very different, other than in the location of the ionizing source for helium. There is considerable diversity in SNe II lightcurves, as illustrated in Patat et al. (1994). We use the photometry of Cappellaro et al. (1995) on SN 1990K as the basis of our standard template for SNe II-L. However, this is missing the rising part, which is reconstructed using the mean lightcurve data in Doggett & Branch (1985). We use the photometry of Hamuy et al. (2001) on SN 1999em as a template for SN II-P.

Lastly, the lightcurves are sampled according to Gaia's scanning law[2] using software kindly supplied by L. Lindegren. Gaia has three telescopes on board. ASTRO-1 and ASTRO-2 perform astrometry and broad-band photometry on all objects brighter than $G \sim 20$. SPECTRO performs spectroscopy and medium-band photometry. The spacecraft is assumed to rotate about its spin axis once every $\sim 3$ hours, performing a great circle scan. (This corresponds to the prototype, although a slower spin rate may be adopted in the final mission). The spin axis is constrained to move on a Sun-centered cone of 55° with a period of 76 days, forcing the plane of the scan to sway back and forth. The axis of the cone follows the yearly solar motion (see ESA 2000). The number of times an object enters the fields of view of ASTRO-1 and ASTRO-2 during mission lifetime depends on ecliptic latitude and is shown in Figure 5.2.

[2]This Chapter uses the scanning law from the original version of the satellite design. The most up-to-date version of the scanning law is presented in Chapter 6

## 5.3 Results

### 5.3.1 Numbers detected

Figure 5.3 shows the fraction of SNe within a distance $D$ which enter the field of view of Gaia's telescopes ASTRO-1 and ASTRO-2. Gaia records data on 30% of all the SNe Ia within 630 Mpc, which marks the limit of the most distant SNe Ia accessible. The distance cut-offs for the intrinsically less bright SNe Ib/c, II-L and II-P are 355 Mpc, 335 Mpc and 195 Mpc respectively. Gaia records data on $\sim$ 20% of all SNe Ib/c, $\sim$ 31% of all SNe II-L and $\sim$ 48% SNe II-P within these distances. This means that Gaia will provide some (perhaps rather limited) information on 14 300 SNe Ia and 1400 SNe Ib/c during its five-year mission. For SNe II, the number depends on the relative frequency $f_{\mathrm{II}}$ and is $\sim 8700 f_{\mathrm{II}} + 2700(1 - f_{\mathrm{II}})$. If SNe II-L and SNe II-P occur equally frequently ($f_{\mathrm{II}} = 0.5$), then the total number of SNe II is $\sim$ 5700. In other words, Gaia will provide some information on $\sim$ 21 400 SNe in total. For comparison, Høg et al. (1999) used simple scaling arguments to estimate that the total number of SNe in the Gaia observations would be $\sim$ 100 000.

These are huge numbers, both compared to the sizes of existing catalogues and to the likely datasets gathered by other planned space missions. Almost all the SNe that Gaia misses explode in the 20 days just after Gaia samples that location in the sky. Before the next transit of ASTRO-1 or ASTRO-2, the SN reaches maximum and then fades to below Gaia's limiting magnitude ($G \sim 20$). It may be wondered whether some SNe are missed because light from the background galaxy can overwhelm the SN. This is clearly a problem for distant galaxies, which are wholly contained within Gaia's PSF ($\sim .35''$ at FWHM). However, rough calculations show that this is not a problem for SNe Ib/c and II, as they occur relatively close by; we estimate that it may affect $\lesssim 10\%$ of SNe Ia. Figure 5.4 shows the fraction of the detected SNe as a function of phase

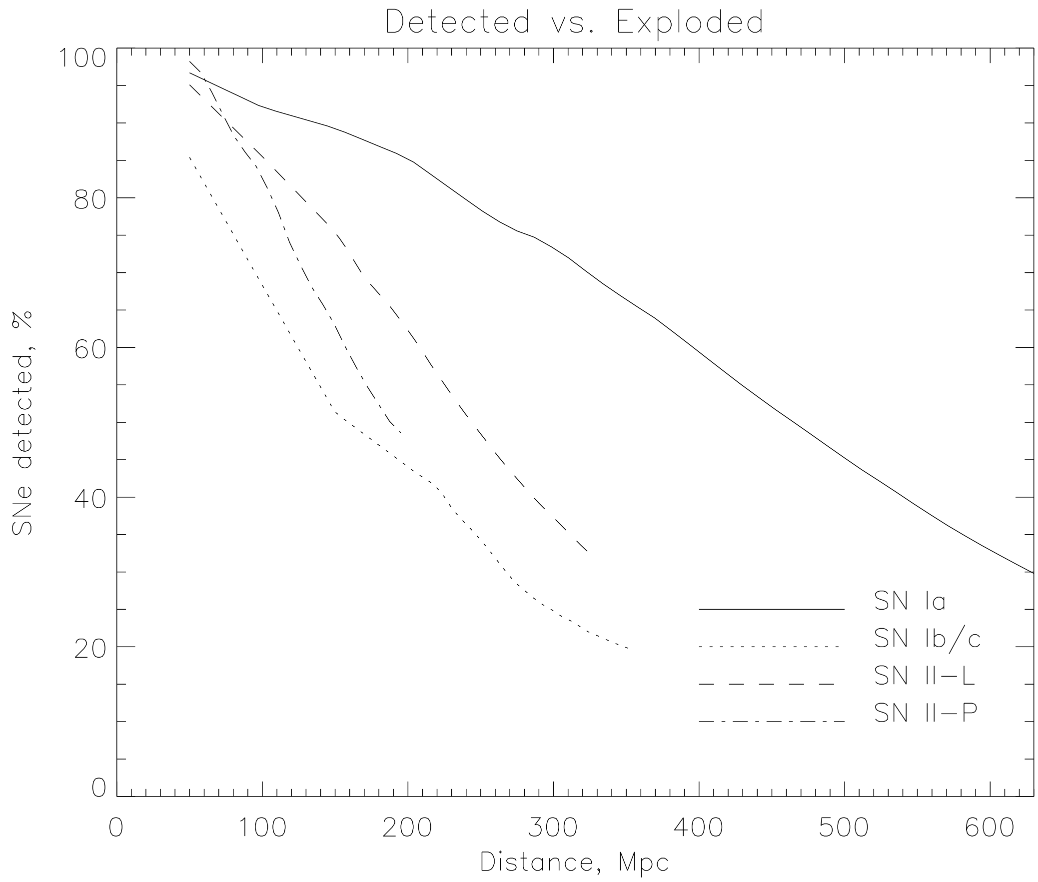


Figure 5.3: This shows the total number of SNe detected within distance $D$ as a fraction of the total number exploded. Within 630 Mpc, Gaia detects $\sim$ 30% of all SNe Ia. Within 355 Mpc, Gaia detects $\sim$ 20% of all SNe Ib/c. For SNe II-L, Gaia detects $\sim$ 31% within 335 Mpc. Finally, for SNe II-P, Gaia detects $\sim$ 48% within 195 Mpc. Note that by detection, we mean that Gaia records at least one datapoint on the standard SNe templates shown in Figure 5.1.

of the lightcurve. Some 44% of the detected SNe Ia are caught before maximum, 37% of the detected SNe Ib/c, 37% of the detected SNe II-L and 9% of the detected SNe II-P. The low fraction for SNe II-P is largely a consequence of the fact that they are intrinsically the faintest. The numbers of each type of SNe caught before maximum by Gaia are recorded in Table 5.4. The total number of all SNe found before maximum during the 5 year mission lifetime is $\sim 8500$. This number can be broken down into $\sim 6300$ SNe Ia, $\sim 500$ SNe Ib/c and 1700 SNe II (assuming $f_{\rm II} = 0.5$). If data on a SN is taken before maximum, then Gaia has an excellent chance of identifying the rapidly brightening object as a SN.

### 5.3.2 Identification strategy

Every new object in a field of view is potentially a SN. Before Gaia can identify a SN, it must have visited that location on the sky at least once before. To provide SN alerts, we must ensure that the brightening object is not just a common variable star. We use the General Catalogue of Variable Stars (Kholopov et al. 1999) to build a subsample of variables with periods in excess of 10 days. Some 34% of this subsample have periods less than 6 months and 86% have periods less than 1 year. In practice, $\sim 12$ months baseline photometry may be needed to discriminate against common forms of stellar variability. One way round this problems is to restrict SN alerts to high galactic latitudes ($|b| > 30°$), where the problem of variable star contamination is mitigated. The objects that can cause most confusion are fast-moving solar system asteroids and novae. Main Belt asteroids move at $\sim 10$ mas s$^{-1}$ and Near-Earth objects at $\sim 40$ mas s$^{-1}$ (e.g., Mignard 2002). Høg (2002) has shown that fast moving objects can be detected by a single field of view crossing. This offers quick discrimination between solar system asteroids and SNe. More problematical are novae. Shafter (1997) gives the Galactic nova rate as $35 \pm 11$ yr$^{-1}$. We assume that this is typical of large galaxies. We take

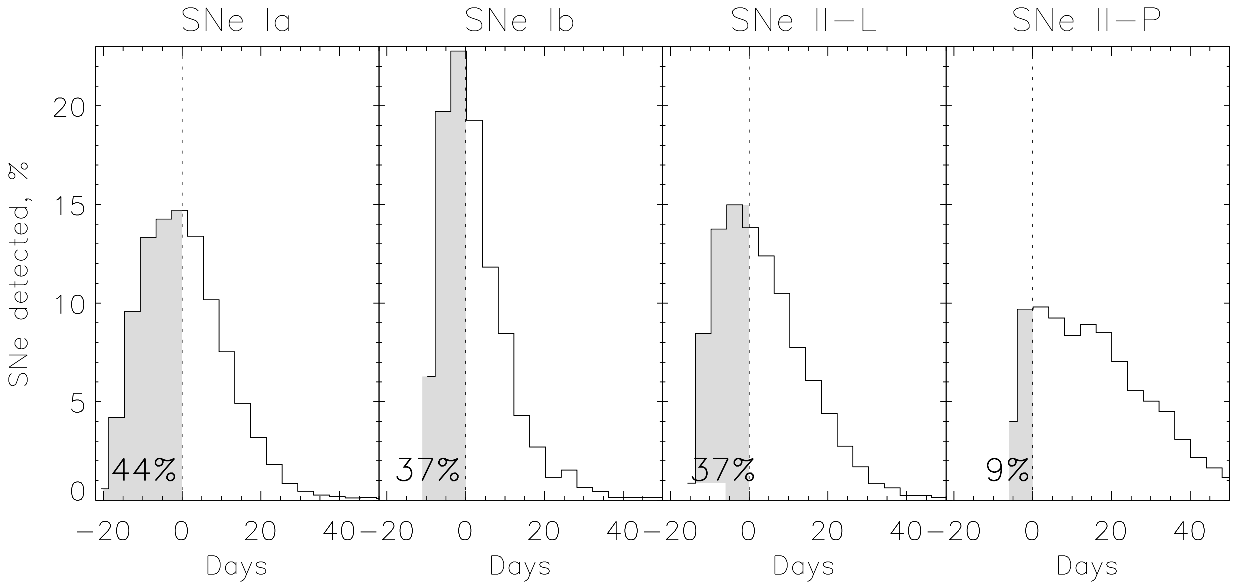


Figure 5.4: This shows histograms of the numbers of detected SNe against phase of the lightcurve. The shaded area corresponds to the fraction of SNe caught before the maximum of the lightcurve.

the absolute magnitude of novae to be in the range $-6 < M < -9$ (Sterken & Jaschek 1996). Given Gaia's limiting magnitude, there are between 20 and 150 galaxies in the CfA catalogue for which novae are detectable. This means that there are $\sim 1000$ novae per year in the Gaia datastream. These can possibly be distinguished from SNe on the basis of colour information and spectroscopy. However, contamination by novae from external galaxies – which is the bulk of the numbers – is restricted to a number of small and pre-determined areas of the sky. These can, if necessary, be excised from the SNe survey. Therefore, a reasonable expectation is that Gaia will alert on all SNe caught before maximum, that is $\sim 1700$ SNe a year. Riess et al. (1998) show how the distance to a SNe Ia can be estimated to within 10% from a single spectrum and photometric epoch. For a 20th magnitude SN, the most suitable combination is a 2m telescope for imaging and a 4m for spectroscopy. On a 2m telescope, it is feasible to carry out high signal-to-noise UBVRI photometry on a 20th magnitude SN in $\lesssim 1$ hr. The typical signal-to-noise needed for identifying the type from spectroscopy is $\sim 30$. This needs $\sim 2$ hrs on a $V \sim 20$ point source in dark sky at low spectral resolution. However,

| SNe | Total number detected | Fraction detected before maximum | Number detected before maximum |
|---|---|---|---|
| Type Ia | 14308 | 44% | 6317 |
| Type Ib/c | 1370 | 37% | 501 |
| Type II-L | $8735 f_{\mathrm{II}}$ | 37% | $3205 f_{\mathrm{II}}$ |
| Type II-P | $2683(1 - f_{\mathrm{II}})$ | 9% | $236(1 - f_{\mathrm{II}})$ |
| Total | 21387 | 40% | 8538 |

Table 5.4: The numbers of SNe of different types detected before maximum during the 5 year Gaia mission lifetime. The last row assumes that the fraction of SNe II-L compared to all SNe II is $f_{\mathrm{II}} = 0.5$.

| Distance | Magnitude | SNe Ia | SNe Ib/c | SNe II-L | SNe II-P | Total |
|---|---|---|---|---|---|---|
| $< 50$ Mpc | $G < 20$ | 23 | 16 | $90 f_{\mathrm{II}}$ | $92(1 - f_{\mathrm{II}})$ | $\sim 130$ |
| $< 100$ Mpc | $G < 20$ | 179 | 107 | $649 f_{\mathrm{II}}$ | $616(1 - f_{\mathrm{II}})$ | $\sim 918$ |
| $< 50$ Mpc | $G > 15$ | 8 | 10 | $65 f_{\mathrm{II}}$ | $75(1 - f_{\mathrm{II}})$ | $\sim 88$ |
| $< 100$ Mpc | $G > 15$ | 115 | 79 | $554 f_{\mathrm{II}}$ | $574(1 - f_{\mathrm{II}})$ | $\sim 758$ |

Table 5.5: The numbers of SNe detected within 50 and 100 Mpc over 5 years. The upper table refers to all SNe brighter than 20th magnitude. However, SNe brighter than 15th magnitude will probably be found beforehand by other means. The lower table gives the numbers of all SNe between 15th and 20th magnitude at maximum light. This gives an idea of the numbers of nearby SNe that only Gaia will find. The last column assumes that the fraction of SNe II-L compared to all SNe II is $f_{\mathrm{II}} = 0.5$.

roughly half the SNe will not be suitable for follow-up from the ground as they will be daytime objects. Assuming we wish to follow up the sample of (nighttime) SNe alerted before maximum, then roughly two dedicated telescopes (say one 2m and one 4m) are required to get distance and phase estimates. This will confirm detection and type. Based on the information from the one night snapshot, selected SNe can be chosen for more detailed monitoring. Candidates for intensive monitoring might include all the SNe Ib/c and II-L (as there is little information on their lightcurves), subluminous and over-luminous events, all SNe Ia caught well before maximum and any SN for which the snapshot gives an unusual luminosity or spectral composition. Tammann & Reindl (2002) have also recently emphasised the value for the extragalactic distance scale of such a follow-up program of Gaia SNe Ia alerts.

## 5.4 Scientific returns

### 5.4.1 Follow-ups, neutrinos and gravitational waves

Of course, it is important to follow up the alerted SN in bandwidths other than the optical, including infrared, X-rays and gamma-rays. This is needed – amongst other things – for the calculation of the bolometric luminosity, which sums together all the flux associated with the energy of the explosion and which provides tests and constraints on the progenitor and detonation models (e.g., Mazzali et al. 2001). More exotically, SNe can also be sought with neutrino and gravitational wave detectors, though these signals reach us before the optical detection.

Infrared and optical photometry of a SN can be used to construct a curve of colour versus time. By matching this to a template with zero reddening, the extinction in the host galaxy can be measured (e.g., Krisciunas et al. 2001) and hence the absolute magnitude and distance of the SN found. There are additional benefits to infrared follow-ups. One of the causes of uncertainty in SNe rates is extinction. For SNe Ib/c and II, which originate in the core collapse of massive stars, the observed rates are likely to be a severe underestimate of the true rate as extinction is usually high – as much as $10-20$ magnitudes – in some starburst regions (Grossan et al. 1999). Of course, the true SNe rate is important for understanding chemical enrichment and evolution of galaxies and the ISM. Infrared photometry, together with Gaia data, will allow the rates to be computed as a function of infrared (rather than blue) luminosity.

X-ray and gamma-rays are associated with the radioactive decay of nuclides produced in the SN explosion or Compton scattering associated with high energy radiation. Only the explosions of SN 1987A and SN 1993J were detected in X-rays, whereas SN 1987A remains the only one thus far detected in gamma-rays. The present generation of satellites, such as the *International Gamma-Ray Astrophysical Laboratory* (INTEGRAL) can detect the gamma-ray signal of SNe out to $\sim 10$ Mpc. However, as Höflich, Wheeler & Khokhlov (1998) point out, next generation Laue telescopes will allow gamma-rays from SNe within $\sim 100$ Mpc to be detected. The numbers of SNe alerted by Gaia within 100 Mpc are listed in Table 5.5. Some of these SNe (typically those brighter than 15th magnitude) are likely to have been found by other means beforehand. So, we conclude that Gaia will alert on $\sim 920$ SNe in total for which the X-ray and gamma-ray signal will be detectable. Of these, $\sim 760$ SNe will not have been discovered by others beforehand.

Gravitational waves may also be sought from nearby SNe. For SNe Ib/c and II, the asymmetry of the core collapse generates gravitational waves which have a typical frequency $\sim 1$ kHz (e.g., Mönchmeyer et al. 1991). For SNe Ia, if the progenitor is a singly degenerate binary (white dwarf and main sequence or red giant star), then no detectable gravitational waves are expected. However, if the progenitor is a double degenerate binary, then the collapse will look like a SN II, probably with a similar output of gravitational waves. The maximal amplitude of gravitational waves for a SN at 30 Mpc is in the range $10^{-21}$ to $10^{-25}$ (e.g., Mönchmeyer et al. 1991, Bonnell & Pringle 1995, Yamada & Sato 1995). The Laser Interferometer Gravitational Wave Observatory (LIGO, see "http://www.ligo.caltech.edu/") is scheduled to begin taking data in 2003. Advanced LIGO will be operational after 2006 and will measure gravitational waves with an amplitude down to $10^{-21}$. This raises the possibility that gravitational waves from SNe within 10-50 Mpc may be detected. From table 5.5, there may be $\sim 130$ SNe alerted by Gaia over 5 years for which detection of the gravitational wave signal is feasible. Note that gravitational waves arrive before any photons. However, the directional sensitivity of gravitational wave detectors is very poor, so Gaia may play an important rôle in identifying the relevant SN.

Lastly, little is known about the neutrino emission from SNe Ia. For SNe associated with core collapse, there are detailed theoretical predictions. However, the only SN for which neutrinos have been detected remains SN 1987A. Neutrinos were registered by the Kamiokande II, the Irvine-Michigan-Brookhaven and the Baksan neutrino detectors. From the three detectors, a combined total of $\sim 25$ neutrinos with energies in the range 10-50 MeV are reckoned to originate from SN 1987A (e.g., Burrows 1989). These are believed to be anti-electron neutrinos, for which the detection cross-section is largest. They were emitted in a burst of $\sim 10$ s associated with the birth of the neutron star. However, both global fits to the SN parameters as well as theory suggest that the Kamiokande II yield was smaller than expected, probably due to statistical fluctuations and the fact that the detector was not optimized at low energies. By comparison, in the 32 kton Super-Kamiokande water-Cerenkov detector, about $10^4$ detected events are expected from a core collapse SN at an assumed distance of 10 kpc (Beacom, private communication). This is larger than the SN 1987A yield in Kamiokande II by roughly the factors 25 (5 times closer), 16 (32 kton detector rather than 2 kton), and 2 (optimisation). In addition, some other reaction channels are expected to become important once the yield is so high.

Scaling this result, the typical number of MeV neutrinos expected from a SN Ib/c or II in a host galaxy at a distance $D$ with a water-Cerenkov detector of volume $V$ is

$$N \sim 30 \left(\frac{\mathrm{Mpc}}{D}\right)^2 \left(\frac{V}{\mathrm{Mton}}\right). \tag{5.1}$$

By Gaia's launch date of 2010, it is reasonable to expect 1 Mton Hyper-Kamiokande detectors and so neutrinos from SNe at distances up to $\sim 5$ Mpc may be detectable. This is the hardest challenge of all! Only a very few such nearby SNe are expected over the 5 year Gaia mission lifetime, and they may perhaps have been found by other means before Gaia alerts on them. However, even today, very nearby SNe are still missed, particularly those that are intrinsically faint or those occurring in obscured parts of the sky

### 5.4.2 Applications

Cosmological problems regarding the dark energy will not be addressed directly by Gaia. Even the most distant SNe that Gaia detects have $z \sim 0.14$. By contrast, Gaia will provide a large dataset of nearby SNe. These are more interesting from the point of view of understanding the properties and the underlying physics of the explosions themselves.

The advantage of SNe surveys with Gaia is that selection effects are either minimised or easy to model, and that there will be many examples of comparatively scarce phenomena (e.g., subluminous SNe, SNe II-L, SNe Ib/c). At present, SNe rates come from relatively small datasets (e.g., Hardin et al. 2000) and are subject to substantial uncertainties. Selection effects – depending on the type of host galaxy, the extinction and the distance from the center of the galaxy – seriously afflict all current datasets. Given the large numbers of alerted SNe, Gaia will provide accurate rates as a function of position, extinction and type of host galaxy. These give valuable, if indirect, information on both the star formation rate and the high mass end of the mass function. There have also been suggestions that populations of subluminous SNe may have been systematically missed in existing catalogues (e.g., Richardson et al. 2002). If so, then Gaia is the ideal instrument with which to find them. The value of Gaia in richly populating the Hubble diagram has also been pointed out recently by Tammann & Reindl (2002).

The nature of the progenitor populations of the different types of SNe – and especially SNe Ia's – will probably remain unsolved over the next decade. Gaia can help as it provides milliarcsecond astrometry or better with a single transit. For a SN at a typical distance of $\sim 200$ Mpc, the projected position can be determined to $\sim 1$ pc (assuming the main error contribution comes from angle measurements). There are only two detections of a SN progenitor before explosion (namely SN 1987A and SN 1993J). Attempts have been made to locate the progenitors of nearby SNe using astrometry with an accuracy of 0.17", though without success so far (Smartt et al. 2002). Gaia will provide milliarcsecond error boxes and therefore it may be easier to locate the progenitor for nearby SNe using HST or other deep search archives. Even if no star is visible, then constraints can still be placed on the progenitor mass, as Smartt et al. (2002) demonstrate. Accurate positional information on the location of SNe within galaxies is important because it sheds light on the spatial distribution (and hence nature) of the progenitor population.

Zampieri et al. (1998) and Balberg & Shapiro (2001) emphasise that the formation of the black hole may also be detectable in nearby SNe as luminosity generated by late-time accretion. This is only possible in the case of subluminous SNe, as otherwise it is masked by radiative heating. Using Figure 4 of Balberg & Shapiro (2001), we see that the fraction of suitable SNe comprise roughly 10% of all core collapse SNe within 50 Mpc. From Table 5.5, it follows that there will be $\sim 10$ SNe Ib/c and II with the required properties alerted by Gaia during the whole mission. If subluminous SNe have been systematically missed in current catalogues, then this number will be still higher. For these SNe, follow-ups may be able to detect the faint luminosity indicative of black hole accretion. This requires scheduling observations with instruments like the *Hubble Space Telescope* or the *Next Generation Space Telescope* of the declining light curve with the hope of observing accretion onto the emerging black hole.

Another application of Gaia's SNe Ia dataset is to measurements of the local velocity field (e.g., Høg et al 1999, Tamman & Reindl 2002). Nowadays, the bulk flow and the bias parameter are often calculated using distance estimators of galaxies such as the Tully-Fisher relationship or the fundamental plane, combined with radial velocity measurements (e.g., Hudson et al. 1999). Typically, this proceeds by finding the best fitting bulk flow $\mathbf{V}$ which minimises

$$\chi^2 = \sum_i \frac{(v_i - \mathbf{V} \cdot \hat{\mathbf{r}}_\mathbf{i})^2}{\sigma_i^2}, \tag{5.2}$$

where $v_i$ is the observed peculiar velocity for the ith galaxy, whose direction vector is $\hat{\mathbf{r}}_\mathbf{i}$, and $\sigma_i$ is an estimate of the error. As pointed out by Riess et al. (1997), SNe Ia offer a more accurate distance estimator than galaxies, as the typical uncertainty is reduced to $\sim 5\%$. In other words, every SNe Ia identified by Gaia can give the distance of its host galaxy with unprecedented accuracy. When combined with ground-based spectroscopy, Gaia will provide $\sim$ 6300 positions and peculiar velocities of galaxies in the nearby Universe. These can be used to study the deviations from the Hubble flow and compared with the velocities predicted by gravity fields of full-sky galaxy catalogues. With such data, not merely the local bulk flow but also the shear field will be measurable.

## 5.5 Conclusions

The theory of SNe explosions is well-developed but somewhat poorly calibrated against data. Nearby SNe are ideal for carrying out such detailed comparisons. Provided we can alert on a large enough sample of SNe, then there are good prospects for the identification of the progenitor population and the detection of the ongoing explosion in all wavebands. All these provide tests and checks on the theory of stellar evolution and SNe detonation. The identification of the gamma-ray and gravitational wave signals may also be possible for close SNe (within 50 Mpc).

We have demonstrated that the astrometric scanning satellite Gaia has exactly the required capabilities. Gaia is the European Space Agency satellite that is the successor to *Hipparcos*. Over Gaia's five year mission lifetime, we estimate that the numbers caught before maximum are $\sim$ 6300 SNe Ia, $\sim$ 500 SNe Ib/c and $\sim$ 1700 SNe II. After launch in about 2010, Gaia will issue $\sim$ 5 SN alerts a day. In total, Gaia will report data on at least 21 400 SNe during the mission, of which $\sim$ 14 300 are SNe 1a, $\sim$ 1400 are SNe Ib/c and $\sim$ 5700 are SNe II. These numbers come from detailed simulations in which SNe explode in galaxies tracing the local large-scale structure. The effects of the dimming of SNe because of absorption in the host galaxy and in the Milky Way are included. The SNe lightcurves are sampled according the scanning law of the satellite. We note that, though huge, these numbers are lower limits. They do not take into account the contribution of SNe in low-luminosity galaxies, which may result in a further doubling of the numbers. They do not take into account the fact that Gaia's limiting magnitude is likely to be somewhat deeper than 20th in practice.

Gaia is complementary to the *SNAP* satellite (see "http://snap.lbl.gov"), which will probe much deeper out to a redshift of $\sim 1.7$ to obtain $\sim 2000$ SNe Ia a year. By contrast, Gaia will obtain data on $\sim 4280$ SNe a year but probe at most out to a redshift of $\sim 0.14$. Gaia will play its role in cosmology by providing a huge dataset of high quality local SNe Ia in which any scatter in the Phillips relation with colour can be quantified and analysed (Tammann & Reindl 2002).

Gaia will provide an important database of nearby SNe which are particularly interesting for studies of the explosions themselves. Many statistics – SNe rates, frequency of different lightcurve morphologies, location in the host galaxy – are poorly known. Gaia will provide the definitive dataset. In particular, SNe rates can be corrected for known biases, such as extinction and position in the host galaxy, and so will be measured with unprecedented accuracy. The huge numbers mean that even examples of comparatively rare phenomena will be present in the database. Despite the enormous efforts of the last decade, there are still very few subluminous SNe, over-luminous SNe, SNe II-L and SNe Ib/c in the standard catalogues. Gaia will present us with good chances of finding examples of nearby subluminous SN Ib/c and II, which are needed to detect the emergence of the black hole. Every SN Ia identified by Gaia can give the distance of its host galaxy with better accuracy than any other method. Thus, the density and velocity field within a few hundred Mpc will be delineated with unprecedented precision.

## 5.6 Bibliography

Balberg S., Shapiro S.L. 2001, ApJ, 556, 944.

Barbon R., Buondí V., Cappellaro E., Turatto M. 1999, A&AS, 139, 531.

Bonnell I.A., Pringle J.E. 1995, MNRAS, 273, L12.

Burrows A., 1989, In “Supernovae: The Tenth Santa Cruz Summer Workshop”, ed. S. Woosley, Springer-Verlag, New York, p. 393

Cappellaro E., Danziger I.J., Della Valle M., Gouiffes C., Turatto M. 1995, A&A, 293, 723

Cappellaro E., Turatto M., Tsvetkov D.Y., Bartunov O.S., Pollas C., Evans R., Hamuy M. 1997, A&A, 322, 431

Ciatti F., Rosino L. 1978, A&AS, 34, 387

Doggett J.B., Branch D. 1985, AJ, 90, 2303

Drimmel R., Spergel D.S. 2001, ApJ, 556, 181

ESA 2000, GAIA: Composition, Formation and Evolution of the Galaxy, Technical Report ESA-SCI(2000)4

Grossan B., Spillar E., Tripp R., Pirzkal N., Sutin B.M., Johnson P., Barnaby D. 1999, AJ, 118, 705.

Hamuy M. et al. 1993, AJ, 106, 2392

Hamuy M., Phillips M.M., Suntzeff N.B., Schommer R.A., Maza J., Smith R.C., Lira P., Aviles R. 1996, AJ, 112, 2438.

Hamuy M. et al. 2001, ApJ, 558, 615

Hardin D. et al. 2000, A&A, 362, 419.

Höflich P., Wheeler J.C., Kholkov A. 1998, ApJ, 492, 228

Høg E., 2002, GAIA-CUO-103

Høg E., Fabricius C., Makarov V.V. 1999, Baltic Astron., 8, 233

Huchra J., Geller M., Clemens C., Tokarz S., Michel A. 1992, Bull. Inf. C.D.S. 41, 31

Hudson M.J., Smith R.J., Lucey J.R., Schlegel D.J., Davies R.L. 1999, ApJ, 512, L79.

Kholopov P.N. et al. 1999, VizieR Online Data Catalog, 2214, 0.

Krisciunas K. et al. 2001, AJ, 122, 1616.

Leibundgut B., Tammann G.A., Cadonau R., Cerrito D. 1991, A&AS, 89, 537.

Leibundgut B. 2000, A&A Rev., 10, 179.

Leibundgut B. 2001, ARAA, 39, 67

Li W., Filippenko A.V., Riess A.G. 2001, ApJ, 546, 719

Lira P. et al. 1998, AJ, 115, 234

Mazzali P.A., Nomoto K., Cappellaro E., Nakamura T., Umeda H., Iwamoto K. 2001, ApJ, 547, 988.

Mignard F. 2002, A&A, in press

Moenchmeyer R., Schaefer G., Mueller E., Kates R.E. 1991, A&A, 246, 417.

Pain R. et al. 1996, ApJ, 473, 356.

Patat F., Barbon R., Cappellaro E., Turatto M. 1994, A&A, 282, 731.

Perlmutter S. et al. 1999, ApJ, 517, 565.

Perryman M.A.C. et al. 2001, A&A, 369, 339

Phillips M.M. 1993, ApJ, 413, L105

Riess A.G., Davis M., Baker J., Kirshner R.P. 1997, ApJ, 488, L1.

Riess A.G., Nugent P., Filippenko A.V., Kirshner R.P., Perlmutter S. 1998, ApJ, 504, 935.

Riess A.G. et al. 1999, ApJ, 118, 2675

Riess A.G. et al. 2001, ApJ, 560, 49

Richardson D., Branch D., Casebeer D., Millard J., Thomas R.C., Baron E. 2002, AJ, 123, 745.

Richmond M.W. et al. 1996, AJ, 111, 327.

Saha A. et al. 2001, ApJ, 551, 973

Schmidt B.P. et al. 1998, ApJ, 507, 46.

Shafter A.W. 1997, ApJ, 487, 226.

Smartt S.J., Gilmore G.F., Tout C.A., Hodgkin S.T. 2002, ApJ, 565, 1089.

Sterken C., Jaschek C. 1996 Lightcurves of Variable Stars, chap. 5 (Cambridge University Press, Cambridge)

Tammann G., Reindl B. 2002, Ap Space Sci, 280, 165

Tsvetkov D.Y., Pavlyuk N.N., Bartunov O.S. 1998, VizieR Online Data Catalog, 2218, 0.

de Vaucouleurs G. 1959, Handbuch der Physik, 53, 275

van den Bergh S., Tammann G.A. 1991, ARAA, 29, 363.

van den Bergh S. 1998, Galaxy Morphology and Classification, chap. 1 (Cambridge University Press: Cambridge)

Yamada S., Sato K. 1995, ApJ, 450, 245.

Zampieri L., Colpi M., Shapiro S.L., Wasserman I. 1998, ApJ, 505, 876

Zwicky F. 1938, PASP, 50, 215

# Chapter 6

# Astrometric Microlensing with the Gaia satellite

This Chapter assesses the microlensing signal that will be seen by Gaia. Section §6.2 gives the formulae for the photometric and astrometric microlensing optical depths. These are used to estimate the total number of microlensing events that Gaia can measure. In §6.3, a covariance analysis is used to demonstrate the effects of error propagation on the recovery of the parameters of microlensing events. §6.4 describes the Galaxy model used to generate microlensing events for our Monte Carlo simulations. The synthetic data are sampled with Gaia's scanning law and realistic errors are applied to provide the one-dimensional astrometric data-streams. §6.5 discusses the results of the simulations, both for the entire sample of events and for the subset of gold-plated events whose parameters can be recovered to good accuracy. Finally, §6.6 examines the overall strategy for identification of events, which need to be distinguished from other forms of astrometric deviation such as binary companions.

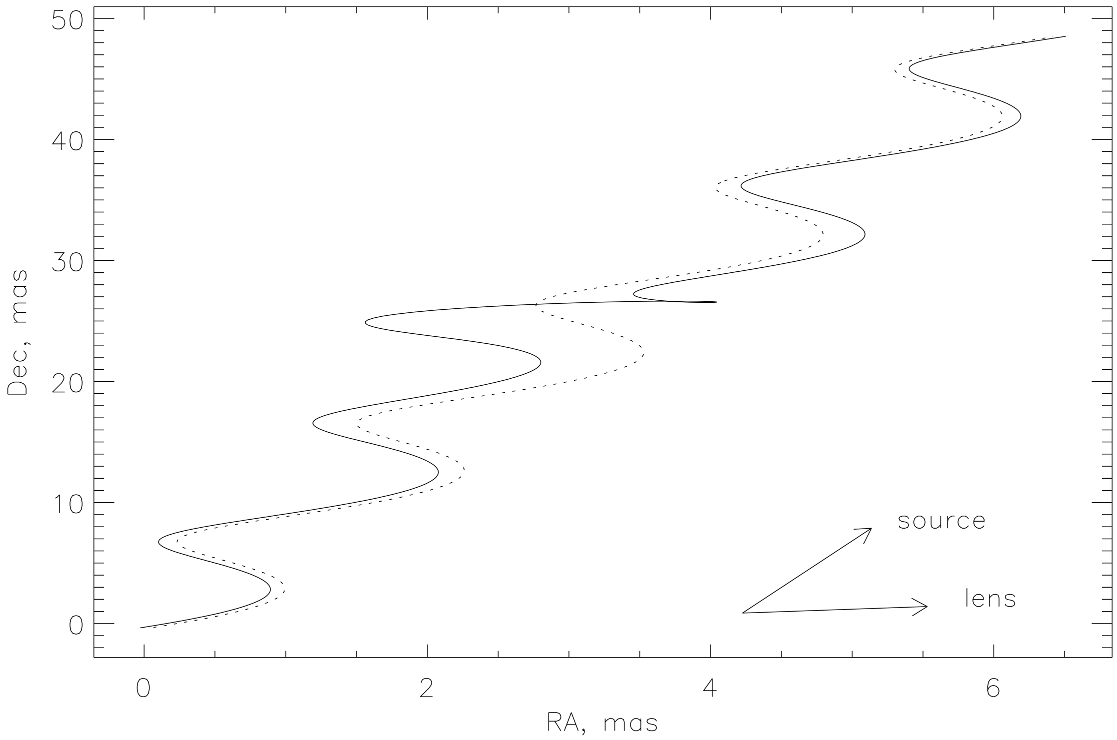


Figure 6.1: This shows the relative right ascension and declination of a source with (solid line) and without (dotted line) a microlensing event. The trajectory is shown over the Gaia mission lifetime of 5 years. Note that the deviations caused by microlensing are present well before and after the time of maximum of the event. (The lens is at 150 pc, the source at 1.5 kpc, the transverse velocity is $70\,\mathrm{km\,s^{-1}}$ and the impact parameter $u_0$ is 1.5. The lens has mass $0.5M_{\odot}$.)

## 6.1 Introduction

A small fraction of the objects monitored by Gaia will show evidence of microlensing. Gaia can observe microlensing by measuring the photometric amplification of a source star when a lens and a source are aligned. This is the approach followed by the large ground-based microlensing surveys like MACHO, EROS, OGLE and POINT-AGAPE (see e.g., Alcock et al. 1997; Aubourg et al. 1995; Udalski et al. 1994, Aurière et al. 2001). Gaia is not very efficient at discovering photometric microlensing events, as the sampling of individual objects is relatively sparse (there are a cluster of observations once every two months on average).

However, there is a more powerful strategy available to Gaia. Although the two images of a microlensed source are unresolvable, Gaia can measure the small deviation (of the order of a fraction of a milliarcsec) of the centroid of the two images around the trajectory of the source. Astrometric microlensing is the name given to this excursion of the image centroid. The cross-section of a lens is proportional to the area it sweeps out on the sky, and so to the product of lens proper motion and angular Einstein radius. Each of these is a declining function of distance, so the signal is dominated by nearby lenses. The detection of astrometric microlensing events for pointed observations has been considered many times before (e.g., Walker 1995; Miralda-Escudé 1996; Paczyński 1996; Boden, Shao & van Buren 1998). Once alerted by a ground-based survey, the events are followed by narrow angle differential astrometry. The detection of astrometric microlensing using observations from a scanning satellite has been considered before by Høg, Novikov & Polnarev (1995) in the context of the proposed ROEMER mission (a forerunner of Gaia).

We will show that the all-sky source-averaged astrometric microlensing optical depth is $\sim 1.5 \times 10^{-5}$, over an order of magnitude greater than the photometric microlensing optical depth. There are two main difficulties facing Gaia in exploiting this comparatively high probability. First, the astrometric accuracy of a single measurement by Gaia depends on the source magnitude and quickly degrades at magnitudes fainter than $G \approx 15$. Second, Gaia provides a time-series of one-dimensional astrometry. The observed quantity is the CCD transit time for the coordinate along the scan. This is the same way the Hipparcos satellite worked (see *The Hipparcos and Tycho Catalogues*, ESA (1997), volume 3, section 16). From the sequence of these one-dimensional measurements, the astrometric path of the source, together with any additional deflection caused by microlensing, must be recovered.

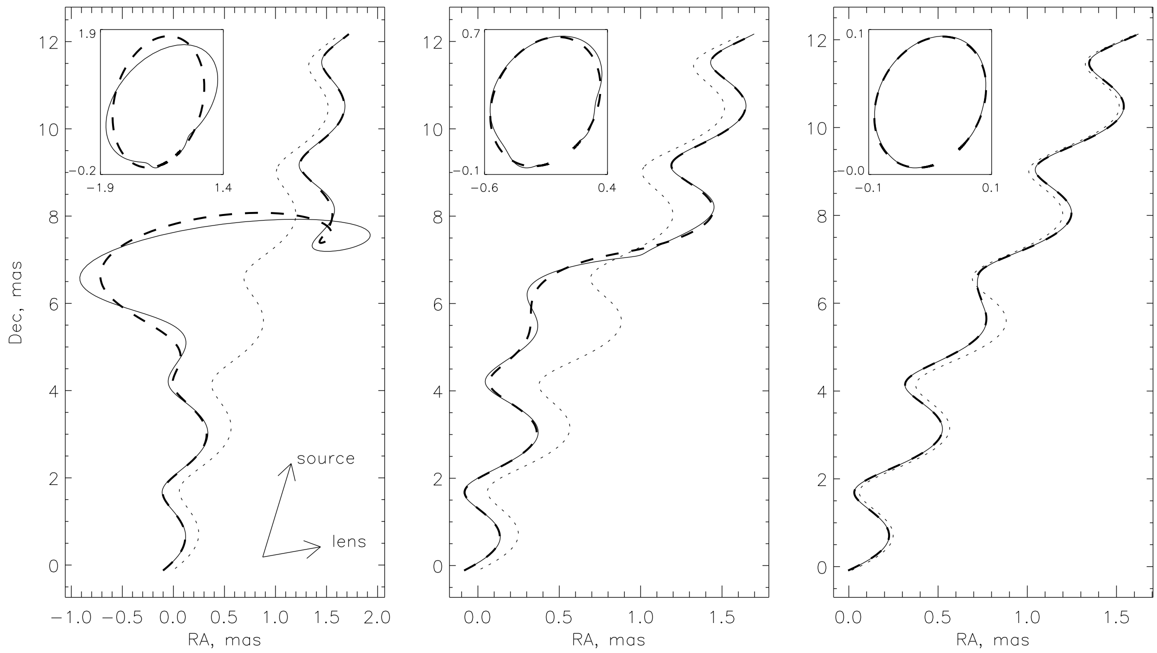


Figure 6.2: The astrometric shift of microlensing events, as seen by a barycentric (dashed line) and a terrestrial observer (solid line). Also shown for comparison is the trajectory of the source without (dotted line) the event. The insets show the deviations with source parallactic and proper motion removed. (The lens is at 150 pc (left), 1kpc (centre) and 5kpc (right), the source at 6.0 kpc, the transverse velocity is $60\,\mathrm{km\,s^{-1}}$ and the impact parameter $u_0$ is 1.5. The lens has mass $0.5 M_{\odot}$.)

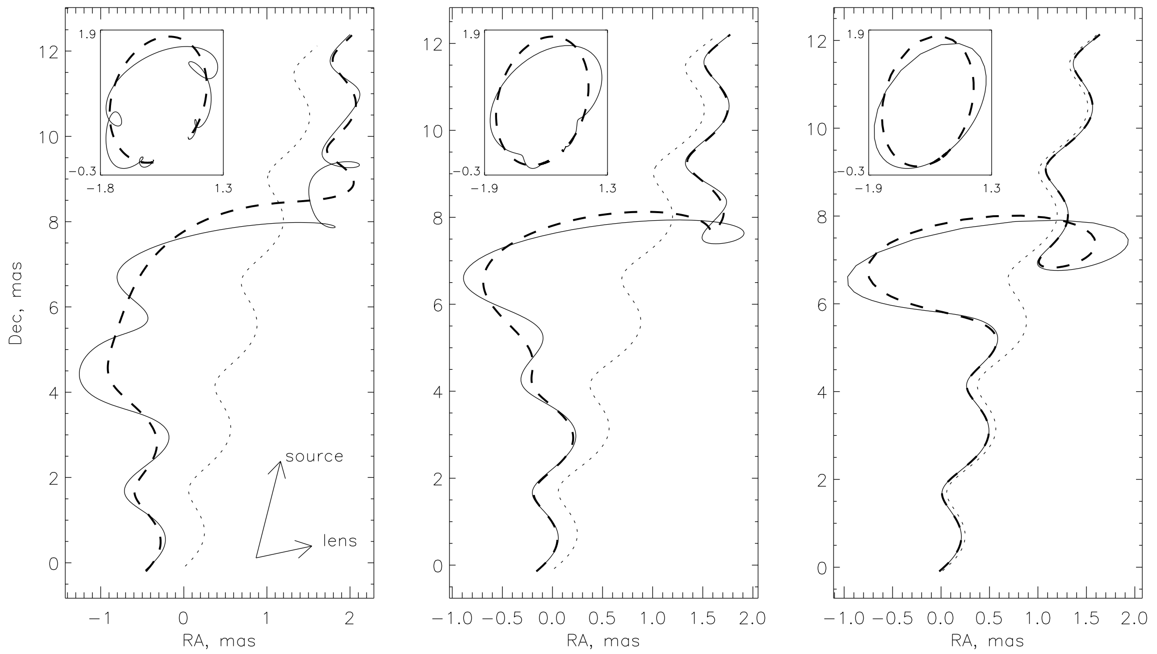


Figure 6.3: As Figure 6.2, but now the transverse velocity varies from $15\,\mathrm{km\,s^{-1}}$ (left), $40\,\mathrm{km\,s^{-1}}$ (centre) and $200\,\mathrm{km\,s^{-1}}$ (right) while the lens is fixed at 150 pc.

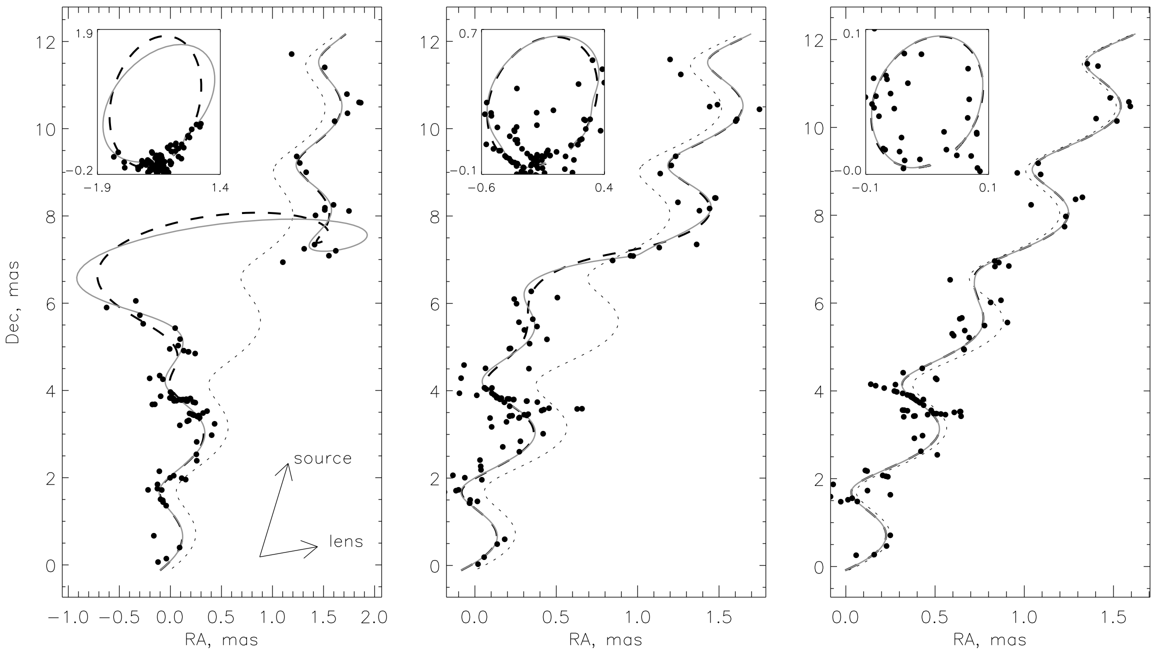


Figure 6.4: As Figure 6.2, but with simulated datapoints using the Gaia scanning law. The accuracy is 150 $\mu$as corresponding to a 16th magnitude star.

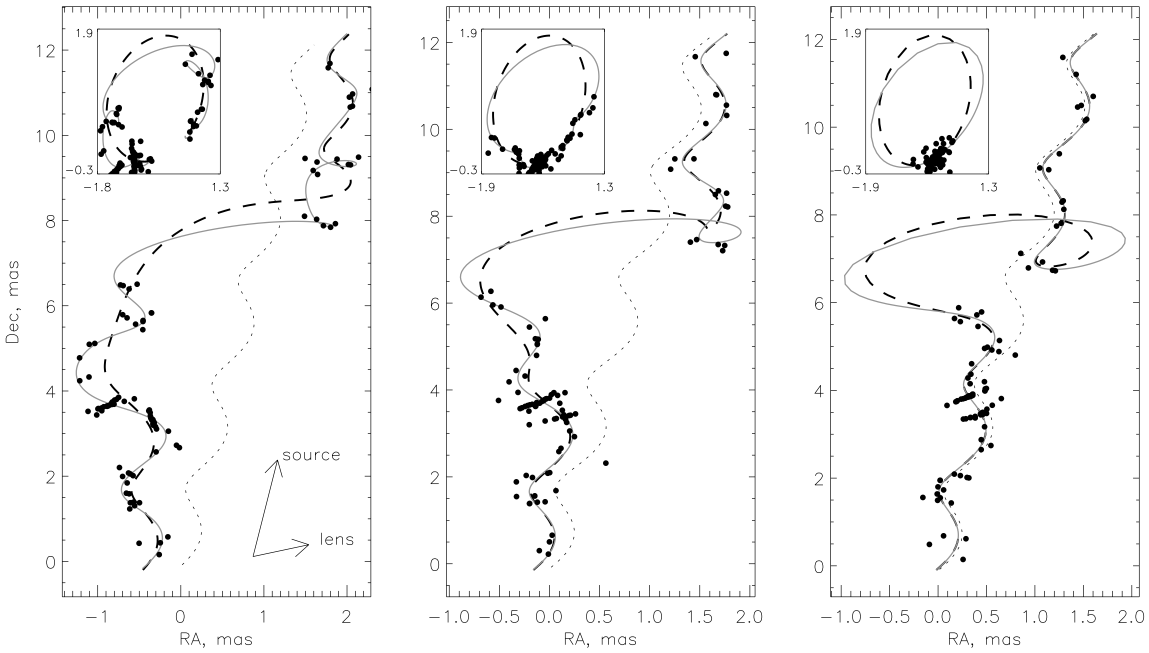


Figure 6.5: As Figure 6.3, but with simulated datapoints using the Gaia scanning law. The accuracy is 150 $\mu$as corresponding to a 16th magnitude star.

## 6.2 Astrometric microlensing

### 6.2.1 General principles

Let us consider the lensing of a luminous source by a dark point lens. (Of course, the lens may be luminous, but we defer consideration of this till §6.6). The angular position of the source $\boldsymbol{\theta}_{\rm s}$ can be written as

$$\boldsymbol{\theta}_{\rm s}(t) = \boldsymbol{\theta}_{\rm s,0} + \boldsymbol{\mu}_{\rm s} t + \mathbf{P}_{\rm s}, \tag{6.1}$$

where $\boldsymbol{\theta}_{\rm s,0}$ is the zero-point, $\boldsymbol{\mu}_{\rm s}$ is the source proper motion and $\mathbf{P}_{\rm s}$ is the source parallax. Similarly, the angular separation between source and lens is given by

$$\boldsymbol{\theta}_{\rm rel}(t) = \boldsymbol{\theta}_{\rm rel,0} + \boldsymbol{\mu}_{\rm rel} t + \mathbf{P}_{\rm rel}, \tag{6.2}$$

where the proper motion $\boldsymbol{\mu}_{\rm rel}$ and parallax $\mathbf{P}_{\rm rel}$ are of the source relative to the lens.

Microlensing induces an additional shift of the source centroid. Letting $\mathbf{S}(t)$ be the image centroid, we have (e.g., Walker 1995; Dominik & Sahu 2000)

$$\mathbf{S}(t) = \boldsymbol{\theta}_{\rm s}(t) + \boldsymbol{\theta}(t), \qquad \boldsymbol{\theta} = \frac{\boldsymbol{\theta}_{\rm rel}(t)}{(\theta_{\rm rel}(t)/\theta_{\rm E})^2 + 2}. \tag{6.3}$$

Here, the angular Einstein radius $\theta_{\rm E}$ is related to the lens mass $M$ by

$$\frac{\theta_{\rm E}}{\rm mas} = \left(\frac{M}{0.12 M_\odot}\right)^{1/2} \left(\frac{\pi_{\rm rel}}{\rm mas}\right)^{1/2}, \tag{6.4}$$

where $\pi_{\rm rel} = |\mathbf{P}_{\rm rel}|$. Figure 6.1 shows the astrometric trajectory of the same source with and without a microlensing event. In this case, the lens is just 150 pc away from the observer, while the source is a disk star 1.5 kpc away. The microlensing event causes the additional excursion superimposed on the parallactic and proper motion of the source.

The characteristic length-scale in microlensing is the Einstein radius $r_{\mathrm{E}} = D_{\mathrm{l}}\theta_{\mathrm{E}}$. It is the linear size of the angular Einstein radius in the lens plane. For applications in the Galaxy, we find that

$$r_{\mathrm{E}} = 9\mathrm{AU}\sqrt{\frac{\mathrm{M}}{\mathrm{M}_{\odot}}}\sqrt{\frac{\mathrm{D_l}}{10\ \mathrm{kpc}}}\sqrt{1-\frac{\mathrm{D_l}}{\mathrm{D_s}}}, \tag{6.5}$$

and so $r_{\mathrm{E}}$ is of the typical size of a few astronomical units (aus). Here, $D_{\mathrm{l}}$ and $D_{\mathrm{s}}$ are the distances from the observer to the lens and source respectively. The characteristic timescale in photometric microlensing is the Einstein crossing time $t_{\mathrm{E}}$, which is the time taken for the source to cross the Einstein radius.

### 6.2.2 The centroid shift

The centroid shift points away from the dark lens as seen by the source. The dimensionless function

$$\mathbf{u} = \frac{\boldsymbol{\theta}_{\mathrm{rel}}}{\theta_{\mathrm{E}}} \tag{6.6}$$

is the angular separation in units of the angular Einstein radius. For $u \to \infty$, the centroid shift falls off like

$$S = |\mathbf{S}| \sim \frac{\theta_{\mathrm{E}}}{u}. \tag{6.7}$$

This can be compared with the photometric magnification $A$, which falls off like

$$A = \frac{u^2+2}{u\sqrt{u^2+4}} \sim 1 + \frac{2}{u^4}. \tag{6.8}$$

These asymptotic results illustrate one of the important differences between astrometric and photometric microlensing. The centroid shift falls off much more slowly than the magnification, so that the cross-section for astrometric events is much larger than for photometric events (e.g., Paczyński 1996; Miralda-Escudé 1996).

In the absence of the proper and parallactic motion, the absolute value of the centroid shift is

$$\theta = \frac{\sqrt{u_0^2 + \hat{t}^2}}{u_0^2 + \hat{t}^2 + 2}\theta_{\mathrm{E}}. \tag{6.9}$$

Here, $u_0$ is the value of the dimensionless distance at the time of closest approach $t_0$ and

$$\hat{t}(t) = \frac{t - t_0}{t_{\mathrm{E}}} = \frac{\mu_{\mathrm{rel}}(t - t_0)}{\theta_{\mathrm{E}}}. \tag{6.10}$$

The shift can be decomposed into components parallel and perpendicular to the direction of motion of the lens relative to the source, namely

$$\theta_{||} = \frac{\hat{t}}{u_0^2 + \hat{t}^2 + 2}\theta_{\mathrm{E}}, \qquad \theta_{\perp} = \frac{u_0}{u_0^2 + \hat{t}^2 + 2}\theta_{\mathrm{E}}. \tag{6.11}$$

As pointed out by Walker (1995), the centroid shift as seen by a barycentric observer is an ellipse. For $u_0 \to 0$, the ellipse becomes a straight line, while for $u_0 \to \infty$, it becomes a circle. Figure 6.2-6.3 shows how the centroid shift changes with differing lens distances and transverse velocities. The dotted line is the path of the source without any microlensing event, the dashed line is that recorded by a barycentric observer and the solid line is that recorded by a terrestrial observer (or equivalently a satellite at the $L_2$ Lagrange point, like Gaia). In the insets, the proper and parallactic motion of the source have been subtracted out. The size of the shift declines substantially as the separation between lens and source decreases. The duration of the shift diminishes as the transverse velocity becomes larger.

However, Gaia does not provide the data in such a clean form, as it really measures a series of one-dimensional transits of the two-dimensional astrometric curve. Figures 6.4-

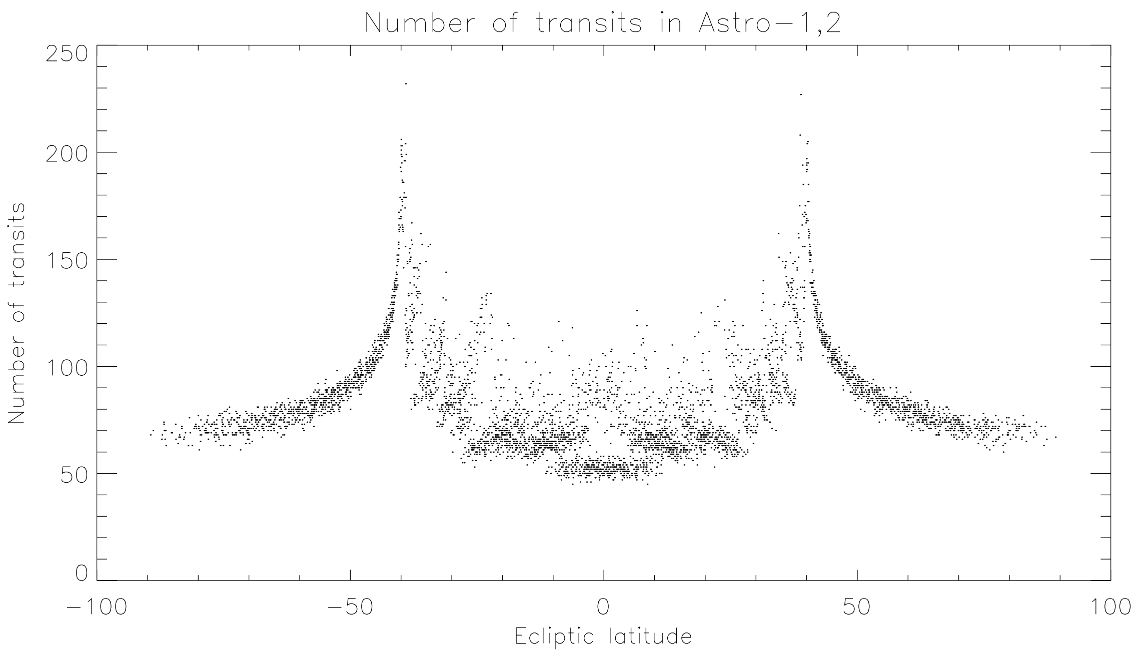


Figure 6.6: This shows the number of transits made by the ASTRO-1 and ASTRO-2 telescopes as a function of ecliptic latitude. The figure is drawn by choosing 5000 random directions on the sky, and computing the ecliptic latitude and number of transits using software supplied by L. Lindegren. It should be remembered that the number of transits may be misleading, as the transits are strongly clustered into groups of between two and five.

6.5 show the events as seen by Gaia. The simulated datapoints have been produced by generating random transit angles, and sampling the astrometric curve according to Gaia's scanning law for the ASTRO-1 and ASTRO-2 telescopes (using programs freely available from L. Lindegren at Lund Observatory). The transits are strongly clustered, as Gaia spins on its axis once every 3 hours and so may scan the same patch of sky four or five times a day. The transit angle is the same for all transits in such a cluster, but changes randomly from cluster to cluster. Gaussian astrometry errors with standard deviation $\sigma_{\mathrm{a}} = 150\ \mu$as have been added to the simulated datapoints. As shown in the insets, the traversal of the elliptical distortion is highly non-uniform, and most of the data are concentrated at epochs when the shift is small. Nonetheless, it is clear that the data-streams will sometimes be poorly fitted by a model without microlensing, from which it is evident that Gaia can detect that a microlensing event has occurred. This is most likely to happen for relatively nearby, slow-moving lenses. It is already clear from the panels that it will be difficult to extract physical information from some of the events, particularly those with smaller Einstein radius.

### 6.2.3 Optical depths

The probability $\tau$ of detecting a microlensing event with certain characteristics is just

$$\tau = D_{\rm s} \int_0^1 dx \int_0^\infty dM \, \frac{\rho(x)}{M} \Sigma(x, M) f(M), \tag{6.12}$$

where $\Sigma$ is the area in the lens plane for which the projected source positions yield the required effect and $f(M)$ is the mass function or the fraction of lenses with mass in the range $M$ to $M + dM$.

Gaia measures displacements only along the scan, so we incorporate a factor of $\sqrt{2}$ to take us from Gaia's one-dimensional astrometric accuracies to the two-dimensional accuracies. The centroid shift varies by more than $5\sqrt{2}\sigma_{\rm a}$ when the projected position of the source lies within a circle of radius $u_{\rm a} r_{\rm E}$, where (Dominik & Sahu 2000)

$$u_{\rm a} = \sqrt{\frac{T_{\rm life} v}{5\sqrt{2}\sigma_{\rm a} D_{\rm l}}} = \sqrt{\frac{T_{\rm life}\theta_{\rm E}}{5\sqrt{2}\sigma_{\rm a} t_{\rm E}}}. \tag{6.13}$$

Here, $T_{\rm life}$ is the lifetime of the satellite and $v$ is the transverse source velocity in the lens plane. Note that $5\sqrt{2}\sigma_{\rm a}$ is enough for Gaia to make a convincing measurement of the shift, but not usually enough for detection of a microlensing event.

Instead, the minimum criterion needed to detect the event in the Gaia database is a variation of centroid shift larger than $5\sqrt{2}\sigma_{\rm a}$ together with a closest approach between lens and source happening with a time $T_{\rm life}$. The area in the lens plane giving rise to events with these characteristics is $\Sigma = 2u_{\rm a} r_{\rm E} T_{\rm life} v$. Using (6.12), the probability is

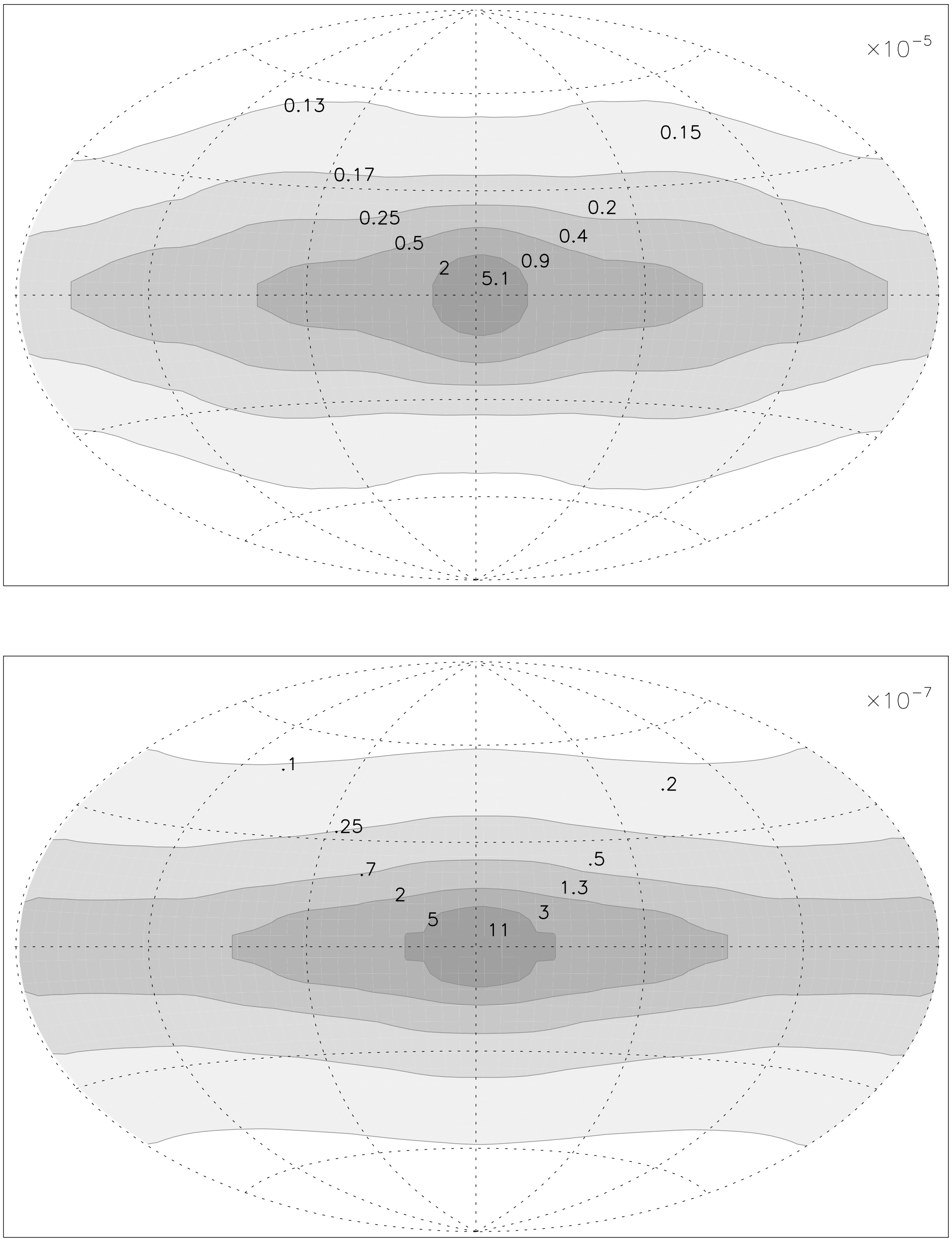


Figure 6.7: Upper panel: An all-sky map of the source-averaged astrometric optical depth. Meridians of Galactic latitude are shown at 60° intervals, parallels of longitude at 30° intervals. The contour levels are marked. The number within each contour refers to the mean value of the optical depth inside the shaded region enclosed between the contours. All numbers are in units of $10^{-5}$. Lower panel: As the upper panel, but for the photometric microlensing optical depth. All numbers are in units of $10^{-7}$. To find the instantaneous number of events in any region, we multiply the average optical depth by the number of stars from Figure 6.8 (for details of the source and lens populations and extinction model, see §6.4).

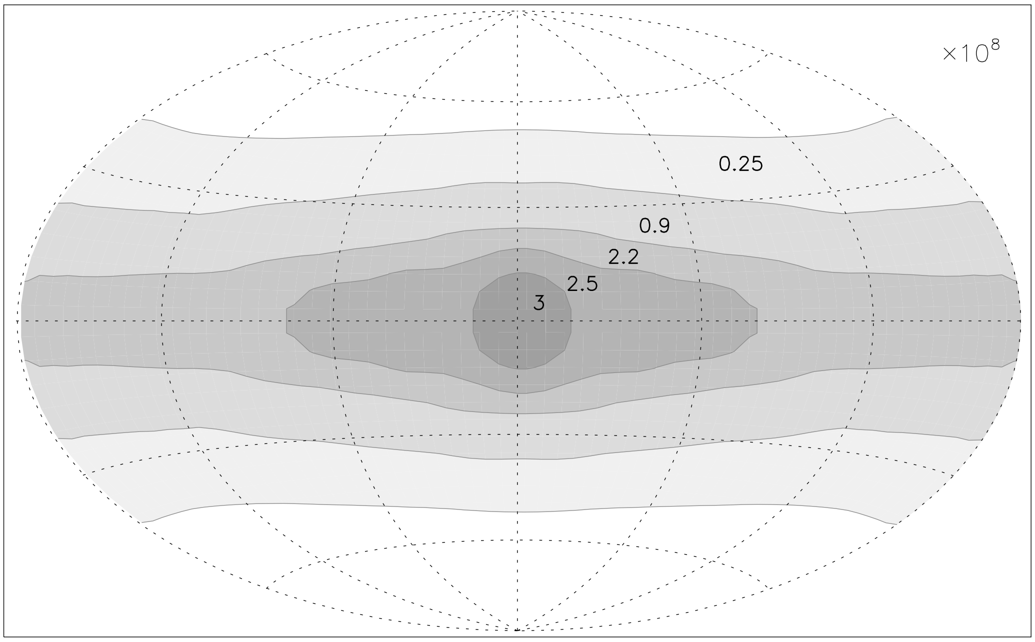


Figure 6.8: This shows an all-sky map of the starcounts. The number within each contour refers to the total number of stars inside the shaded region enclosed between the contours.

(Dominik & Sahu 2000)

$$\tau_{\rm a} = 4\sqrt{\frac{G}{c^2}} D_{\rm s} \langle M^{-1/2} \rangle \sqrt{\frac{T_{\rm life}^3 v^3}{5\sqrt{2}\sigma_{\rm a}}} \int_0^1 dx\, \rho(x) \sqrt{1-x}, \tag{6.14}$$

where

$$\langle M^{-1/2} \rangle = \int_0^\infty M^{-1/2} f(M) dM. \tag{6.15}$$

We refer to the quantity (6.14) as the astrometric microlensing optical depth.

By contrast, the probability of a microlensing event with an amplification greater than that corresponding to the threshold of photometric accuracy $5\sigma_{\rm p}$ is (e.g., Griest

| $G$ (in mag) | 10 | 11 | 12 | 13 | 14 | 15 | 16 | 17 | 18 | 19 | 20 |
|---|---|---|---|---|---|---|---|---|---|---|---|
| $\sigma_{\rm p}$ (in mmag) | 9 | 9 | 9 | 9 | 9 | 10 | 12 | 16 | 23 | 36 | 60 |
| $\sigma_{\rm a}$ (in $\mu$as) | 30 | 30 | 30 | 40 | 60 | 90 | 150 | 230 | 390 | 700 | 1400 |

Table 6.1: This table lists the mean accuracy in photometry $\sigma_{\rm p}$ and in position $\sigma_{\rm a}$ versus $G$ band magnitude for the Gaia satellite. Note that $\sigma_{\rm a}$ is the accuracy of a single astrometric measurement, not the target accuracy at the end of the Gaia mission, which is better by a factor of $\sim 10$. The values are approximate sky averages, adapted from Tables 7.3 and 8.2 of ESA (2000).

1991, Dominik & Sahu 2000), namely

$$\tau_{\rm p} = \frac{4\pi G}{c^2} u_{\rm p}^2 D_{\rm s}^2 \int_0^1 dx\, \rho(x) x(1-x), \tag{6.16}$$

where

$$u_{\rm p}^2 = \frac{2}{\sqrt{1 - A_{\rm p}^{-2}}} - 2. \tag{6.17}$$

Here, $A_{\rm p}$ is the magnification corresponding to the threshold photometric accuracy $5\sigma_{\rm p}$. We refer to the quantity (6.16) as the photometric microlensing optical depth. For Gaia, both the astrometric and photometric accuracies depend on the magnitude of the source as listed in Table 6.1. The Einstein crossing time $t_{\rm E}$ is the time taken for the source to cross the Einstein radius. This is not the duration of a photometric event, which is the time taken for the source to cross a circle of radius $u_{\rm p} r_{\rm E}$ in the lens plane. The duration of an astrometric event is the time for which the centroid shift is greater than the threshold $5\sqrt{2}\sigma_{\rm a}$. Dominik & Sahu (2000) show that this is proportional to the time taken to cross a circle of radius $r_{\rm E}\theta_{\rm E}/(5\sqrt{2}\sigma_{\rm a})$. So, the duration of an astrometric event is

$$t_{\rm ae} = t_{\rm E} \frac{2 u_0 \theta_{\rm E}}{5\sqrt{2}\sigma_{\rm a}}. \tag{6.18}$$

For Gaia, this is typically a factor of two times longer than the duration of a photometric event.

Figure 6.7 shows contours of astrometric and photometric microlensing optical depth together with starcounts. The maps assume a standard model for the sources and lenses in the Galaxy, together with a luminosity function and extinction law (described in §6.4). Extinction is an important effect for Gaia's microlensing capabilities, as the accuracy of both the astrometry and photometry depends on source magnitude. Taking into account the effects of extinction, the all-sky averaged value of the astrometric optical depth is $1.5 \times 10^{-5}$. Here, the averaging is performed by weighting the optical depth with the starcount density. Regions like the Galactic bulge are very heavily weighted, and so the average astrometric optical depth is of the same order of magnitude as the typical optical depth towards the central part of the Galaxy. There are $\sim 10^9$ stars brighter than $V = 20$ in our model; the same is true for the Galaxy (Mihalas & Binney 1981). This means that, during the Gaia mission, there are $\sim 15000$ astrometric microlensing events, which have a variation of the centroid shift greater than $5\sqrt{2}\sigma_{\rm a}$ together with a closest approach during the mission lifetime. This number can be read off Figure 6.7, by multiplying the mean astrometric optical depth within the central contour of the upper panel by the total number of stars within the central contour of the lower panel. Some of these displacements cannot be identified by Gaia as microlensing events, first because the signal-to-noise will often be low and second because any identification algorithm must not generate too many false detections. The middle panel of Figure 6.7 shows contours of photometric microlensing optical depth again including the effects of extinction. This map uses the accuracies appropriate after photometric calibration (perhaps of the order of a month after the start of the mission). Assuming calibration has taken place, then the all-sky averaged photometric optical depth is $\sim 5 \times 10^{-7}$. Let us recall that, from eqs (6.16-6.17), a photometric event occurs whenever there is $5\sigma_{\rm p}$ variation. The typical event duration is $\sim 2-3$ months, so that there are a total of $\sim 8000-14000$ photometric microlensing events during the Gaia mission. However, a very substantial number of these events will be undetectable. Gaia's sampling is sparse compared to ground-based programs like MACHO, EROS or POINT-AGAPE, so many of these events will be missed.

## 6.3 Error propagation

### 6.3.1 Covariance analysis

Our first task is to understand the propagation of errors, so that we can assess how many of the $\sim 15000$ potential astrometric microlensing events are useful.

Most events will not be detected photometrically by Gaia. The measured quantity that will generally be provided by Gaia is the source displacement along the scan. This contains information on the microlensing event, but is contaminated with the source parallactic and proper motion as well. (We assume that the Gaia data-stream has already been corrected for aberration due to satellite motion and gravitational deflection caused by Solar System objects). Most of the results we present here assume only astrometric data. However, this is pessimistic, as it is likely that ground-based surveys will be able to follow-up events alerted by Gaia. So, we also show the effects of incorporating photometric data on the accuracies. The components of $\mathbf{S}$ resolved with respect to right ascension $\alpha$ and declination $\delta$ are

$$(S_\alpha, S_\delta) = \boldsymbol{\theta}_\mathrm{s} + \frac{\mathbf{u}}{u^2+2}\theta_\mathrm{E}. \tag{6.19}$$

The angular position of the source $\boldsymbol{\theta}_\mathrm{s}$ contains the contributions from the source proper motion $\boldsymbol{\mu}_\mathrm{s}$ and source parallax $\mathbf{P}_\mathrm{s}$. We note that

$$\mathbf{u} = \begin{pmatrix} \hat{t}\cos\phi - u_0\sin\phi - \pi_\mathrm{rel}P_\alpha\theta_\mathrm{E}^{-1} \\ \hat{t}\sin\phi + u_0\cos\phi - \pi_\mathrm{rel}P_\delta\theta_\mathrm{E}^{-1} \end{pmatrix} \tag{6.20}$$

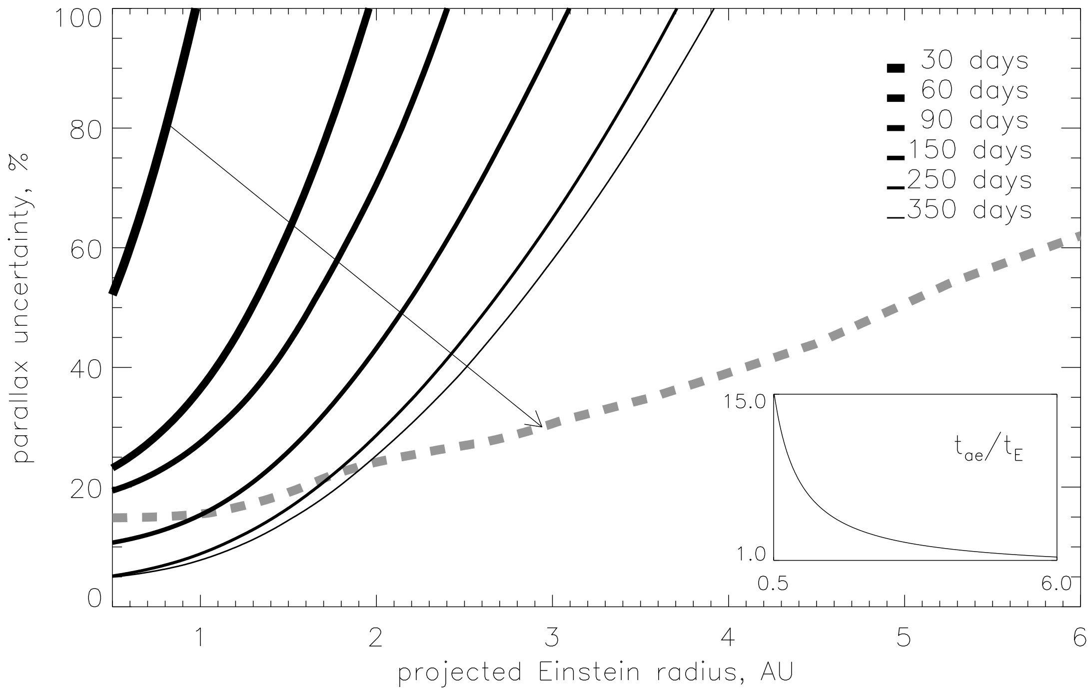


Figure 6.9: This shows the percentage error in estimation of the relative parallax as a function of the projected Einstein radius $\tilde{r}_{\mathrm{E}}$ for different Einstein crossing times and a given accuracy $\sigma_{\mathrm{a}} = 150\ \mu$as. The events have a lens distance varying between 50 pc and 1.5 kpc, but the source distance is fixed at 4 kpc, the impact parameter $u_0$ is 1. The grey line shows the improvement when photometric follow-up information is available. For the fixed Einstein crossing time $t_{\mathrm{E}}$ the astrometric event duration $t_{\mathrm{ae}}$ varies as $\theta_{\mathrm{E}}$. The inset shows $t_{\mathrm{ae}}/t_{\mathrm{E}}$ as a function of the projected Einstein radius.

where $\phi$ is the proper motion angle (Gould & Salim 1999). We have also expanded the parallaxes $\mathbf{P}_{\mathrm{s}}$ and $\mathbf{P}_{\mathrm{rel}}$ as

$$\mathbf{P}_{\mathrm{s}} = \pi_{\mathrm{s}} \left( P_\alpha, P_\delta \right), \qquad \mathbf{P}_{\mathrm{rel}} = \pi_{\mathrm{rel}} \left( P_\alpha, P_\delta \right), \tag{6.21}$$

so that $\pi_{\mathrm{s}}$ and $\pi_{\mathrm{rel}}$ are the absolute values and $P_\alpha$ and $P_\delta$ are the direction cosines (given in van der Kamp 1967).

The directions along and perpendicular to the scan are related to right ascension and declination by a rotation, which depends on where the satellite is pointing. As Gaia continuously scans the sky, this angle can take any value for the same source. So,

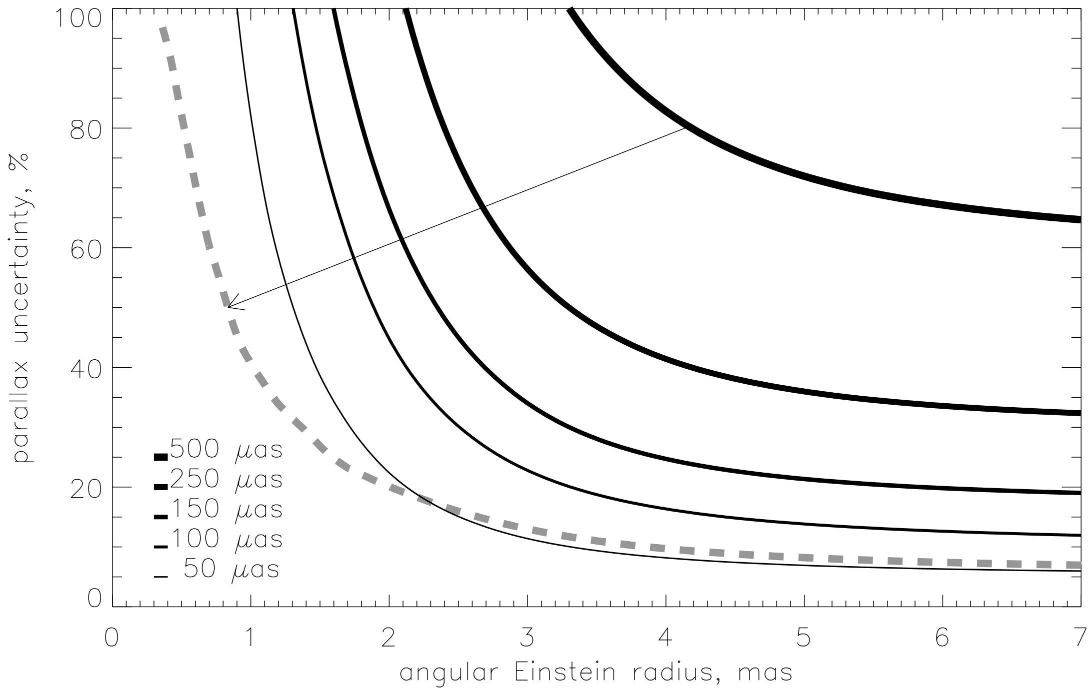


Figure 6.10: This shows the percentage error in estimation of the relative parallax as a function of the angular Einstein radius $\theta_{\rm E}$ for different astrometric accuracies. Again, the grey line shows the improvement when photometric follow-up information is available.

formulae (6.19)-(6.21) hold good in the scan coordinate system as well, after rotation by a random angle to take us from the right ascension and declination to the along-scan and across-scan coordinates. Gaia measures positions in the along-scan direction only.

We use this microlensing model to create synthetic astrometric measurement sets. There are a total of 11 parameters which we wish to compute from the data, namely: $\boldsymbol{\mu}_{\rm s}$, $\pi_{\rm s}$, $u_0$, $t_0$, $t_{\rm E}$, $\phi$, $\theta_{\rm E}$, $\pi_{\rm rel}$ and $\boldsymbol{\theta}_{\rm s,0}$. To study parameter estimation performance, we evaluate the covariance matrix $c_{ij}$ (see e.g., Boutreux & Gould 1996; Gould & Salim 1999). This is defined as the matrix $\mathbf{C} = \mathbf{B}^{-1}$, where

$$b_{ij} = \sum_{k=1}^{N} \sigma_{\rm a}^{-2} \, \frac{\partial \theta_{Gaia}(t_k)}{\partial a_i} \frac{\partial \theta_{Gaia}(t_k)}{\partial a_j}. \tag{6.22}$$

Here $\theta_{Gaia}(t_k)$ is the projection of the two-dimensional path of the source $\mathbf{S}(t_k)$ on Gaia's along-scan axis. Diagonal elements of the matrix $\sqrt{c_{ii}}$ are the individual uncertainties in the parameters $a_i$ assuming the standard $\chi^2$ fitting procedure. The uncertainty introduced above is a simple estimator of the width of the posterior probability distribution of the model parameters (Sivia 1996, Saha 2003). Note, that it is only valid when the posterior distribution is sufficiently narrow that we can approximate the signal by its linear expansion around true value of $a$. Here, $a_1, \ldots, a_{11}$ are the 11 parameters stated above and $\sigma_{\rm a}$ is the astrometric accuracy for a given star, which depends on the source magnitude and is recorded in Table 6.1.

Note that $t_k$ are the times at which Gaia samples the one-dimensional astrometry data-stream. In our calculations, these times are always generated from Gaia's scanning law using Lindegren's software. Gaia's scanning law is quite complicated, as shown in Figure 6.6. The number of times Gaia samples an object $N$ is between 50 and 200, depending on its ecliptic latitude (Lindegren 1998). The number of transits is greatest, and so the final astrometry is most accurate, for objects close to an ecliptic latitude $\sim 40°$. For a typical location, the number of transits is between 50 and 100. These transits are usually clustered into groups of between 2 and 5, so the average effective number of independent datapoints is $\sim 30$. To incorporate Gaia's photometry eq. 6.22 becomes

$$b_{ij} = \sum_{k=1}^{N} \left( \sigma_{\rm a}^{-2} \, \frac{\partial \theta_{Gaia}(t_k)}{\partial a_i} \frac{\partial \theta_{Gaia}(t_k)}{\partial a_j} + \sigma_{\rm F}^{-2} \, \frac{\partial F_{Gaia}(t_k)}{\partial a_i} \frac{\partial F_{Gaia}(t_k)}{\partial a_j} \right), \tag{6.23}$$

where $F_{Gaia} = F^0_{Gaia} A_{Gaia}$ is the flux observed from Gaia and $F^0_{Gaia}$ is the $12^{th}$ model parameter corresponding to the baseline flux. For a given $\sigma_{\rm p}$, the accuracy in flux measurement is fixed to $\sigma_{\rm F} = F^0_{Gaia}(10^{0.4\sigma_{\rm p}} - 1)$. When photometric data is also available from the ground-based observations

$$b_{ij} \rightarrow b_{ij} + \sum \sigma_{\oplus}^{-2} \, \frac{\partial F_{\oplus}(t_{\oplus})}{\partial a_i} \frac{\partial F_{\oplus}(t_{\oplus})}{\partial a_j} \tag{6.24}$$

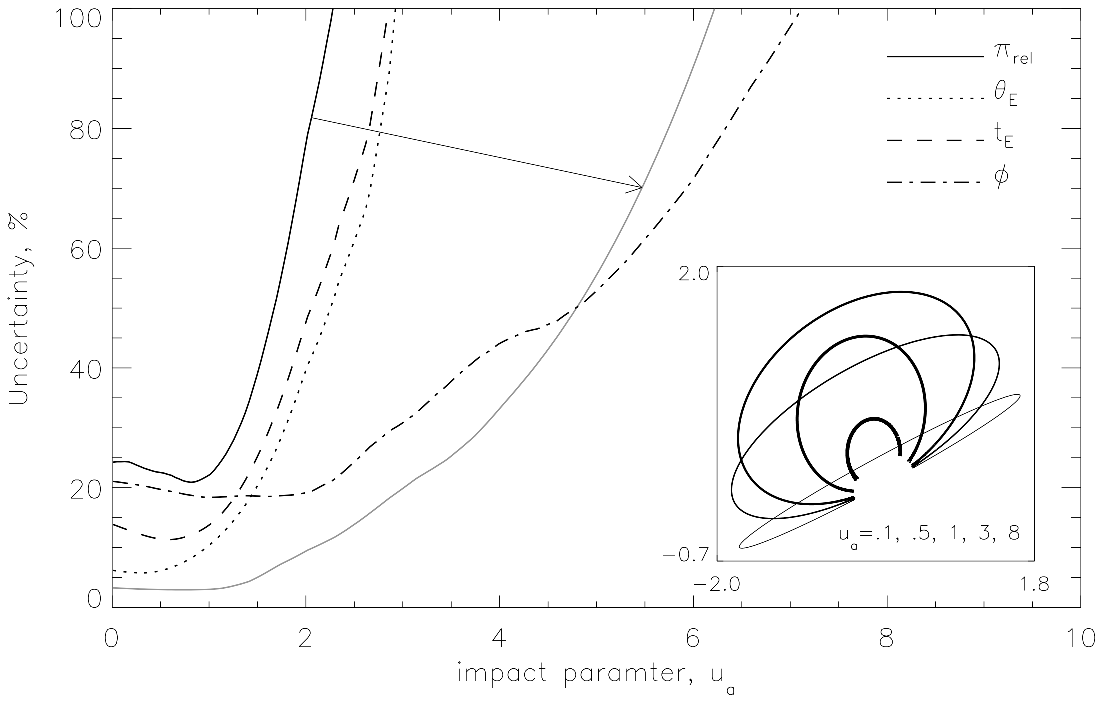


Figure 6.11: This shows the percentage error in estimation of the microlensing parameters as a function of impact parameter $u_0$. Accurate recovery of the relative parallax $\pi_{\rm rel}$ is hard, whereas recovery of the angular Einstein radius $\theta_{\rm E}$ and the Einstein crossing time $t_{\rm E}$ is easier. (The lens distance is 150 pc, the source distance is 4 kpc, the transverse velocity is 20 $\rm km\,s^{-1}$, while the accuracy is 150 $\mu$as.)

where $F_\oplus$ is the flux measured from the ground at times $t_\oplus$. In all the calculations reported below, we set $A_\oplus = A_{Gaia}$ and $F^0_\oplus = F^0_{Gaia}$.

### 6.3.2 Errors in estimates of the astrometric microlensing parameters

Although the relative parallax $\pi_{\rm rel}$ is quite hard to estimate, it is valuable since it provides a unique solution for the mass of the lens $M$ when combined with $\theta_{\rm E}$ (see eq. (6.4)). If in addition the source distance $D_{\rm s}$ can be estimated – for example, if Gaia itself measures the source parallax – then we have a complete solution for all the microlensing parameters. Let us recall that in the ground-based MACHO, EROS and OGLE pro-

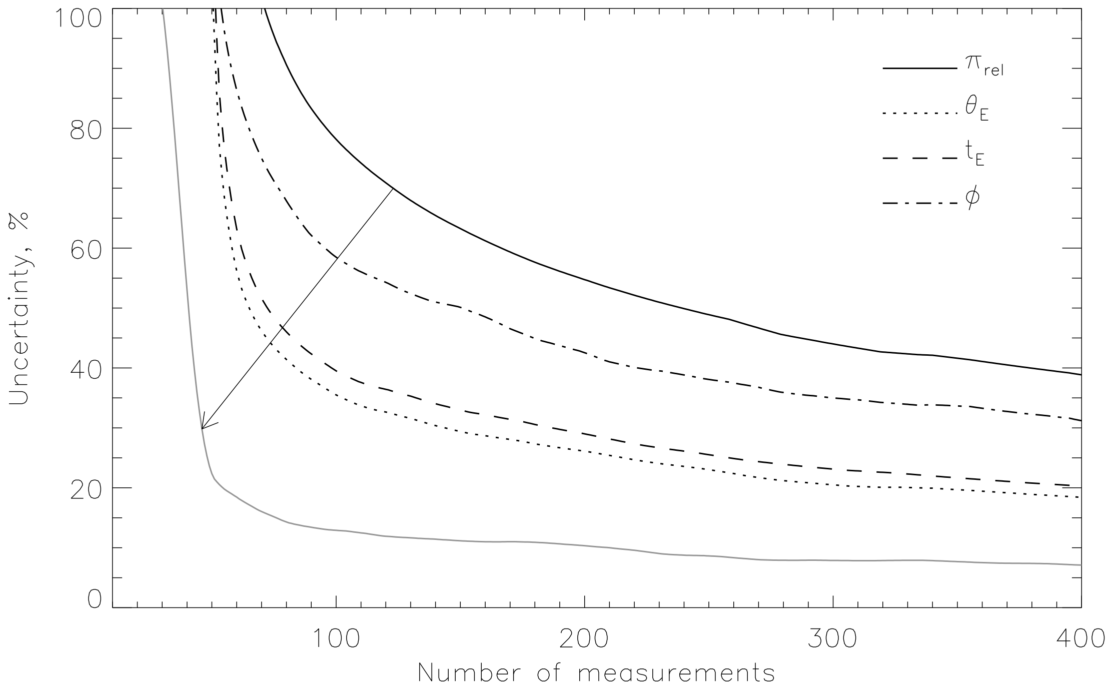


Figure 6.12: This shows the percentage error as a function of number of datapoints for a typical microlensing event. Provided there are $\gtrsim 100$ measurements, then the sampling is not the critical factor. (The lens distance is 150 pc, the source distance is 4 kpc, the transverse velocity is 40 $\mathrm{km\,s^{-1}}$, while the accuracy is 230 $\mu$as.)

grams, there is not a single microlensing event for which the parameters can be derived unambiguously from the data alone. Consequently, the location of the lenses responsible for the events towards the Magellanic Clouds is a matter of considerable controversy (e.g., Sahu 1994, Gould 1995, Alcock et al. 1997, Evans & Kerins 2000, Zhao & Evans 2000). Gaia offers the promise of providing a sample of lensing events for which all the parameters can be extracted without any modeling assumptions. However, some caution is needed, as we already known in the context of the *Space Interferometry Mission* (SIM) by Gould & Salim (1999) that astrometric measurements alone do not necessarily guarantee accurate estimation of the relative parallax. For which events can we recover the relative parallax to good accuracy from the Gaia data? First of all, an event must last an adequate time for the microlensing shift to be distorted by parallactic movement of the lens. Thus, the error will depend on the duration of the astrometric event. Second, the amplitude of the distortion is dictated by the Einstein radius projected onto the observer plane (e.g., Gould & Salim 1999, Gould 2000), namely

$$\tilde{r}_{\mathrm{E}} = \frac{\theta_{\mathrm{E}}}{\pi_{\mathrm{rel}}}. \tag{6.25}$$

For close lenses ($D_{\mathrm{l}} \approx 100$ pc), it follows that $1 - D_{\mathrm{l}}/D_{\mathrm{s}} \to 1$, and so the projected Einstein radius becomes

$$\tilde{r}_{\mathrm{E}} \approx r_{\mathrm{E}} \approx 1\mathrm{AU}\sqrt{\frac{\mathrm{M}}{\mathrm{M}_{\odot}}}\sqrt{\frac{\mathrm{D_l}}{100\ \mathrm{pc}}}. \tag{6.26}$$

For a measurable distortion, we require $\tilde{r}_{\mathrm{E}}$ to be about an astronomical unit. If it is too large, then the Earth's motion about the Sun has a negligible effect. Accuracy in the relative parallax is a trade-off between duration and lens distance.

Figure 6.9 shows the uncertainty in $\pi_{\mathrm{rel}}$ as a function of $\tilde{r}_{\mathrm{E}}$ for different Einstein crossing times $t_{\mathrm{E}}$, while the companion Figure 6.10 shows the uncertainty in $\pi_{\mathrm{rel}}$ as a function $\theta_{\mathrm{E}}$ for different astrometric accuracies. It aids accurate recovery of the relative parallax if the angular Einstein radius is large. Note, that astrometric event duration is $\sim t_{\mathrm{E}}\theta_{\mathrm{E}}$ which is illustrated in the inset of Figure 6.9. The error in $\pi_{\mathrm{rel}}$ degrades for distant lenses. The degradation is worse for the shorter duration events. Note that the close lenses ($D_{\mathrm{l}} \approx 100$ pc) typically have a crossing time $t_{\mathrm{E}} \approx 1\mathrm{AU}/50\ \mathrm{kms}^{-1} \approx 30$ days, and so the astrometric event duration is typically 450 days. It is the close lenses with longer timescales that provide the most propitious circumstances for measuring $\pi_{\mathrm{rel}}$ from the data. In each case, the thick grey curve shows the considerable improvement when photometric data is available from the ground-based follow-up observations.

Figure 6.11 shows the uncertainties in $\theta_{\mathrm{E}}, t_{\mathrm{E}}, \pi_{\mathrm{rel}}$ and $\phi$ as a function of the dimensionless impact parameter. A typical value of $u_0$ for Gaia is 2 or so. For large $u_0$, the parallactic distortion is superposed upon a small eccentricity ellipse (see eq. (6.11)).

For small $u_0$, the eccentricity of the ellipse becomes large and the parallactic distortion makes the curve thinner and more elongated, as illustrated in the inset to Figure 6.11. This can be an almost degenerate situation for estimating the microlensing parameters from one-dimensional astrometry. For typical impact parameters, the percentage error in $\phi$ and $\pi_{\rm rel}$ is larger than the error in $\theta_{\rm E}$ and $t_{\rm E}$. This is because $\pi_{\rm rel}$ controls the shape of the astrometric curve, $\phi$ controls the orientation, while $\theta_{\rm E}$ and $t_{\rm E}$ the size. Given one-dimensional astrometry, it is more difficult to recover the details of the shape than the size. Asymptotically, the percentage error always increases with increasing impact parameter. However, there is a régime at small impact parameter when the converse is true. The reason for this is as follows. For very close lenses, the parallactic distortion can become so large that the direction of traversal of the astrometric curve is reversed. This degeneracy is inherent in microlensing and it is not a consequence of the limited information that can be extracted from measurements. The astrometric curve can now correspond to events with positive impact parameter and large parallactic effect, or negative impact parameter and small parallactic effect. There is no way to tell the difference.

Finally, Figure 6.12 shows the effects of sampling. The error in selected microlensing parameters is plotted against the number of datapoints for a typical microlensing event. In this Figure only, the sampling is not performed according to Gaia's sampling law, but the datapoints are chosen uniformly over the mission lifetime, as we wish to illustrate the importance of sampling. In fact, Gaia samples every object between 100 and 200 times depending on ecliptic latitude. So, at first glance, Figure 6.12 seems to offer reassurance that sampling is not a critical factor, as it shows that the error increases swiftly only once the effective number of datapoints falls below 50. However, this is misleading because Gaia's datapoints are clustered into groups of between 2 and 5, or typically 4. This is disadvantageous, as it reduces the effective number of datapoints by $\sim 4$, although the accuracy of the astrometry is improved by $\sim 2$. Figure 6.12 tells us that if the number of independent datapoints falls below $\sim 50$, then sampling is the limiting factor in the extraction of useful parameters.

### 6.3.3 Errors in estimates of masses of lenses

We are primarily interested in finding the masses of the lenses. The error in the mass is related to the errors in the angular Einstein radius and the relative parallax by

$$\left(\frac{\sigma_M}{M}\right)^2 = 4\frac{\sigma^2_{\theta_{\rm E}}}{\theta^2_{\rm E}} + \frac{\sigma^2_{\pi_{\rm rel}}}{\pi_{\rm rel}} - 4\hat{C}(\theta_{\rm E}, \pi_{\rm rel})\frac{\sigma_{\theta_{\rm E}}}{\theta_{\rm E}}\frac{\sigma_{\pi_{\rm rel}}}{\pi_{\rm rel}}, \tag{6.27}$$

where $\hat{C}$ is the correlation coefficient between $\theta_{\rm E}$ and $\pi_{\rm rel}$. Let us recall that the elements of the correlation matrix are customarily defined as

$$\hat{C}(i,j) = \frac{C_{ij}}{\sqrt{C_{ii}C_{jj}}}. \tag{6.28}$$

The cross-term is important because errors in $\theta_{\rm E}$ and $\pi_{\rm rel}$ are strongly correlated for most of the events. This is a small term for low impact parameter events, but it becomes important once $u_{\rm a} > 2$. The cross-term always decreases the uncertainty in the mass. This is why Boden et al. (1998) found that eq. (14) of their paper (which neglects the correlation) tends to overestimate the mass error. We always use the full formula (6.27) to compute the uncertainty in the mass in our simulations.

## 6.4 A model of the Galaxy

The goal of the analysis of the microlensing events seen by Gaia is to infer properties of the lenses. The likely results can best be judged by Monte Carlo simulations. Before this, we need to develop a model of the lens and source populations in the Galaxy. This section describes the ingredients of the model in turn.

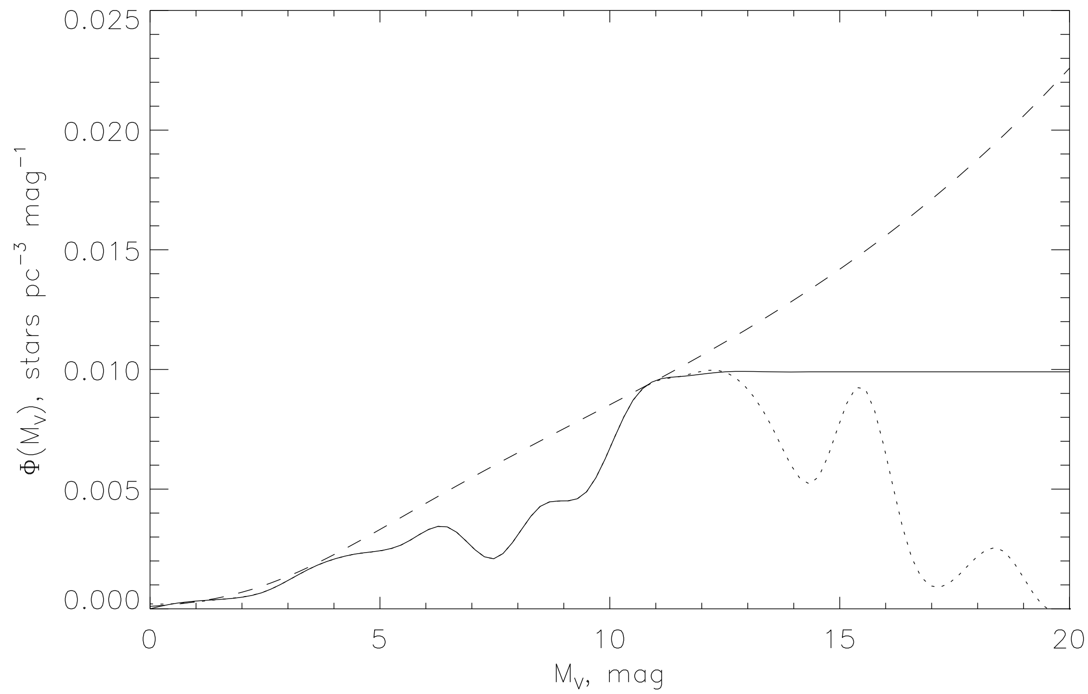


Figure 6.13: This shows three luminosity functions, namely the Bahcall-Soneira (dashed line), the Reid-Hawley (dotted line) and the flat model (full line). The flat model is the standard one in our simulations.

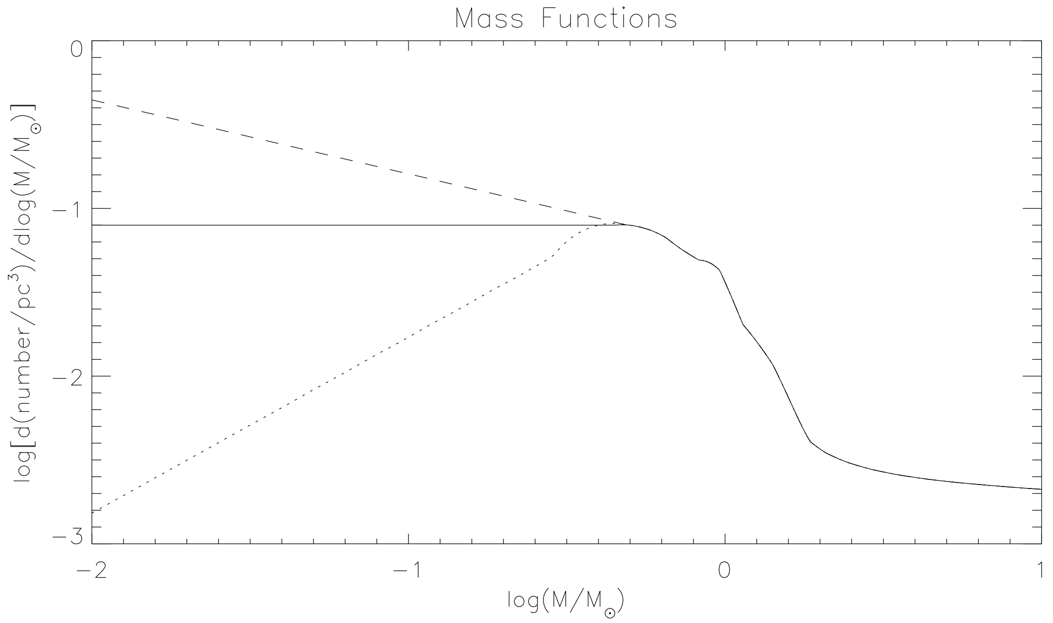


Figure 6.14: This shows three mass functions that are flat, rising and falling below $0.5M_\odot$. Above $0.5M_\odot$, the mass function is derived from the Reid-Hawley LF. Below $0.5M_\odot$, the mass function cannot be derived with certainty from the observations.

### 6.4.1 Luminosity function of sources

Let the mass density of sources be $\rho$ and the luminosity function (LF) be $\phi$. In an element of solid angle $d\Omega$, the number of stars in a direction $(\ell, b)$ with distances between $D_\mathrm{s}$ and $D_\mathrm{s} + dD_\mathrm{s}$ and with magnitudes between $m_\mathrm{G}$ and $m_\mathrm{G} + dm_\mathrm{G}$ is

$$dN = \frac{1}{\rho_0}\phi(M_G) dm_\mathrm{G} \rho(\ell, b, D_\mathrm{s}) D_\mathrm{s}^2 dD_\mathrm{s} d\Omega. \tag{6.29}$$

Here, $\ell$ and $b$ are Galactic coordinates, so that the solid angle $d\Omega$ is just $\cos b\, d\ell db$ and $\rho_0$ is the local mass density. As usual, absolute magnitude $M_G$ is related to apparent magnitude $m_\mathrm{G}$ and extinction via

$$M_G = m_\mathrm{G} - 5\log D_\mathrm{s} - A(D_\mathrm{s}, \ell, b) + 5, \tag{6.30}$$

where $A(D_\mathrm{s}, \ell, b)$ is the extinction law. Equation (6.29) combined with Equation (6.14) can be interpreted as a probability density for the source parameters $D_\mathrm{s}, \ell, b$ and $M_G$.

Three source LFs are shown in Figure 6.13. These are valid for the $V$ band, whereas Gaia's photometry is most accurate in the broad $G$ band. As our aim is to provide approximate numbers in our calculations, the conversion from $V$ to $G$ band in the LF will not have a noticeable effect on the results.

The Bahcall-Soneira (1980) LF is a reasonably accurate predictor of the numbers of stars in the Galaxy fainter than $G \sim 15$. The Reid-Hawley LF (2000) is derived from a combination of sources, including the *Third Catalogue of Nearby Stars*, the *8 Parsec Sample*, as well as *Hipparcos* data. It is the local LF for the stellar disk, but it may suffer from incompleteness at magnitudes fainter than $G \sim 16$. Accordingly, our standard assumption is that the LF is flat in the magnitude range $10 < M_G < 20$ and follows the Reid-Hawley LF when $M_G < 10$. In this case, the normalization is chosen to be the maximum value of the stellar luminosity function of the Galactic disk as recorded in Table 7.3 of Reid & Hawley (2000). The total number of stars in the range $10 < G < 20$ in each of the three models is $\sim 0.9 - 1.1 \times 10^9$. The microlensing results reported in this Chapter are always calculated assuming our standard LF.

### 6.4.2 Extinction

We use the extinction law of Drimmel & Spergel (2001), the source code of which is freely available on the web. In the resulting Galaxy model, the total number of stars with magnitudes satisfying $10 \lesssim G \lesssim 20$ is $\sim 10^9$, for which there is good evidence from starcounts (Table 4.2 of Mihalas & Binney 1981).

In the Monte Carlo simulations, once the source distance, direction and absolute magnitude are chosen, then the extinction law is used to work out the apparent magnitude. We calculate the astrometric accuracy $\sigma_{\rm a}$ for a given source magnitude using the accuracy-magnitude relation for Gaia, listed in Table 6.1.

### 6.4.3 Density of sources

The density of sources at a distance $D_{\rm s}$ in the direction of Galactic longitude $\ell$ and latitude $b$ is

$$\rho = \rho_{\rm d} + \rho_{\rm b}. \tag{6.31}$$

Here, $\rho_{\rm d}$ is the density distribution of the Galactic disk and $\rho_{\rm b}$ is the density of the Galactic bulge. We use an exponential disk model with scale-length $R_{\rm d} \sim 3$ kpc and scale-height $z_{\rm h} \sim 350$ pc (Gould, Bahcall & Flynn 1997), namely

$$\rho_{\rm d} = \rho_0 \exp\left(-(R - R_0)/R_{\rm d} - |z|/z_{\rm h}\right), \tag{6.32}$$

where $R$ is Galactocentric distance, $z$ is the height above or below the Galactic plane, $R_0$ is the radial position of the Sun and $\rho_0$ is the local density of disk stars, which is taken as $0.10 M_\odot$ pc$^{-3}$ (Holmberg & Flynn 2000). It is straightforward to establish that

$$R^2 = R_0^2 + D_\mathrm{s}^2 \cos^2 b - 2 D_\mathrm{s} R_0 \cos b \cos \ell, \quad z = D_s \sin b. \tag{6.33}$$

We use the oblate axisymmetric bulge model provided by Kent (1992)

$$\rho_\mathrm{b}(R,z) = 3.53\, K_0 \left( \frac{s}{667 \text{ pc}} \right) M_\odot \text{ pc}^{-3}, \tag{6.34}$$

where $s^4 = R^4 + (z/0.61)^4$ and $K_0$ is a modified Bessel function. Kent's model is a reasonable fit to the Spacelab infrared data. However, it is known to be wrong in detail as the Galactic bulge is really a triaxial bar (e.g., Binney et al. 1991; Häfner et al. 2000). This means that our model – like any axisymmetric model – will underestimate the photometric optical depth as compared to the observations in windows close to the Galactic Centre typically by a factor 2 or so (see e.g., Evans 1994, 1995; Binney 2000).

### 6.4.4 Mass function and density of lenses

In our Monte Carlo simulations, both the disk and the bulge stars act as lenses. Halo populations of dark objects like Machos are not included. So, the density of lenses is prescribed by eq (6.32) and eq (6.34). We generate the masses of the lenses using the composite mass function shown in Figure 6.14. Above $0.5 M_\odot$, we use a mass function (MF) derived from the Reid-Hawley LF via

$$f(M) = \phi(M_G(M)) \frac{dM_G}{dM}, \tag{6.35}$$

Here, $M_G(M)$ is the relationship between mass and absolute magnitude, as recorded in Kroupa, Tout & Gilmore (1990). This ensures that the high-mass end of the MF (which gives most of the light) is compatible with the local LF. The low-mass end of the MF is not at all certain and its derivation from the LF is fraught with difficulties (e.g., D'Antona & Mazzitelli 1994). Hence, for masses below $0.5M_\odot$, we assume that the MF is flat in our standard model.

### 6.4.5 Velocity distributions

We draw components of source and lens velocities from triaxial Gaussian distributions:

$$\begin{aligned} f(V_R, V_z, V_\phi) &= \frac{1}{(2\pi)^{3/2}\sigma_R\sigma_\phi\sigma_z} \\ &\times \exp(-\frac{V_R^2}{2\sigma_R^2} - \frac{(V_\phi - v_\mathrm{m})^2}{2\sigma_\phi^2} - \frac{V_z^2}{2\sigma_z^2}) \end{aligned} \tag{6.36}$$

For the bulge sources, the random velocity is $\sigma_R = \sigma_\phi = \sigma_z = 100\,\mathrm{km\,s^{-1}}$ about a mean of $50\,\mathrm{km\,s^{-1}}$ (McGinn et al. 1989). For the disk sources, the random component has $\sigma_R = 34\,\mathrm{km\,s^{-1}}$ $\sigma_\phi = 21\,\mathrm{km\,s^{-1}}$ $\sigma_z = 18\,\mathrm{km\,s^{-1}}$ about a mean velocity $v_\mathrm{m}$ of $214\,\mathrm{km\,s^{-1}}$ (Edvardsson et al. 1993). The assumption of triaxial Gaussians with constant semiaxes seems reasonable and is often made in studies of Galactic microlensing (e.g., Kiraga & Paczyński 1994, Kerins et al. 2001). Nonetheless, a more exact calculation should derive the spatial variation in the means and dispersions of the velocities of the stellar populations by solving the Jeans equations. The velocity of the Sun has the following components: $v_{\odot R} = -10\,\mathrm{km\,s^{-1}}$, $v_{\odot\phi} = 219.25\,\mathrm{km\,s^{-1}}$ and $v_{\odot z} = 7.17\,\mathrm{km\,s^{-1}}$ (Dehnen & Binney 1998).

| | A | A+Ph | A+Ph+$\oplus$ |
|---|---|---|---|
| $N(\sigma_M < 50\%)$ | 0.2 % | 3.3 % | 6.6 % |
| $N(\sigma_{t_E} < 50\%)$ | 0.4 % | 34 % | 49 % |
| $N(\sigma_{\theta_E} < 50\%)$ | 0.6 % | 10 % | 11 % |
| $N(\sigma_{\pi_{rel}} < 50\%)$ | 0.2 % | 3.3 % | 6.4 % |
| $N(\sigma_\phi < 50\%)$ | 2.3 % | 16 % | 26 % |
| $N(\sigma_{u_0} < 50\%)$ | 0.05 % | 26 % | 38 % |

Table 6.2: This gives the percentage of events in the whole sample with an error of less than 50% in the estimate of mass $M$, or the Einstein crossing time $t_E$, or the angular Einstein radius $\theta_E$ or the relative parallax $\pi_{rel}$, or the proper motion angle $\phi$, or the impact parameter $u_0$. Columns headed with A, A+Ph and A+Ph+$\oplus$ correspond to different observing strategies, namely Gaia astrometry alone; Gaia astrometry and photometry; Gaia astrometry and photometry plus ground-based photometry.

## 6.5 Monte Carlo simulations

We first pick the source position, velocity and magnitude, which provides the astrometric accuracy. This is done by drawing randomly from the probability distributions implied by eqs. (6.14), (6.29) and (6.36), using the rejection method (e.g., Press et al. 1992). The astrometric optical depth (6.14) can be recast to provide the joint probability of drawing the lens distance and transverse velocity for a given source. We draw the mass of the lens from the mass function. Finally, we pick the impact parameter $u_0$ and the phase $t_0$ by drawing uniformly from the rectangular area in the lens plane of size $T_{life}v$ and $2u_a r_E$ (illustrated in Figure 2 of Dominik & Sahu (2000)). This provides us with a single simulated microlensing event, which has a variation of the centroid shift at least as large as $5\sqrt{2}\sigma_a$ and which has a maximum during the lifetime of the Gaia mission. We can envisage three different observing strategies. The first strategy uses Gaia astrometry alone (labelled as A), the second Gaia astrometry and photometry together (labelled as A+Ph). We can also consider the inclusion of additional ground-based photometry. In the third strategy, once Gaia detects more than $3\sigma_p$ amplification from the baseline, we assume that a ground-based telescope starts following the event and delivers hourly photometry with an accuracy $\sigma_p$ (labelled as A+Ph+$\oplus$).

| Parameter | Whole Sample | High Quality Sample |
|---|---|---|
| $t_{\rm ae}$ (days) | 9 (500) | 240 (1175) |
| $\theta_{\rm E}$ (mas) | 0.6 (1.2) | 2.6 (3.6) |
| $\tilde{r}_{\rm E}$ (au) | 9.1 (14.4) | 7.4 (11.4) |
| $\pi_{\rm rel}$ (mas) | 0.06 (1.3) | 0.33 (3) |
| $\lvert u_0 \rvert$ | 1.2 (1.7) | 0.99 (1.2) |
| $D_{\rm l}$ (kpc) | 5.7 (5.2) | 2.4 (2.8) |
| $D_{\rm s}$ (kpc) | 8.6 (8.3) | 7.4 (6.9) |
| $v$ ( $\rm km\,s^{-1}$) | 145 (154) | 50 (66) |
| $\sigma_{\rm a}$ ($\mu$as) | 695 (734) | 466 (540) |
| $G$ magnitude | 19.0 (19.1) | 18.4 (18.6) |

Table 6.3: This records the median and the mean (in brackets) values of the parameters of the simulated events for the whole sample and for the subset of high quality events (those with mass uncertainty less than 50%).

### 6.5.1 Distributions of the events

We create a set of 15000 such microlensing events, as a synthetic Gaia database. For each member of the sample, we compute the error in the estimated mass of the lens using eq (6.27), which of course depends on the uncertainties in the relative parallax and the angular Einstein radius. This is done for each of the three observing strategies. From this, we build up subsets of events for which the error in the inferred mass is less than 50%. The number of high quality events for each strategy is listed in Table 6.2. We choose the subset with the largest number of lens masses recovered. This corresponds to the set of events that were followed up by the ground-based telescopes (Strategy 3). We refer to this as the sample of high quality events. Figures 6.15 and 6.16 show the distributions of the microlensing parameters for the entire sample and for the subset of high quality events. The medians and means of the distributions are given in Table 6.3.

There are a number of interesting things to notice. The mean source distance is $\sim 8.5$ kpc for the whole sample, and about 7.5 kpc for the high quality events (Figure 6.15). The mean lens distances are still smaller: 6 kpc for the whole sample and 2 kpc for the high quality events. So, the astrometric microlensing signal seen by Gaia is dominated

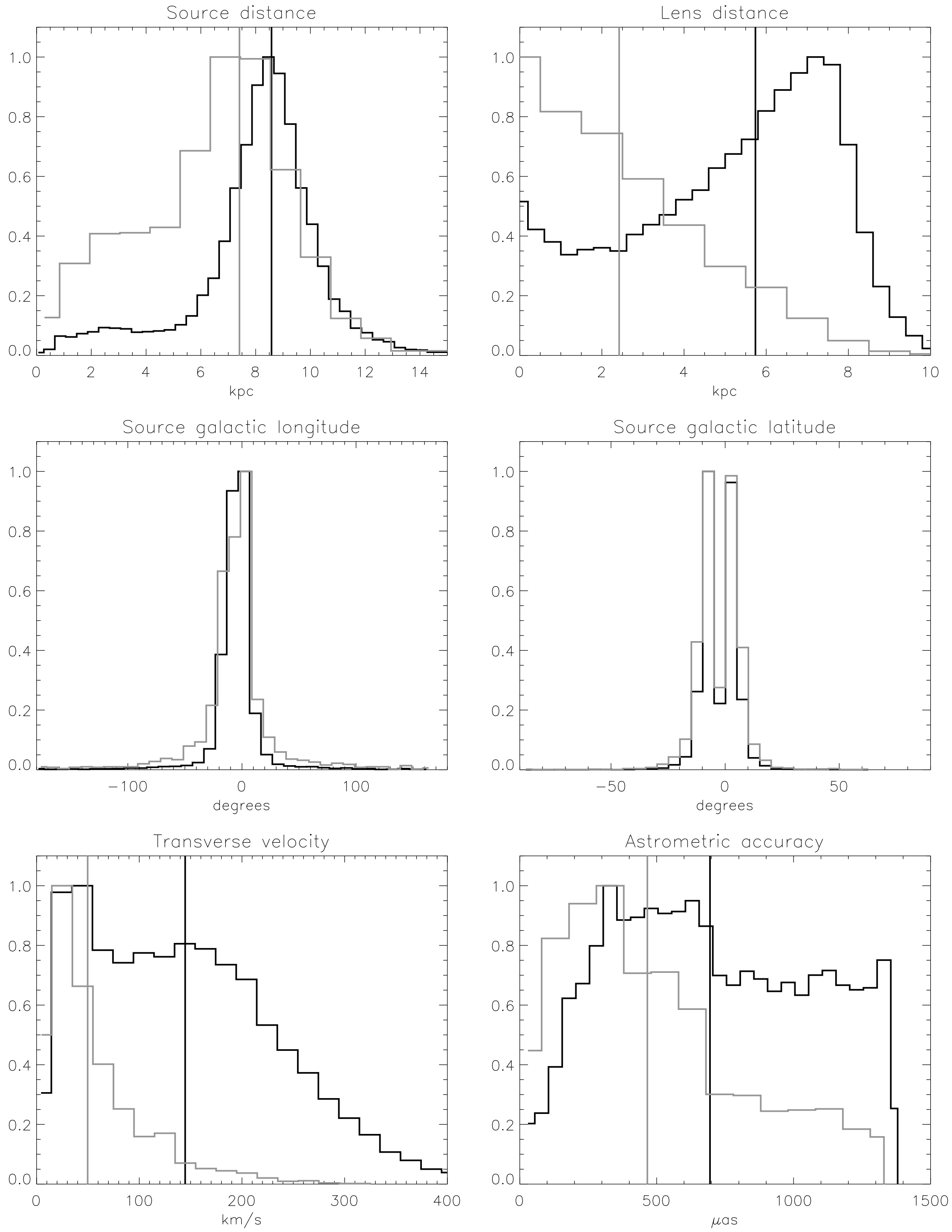


Figure 6.15: Distributions of source distance $D_s$, lens distance $D_l$, source coordinates $(\ell, b)$, transverse velocity $v$ and astrometric accuracy $\sigma_a$ for the simulated datasets. The histogram in black lines refers to the whole sample, grey lines to the sub-sample of high quality events. The distributions are all normalized to a maximum value of unity. The medians are indicated by vertical bars.

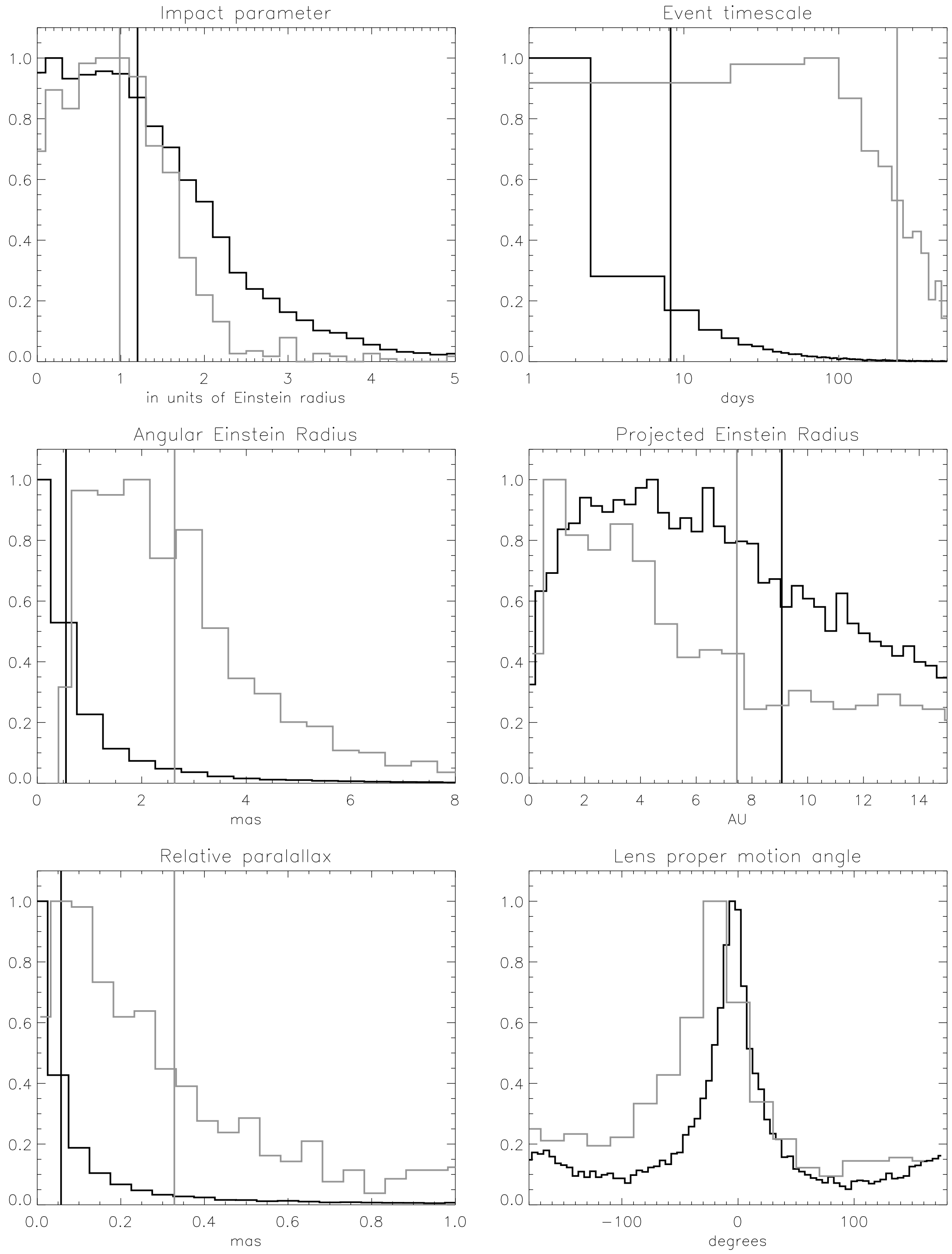


Figure 6.16: Distributions of impact parameter $u_0$, event duration $t_{\rm ae}$, angular Einstein radius $\theta_{\rm E}$, projected Einstein radius $\tilde{r}_{\rm E}$, relative parallax $\pi_{\rm rel}$ and lens proper motion angle $\phi$ for the simulated datasets. The histogram in black lines refers to the whole sample, grey lines to the sub-sample of high quality events. The distributions are all normalized to a maximum value of unity. The medians are indicated by vertical bars.

by the local stars. Of course, more distant microlensing events take place, but they can be much less commonly identified and still less commonly analyzed to extract the parameters for the event. For the whole sample, the optimum direction is towards the Galactic Centre. This is not surprising, as the source and lens density is highest in this direction. The distribution of lens distance for the whole sample is approximately bimodal. This is because the probability is $\propto v^{3/2}\sqrt{1-D_\mathrm{l}/D_\mathrm{s}}$. For lenses in the disk, the first factor increases with increasing $D_\mathrm{l}$, whilst the second factor decreases. For high quality events, no such bimodality is evident, as the lenses must be very close.

There are two ways to obtain a high quality event. Either the astrometric accuracy is good (e.g. lower right panel of Figure 6.15) or the microlensing event has optimum characteristics, namely that the angular Einstein radius is large, the duration is long and the projected Einstein radius $\tilde{r}_\mathrm{E}$ is comparable to the size of the Earth's orbit around the Sun. All these characteristics are evident on comparing the full and the dashed histograms in Figure 6.16. The median duration of the high quality events is $\sim$ 240 days, nearly a factor 30 times larger than the whole sample. The projected Einstein radius $\tilde{r}_\mathrm{E}$ has a median of 9 au for the whole sample, and it is smaller at 7 au for the high quality events. Note, that the distribution of $\tilde{r}_\mathrm{E}$ peaks at 1 au for the events with the lens masses measured. The median angular Einstein radius is nearly a factor of 4 larger for the high quality events. The lower right panel of Figure 6.16 shows the distribution of the lens proper motion angle with respect to the direction of Galactic rotation. While for the whole sample this distribution is symmetric, there is a noticeable selection effect for the high quality events. The motion of the satellite around the Sun affects the relative source-lens trajectory for a longer period of time if the lens proper motion angle is parallel to the ecliptic plane. Table 6.2 shows the percentage of events for which $M, t_\mathrm{E}, \theta_\mathrm{E}$, $\pi_\mathrm{rel}$, $\phi$ and $u_0$ can be recovered to within 50% for all four strategies. From the table, we see that Gaia will determine masses of $\sim$ 500 objects with an accuracy greater than 50%. Photometric measurements performed by Gaia play an

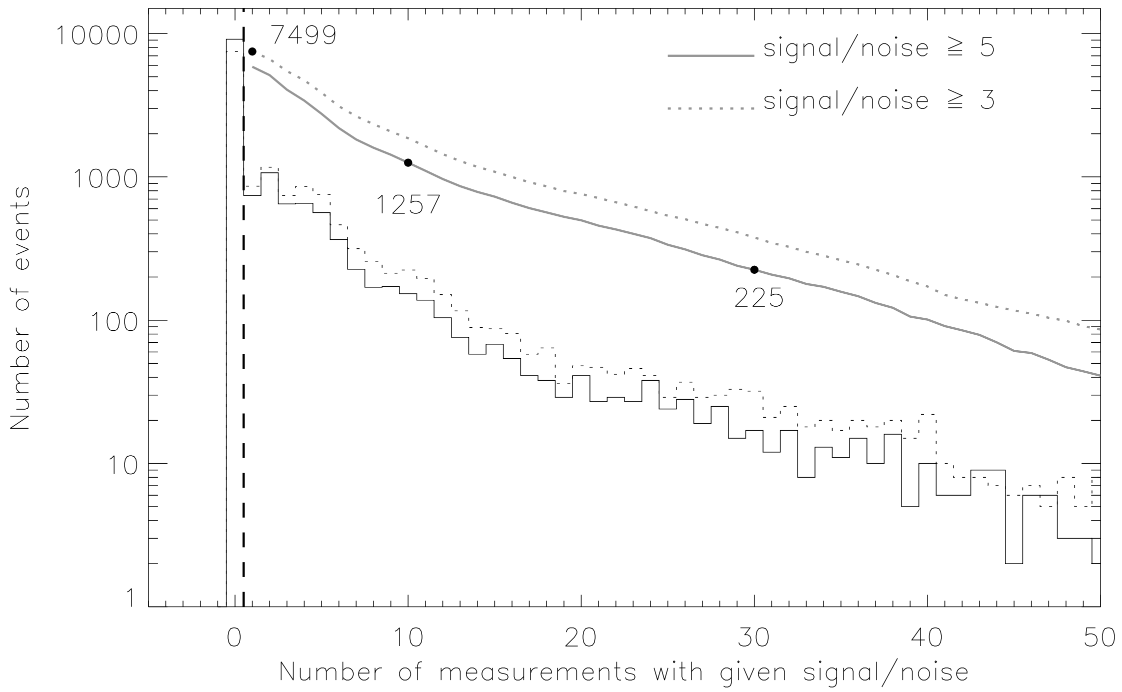


Figure 6.17: This shows distributions of the number of Gaia's photometric measurements (per event) with signal-to-noise ratio greater than certain threshold. The two histograms correspond to signal-to-noise ratio of 5 (solid) and 3 (dotted). The dashed line marks the boundary beyond which at least one datapoint is recorded by Gaia. Integrated distributions are shown as grey lines above the histograms.

important role in the recovery of microlensing parameters. Let us recall, that astrometry can provide direct estimates of the angular Einstein radius $\theta_{\rm E}$ and the lens proper motion angle $\phi$. However, values of impact parameter $u_0$ and Einstein crossing time $t_{\rm E}$ are more difficult to obtain with astrometry alone (Strategy 1). On the other hand, just a few datapoints on the lightcurve of a microlensed star will allow the timescale $t_{\rm E}$ and the maximum amplification (and hence $u_0$) to be determined (Strategy 2). A further increase in the number of mass measurements is possible if ground-base photometry is supplied. In our model the quality of the photometric follow-up measurements is comparable to that from Gaia, but the temporal sampling is much denser. The dedicated ground-based telescopes will help to bring the total number of masses recovered to $\sim 1000$ (Strategy 3). Let us emphasize that, although, accurate and well-sampled photometry aids parameter recovery, the complete microlensing solution requires the knowledge of $\theta_{\mathrm{E}}$ and $\phi$ that come only from astrometric data. Note, that over 30% of all the events will have good estimates for $t_{\mathrm{E}}$ and of order of 10% for $\theta_{\mathrm{E}}$ from the Gaia measurements alone. Current ground-based programs like MACHO and EROS attempt to recover the characteristic masses of lenses from estimates of $t_{\mathrm{E}}$ alone for samples of a few tens to hundreds of events. By contrast, Gaia will provide a much larger dataset of $> 1500$ microlensing events with good estimates of both $t_{\mathrm{E}}$ and $\theta_{\mathrm{E}}$. The typical locations and velocities of the sources and lenses can be inferred for the ensemble using statistical techniques based on Galactic models (in much the same manner as MACHO and EROS do at present).

Figure 6.17 shows the distribution of the number of photometric measurements with a certain signal-to-noise ratio in Gaia's data-stream. We require $\geq 3\sigma_{\mathrm{p}}$ deviation in flux during the microlensing event for Gaia to issue an alert for ground-based follow-up observations of the star. From Figure 6.17 it follows that $\sim 7500$ (i.e. 50% of the whole dataset) astrometric events can in principle be followed-up from the ground (please note, that this number will be still lower if we want Gaia to see an event in photometry before maximum). This number can be read off the plot as it gives the integrated distributions as well as the histograms. Events with an amplification $A_{Gaia}$ corresponding to $5\sigma_{\mathrm{p}}$ can be detected and analyzed without any help from the ground provided there are enough measurements recorded by Gaia. The total number of events with at least one datapoint at $5\sigma_{\mathrm{p}}$ excursion caused by microlensing is 5870. It means that a maximum of 40% of all events will be measured simultaneously in photometry by Gaia. However, if only a few measurements are enough to put constraints on the value of $t_{\mathrm{E}}$, many more datapoints are needed to measure the projected Einstein radius $\tilde{r}_{\mathrm{E}}$. Only 8.3% of all the 15000 events have 10 datapoints during during the source brightening. These may very well be clustered, so there may be only 3 or so independent measurements.

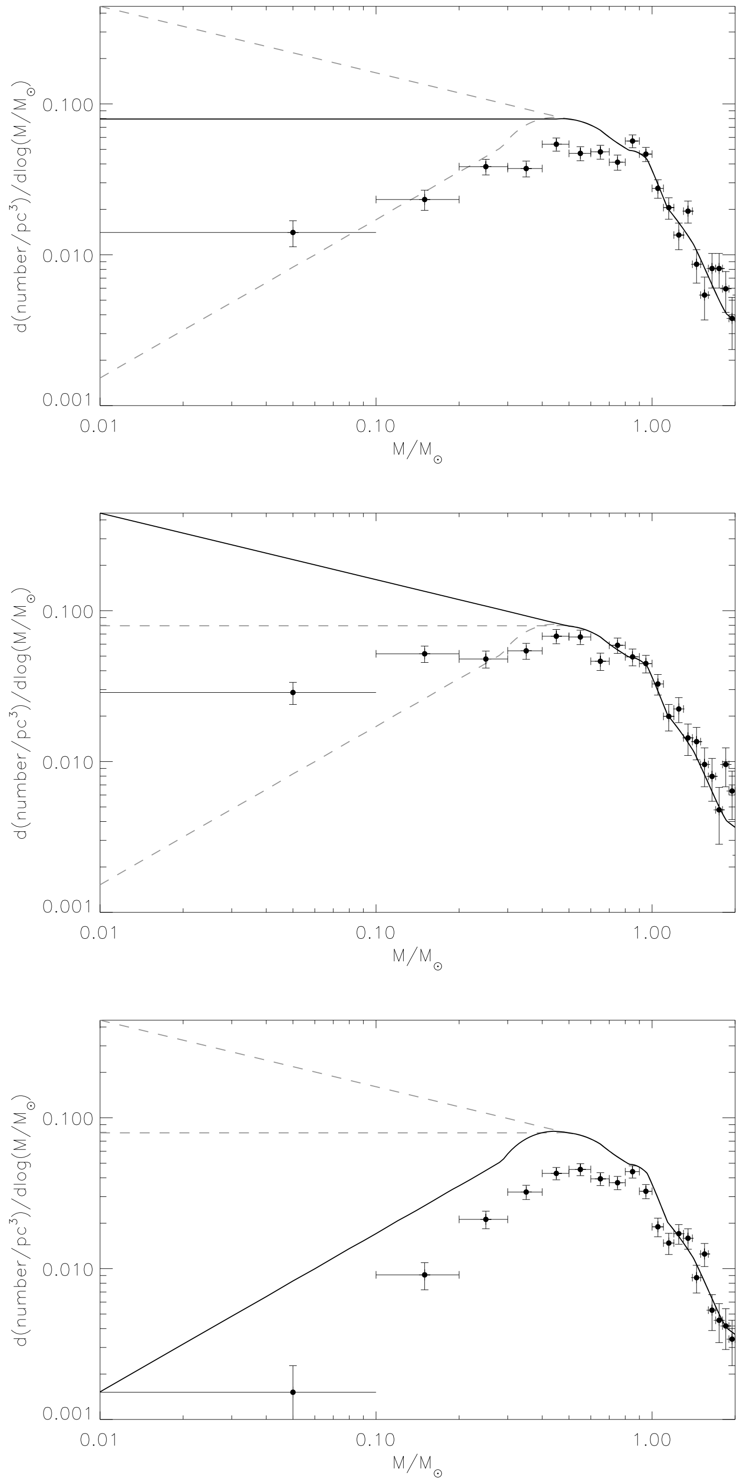


Figure 6.18: The recovery of the flat, rising and falling mass functions from the subsamples of high quality astrometric microlensing events generated from simulations. The vertical error bar associated with each bin is proportional to the square root of events in the bin. The horizontal error bar is the size of the bin.

### 6.5.2 Determination of the local mass function

Gaia is the first instrument to have the capabilities of detecting nearby populations of very dark objects. For example, local populations of low mass ($\sim 0.5 M_\odot$) black holes could easily have eluded identification thus far. Cool halo white dwarfs are also extremely difficult to detect. Existing programs look for faint objects with high proper motions characteristic of halo populations (e.g., Oppenheimer et al. 2001). Such programs miss stars with low space motions and have difficulties detecting stars with extremely high proper motions (depending on the epoch difference of the plates). So, they can only set lower limits to the local halo white dwarf density. Samples of disk white dwarfs are again selected kinematically and are subject to similar biases (Knox, Hawkins & Hambly 1999). There may remain undetected a larger population of even fainter and cooler white dwarfs, as it is unclear whether existing surveys are probing the very faintest luminosities possible. Similarly, there may be an extensive local population of very cool brown dwarfs. The *2 Micron All Sky Survey* (2MASS) and the *Sloan Digital Sky Survey* (SDSS) have increased the known population of local dwarf stars with spectral types later than M to over a hundred (e.g., Strauss et al. 1999, Burgasser et al. 2000, Gizis, Kirkpatrick & Wilson 2001). Nonetheless, the coolest brown dwarfs will have easily eluded the grasp of these and all current surveys. Future projects like the *Space Infrared Telescope Facility* (SIRTF) may be able to detect very old brown dwarfs in the solar neighbourhood by using long integration times, but a large-scale survey will be prohibitively costly in terms of time. However, the astrometric microlensing signal seen by Gaia will be sensitive to local populations of even the dimmest of stars and darkest of these objects.

Here, we investigate whether we can recover the local mass function (MF) from the astrometric microlensing signal seen by Gaia and supplemented by ground-based photometry (Strategy 3). We begin by examining the selection effects in the subsample of high quality events, the only ones for which individual lens masses can be recovered to reasonable accuracy. The lenses of the high quality events are biased towards masses greater than $0.3M_\odot$. This is not too surprising, as it is more difficult to recover the relative parallax if the Einstein radius is small. Gaia's astrometric microlensing signal will be an unbiased and powerful probe of the local population of stellar remnants, such as white dwarfs and neutron stars. However, the signal seen on smaller mass-scales will required modelling and correction for selection effects before it is unbiased.

Reid & Hawley (2000) compute the mass function (MF) for nearby stars from the volume-limited *8 Parsec Sample* using empirical mass-luminosity relationships. They obtain a power-law MF ($f(M) \propto M^{-1}$) over the range 0.1 to $1.0M_\odot$. This is in rough agreement with the MF as inferred from studies of the LF of red disk stars seen with *Hubble Space Telescope* (Gould, Bahcall, Flynn 1997), which is a broken power-law. Above $\sim 0.6M_\odot$, the MF is nearly of the classical Salpeter form with $f(M) \propto M^{-2.21}$. Below $0.6M_\odot$, it is flatter than Salpeter with $f(M) \propto M^{-0.9}$ (after correction for binaries). Of course, the behaviour of the MF becomes more uncertain as the hydrogen-burning limit is approached.

We use the three MFs shown in Figure 6.14 as spanning a range of reasonable possibilities. Above $0.5M_\odot$, the MF is always derived from the Reid-Hawley luminosity function. Below $0.5M_\odot$, there are three possibilities. It may be flat ($f(M) \propto M^{-1}$), rising ($f(M) \propto M^{-1.44}$) or falling ($f(M) \propto M^{0.05}$). These choices are motivated by the Reid-Hawley LF as shown in Figure 6.13. For the falling MF, we choose the power-law index to be that implied by the decline in the LF below $M_G \approx 13$. For the rising MF, we choose the power-law index by assuming that the rise at $M_G \approx 11$ continues to fainter magnitudes and that these stars are missing from the data because of incompleteness. Of course, the flat MF is so called because it has equal numbers of objects in each decade of mass and so appears flat in a plot of $\log Mf(M)$ versus $\log M$. For each of the three MFs, we generate samples of 25000 astrometric microlensing events using Monte Carlo simulations. We extract the high quality events and compute the mass uncertainty using the covariance analysis. (In actual practice, the high quality events would be selected on the basis of the goodness of their $\chi^2$ fits). We build up the MF as a histogram. The vertical error bar associated with each bin is proportional to the square root of events in the bin. The horizontal error bar is the size of the bin.

The three cases are shown in Figure 6.18 with the solid line representing the underlying MF. The simulated datapoints with error bars show the MFs reconstructed from the high quality events. It is evident that Gaia can easily distinguish between the flat, rising and falling MFs. The MFs are reproduced accurately above $\sim 0.3 M_\odot$. Below this value, the reconstructed MFs fall below the true curves, as a consequence of the bias against smaller Einstein radii. However, this does not compromise Gaia's ability to discriminate between the three possibilities. In practice, of course, simulations could be used to re-calibrate the derived MFs at low masses and correct for the bias.

We have also carried out simulations with MFs containing spikes of compact objects, such as populations of $\sim 0.5 M_\odot$ white dwarfs. They lie in the mass régime to which Gaia's astrometric microlensing signal is most sensitive. So, such spikes stand out very clearly in the reconstructed MFs. We conclude that one of the major scientific contributions that Gaia can make is to determine the local MF. Microlensing provides the only way of measuring the masses of individual objects irrespective of their luminosity. Gaia is quite simply the best survey instrument to carry out an inventory of masses in the solar neighbourhood.

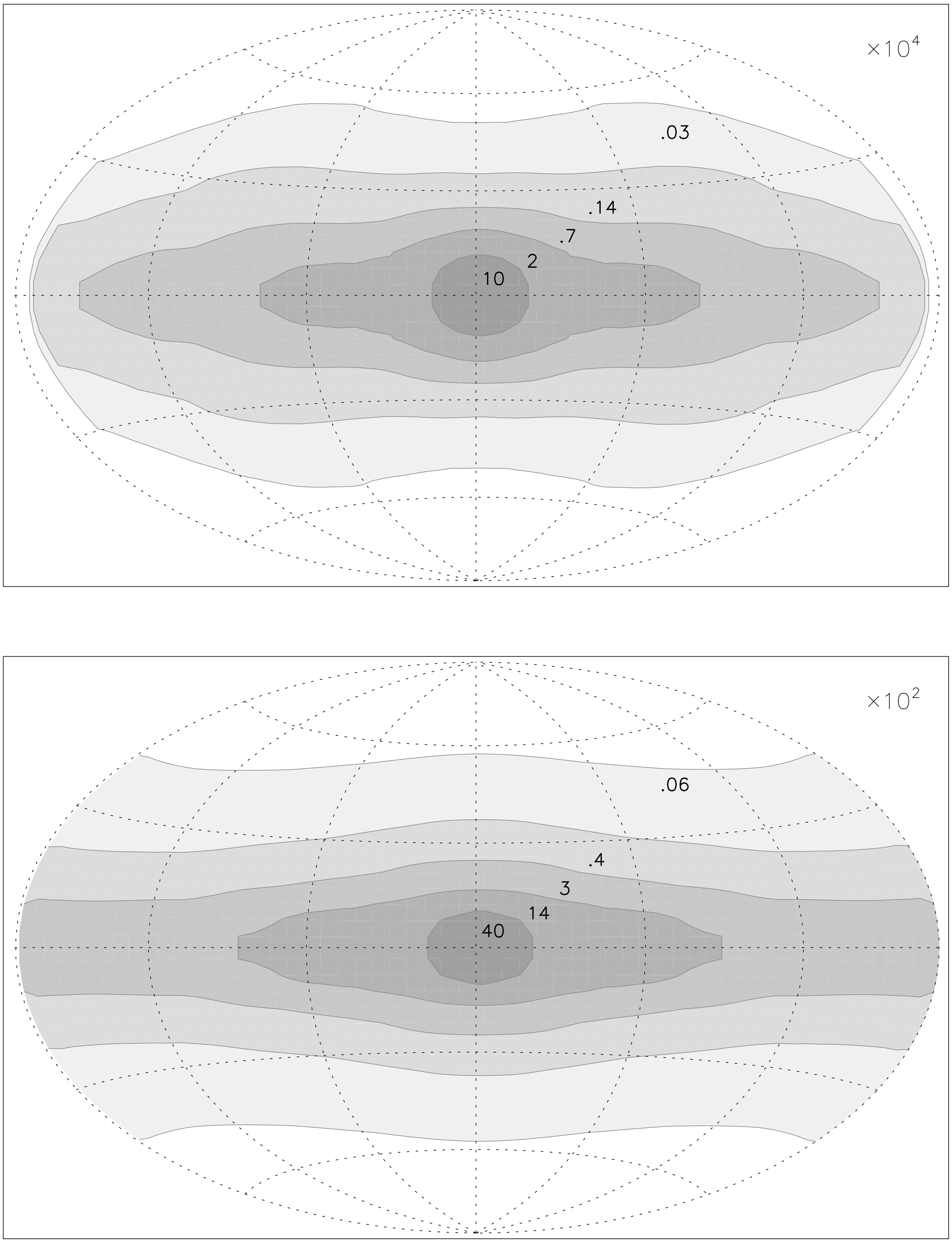


Figure 6.19: This shows contours of "microlensing noise" in astrometry (upper panel) and photometry (lower panel). The number within each contour refers to the total number of stars inside the shaded region enclosed between the contours that suffer an astrometric distortion or photometric brightening exceeding the mission target accuracy. The numbers are in units of $10^4$ in the upper panel and $10^2$ in the lower panel.

## 6.6 Implementation

### 6.6.1 Detection of events

All sources detected by Gaia will be fit using the standard algorithms for the 6 astrometric parameters, namely $\boldsymbol{\theta}_{\mathrm{s},0}$, $\boldsymbol{\mu}_{\mathrm{s}}$ and $\mathbf{P}_{\mathrm{s}}$. This is described in, for example, volumes 1 and 3 of *The Hipparcos and Tycho Catalogues* (ESA 1997). So, the first cut on the dataset is to ask for large residuals in the standard astrometric parameters. Of course, microlensing is just one cause of large residuals out of many. Other possibilities include multiple companions, eclipsing systems, the mottled or spotted surfaces of stars and variability-induced movers or VIMs (Wielen 1996). VIMs were first discovered in *Hipparcos* data, as they give spurious negative parallaxes when fit to the standard astrometric model. In VIMs, it is hypothesised that the photometric centre of a close double star moves on the sky as one of the components has variable luminosity.

Suppose we detect the event photometrically as well as astrometrically. Then, Gaia's spectroscopy and multicolour photometry can help us distinguish microlensing events from other possible causes of astrometric shifts. Gaia's spectroscopy is reasonably accurate for objects brighter than $V \sim 15$, although it covers a short wavelength range near the Ca triplet. For objects fainter than $V \sim 15$, Gaia's mulicolour photometry will be more useful. If the lens is dark, then the colours before, during and after the microlensing event are the same. Such is not true of spotted stars, VIMs and resolved binaries, which will show colour changes over the course of time. If the lens is luminous, then the colour does change over the course of the microlensing event. However, Gaia will detect such a luminous lens and so the lens proper motion and parallax will be available from a standard astrometric fit. This means that we can correct for the gravitational deflection of the source directly from the data. The multicolour photometry can also help us reduce the false detection rate. An unblended microlensing event is achromatic and does not repeat, whereas most other types of variability are chromatic and do repeat. Even long-period variables have periods of at most $\sim 600$ days (Cox 2000) and thus are short enough for Gaia to recognise as repeating.

In propitious circumstances, close companions can be distinguished from microlensing by analysis of the rate of change of the astrometric excursion with time. At times far from the closest approach, the source motion is slow in a microlensing event, whereas at or near the closest approach, the source rapidly traverses the perturbation ellipse. Although a nearby companion also causes an elliptical distortion to be superposed on the proper and parallactic motion, the traversal is harmonic in time and repeats. A close companion will also induce radial velocity variations, which may be detectable with Gaia's spectroscopy. If the stars in the binary are of similar luminosity but different colour, then there may be color variations during the centroid motion as well.

If the closest approach, which corresponds to the maximum astrometric deviation, does not occur during the lifetime of the Gaia mission, then it will be difficult to be certain that the centroid shift is caused by microlensing. This is why, in this Chapter, we have restricted attention only to events which satisfy the stringent criteria of a $5\sqrt{2}\sigma_{\rm a}$ variation in the centroid shift and a maximum during the mission lifetime.

Can Gaia trigger detection of microlensing events on the basis of the astrometry only? This is a real challenge. Gaia provides a one-dimensional stream of astrometric data, and so must operate for roughly two years to gain enough accuracy on parallactic motions. After two years, preliminary astrometric fits may be constructed, but their accuracy will be limited. The best opportunities for detecting events will come in the latter part of the mission, when the iterative astrometric solution becomes more accurate. Hence, there is a need for at least one dedicated 1m class telescope (or better still a world-wide network of such telescopes) to monitor fields in the bulge and spiral arms so that the datasets can be correlated with Gaia's database. The error is reduced by typically better than a

| $u_0$ | 0.25 | 0.5 | 1 | 5 |
|---|---|---|---|---|
| % error | 0.28 | 0.26 | 0.22 | 0.14 |

Table 6.4: This table lists the percentage error in the estimated point spread function against the impact parameter of the microlensing event.

factor of 10 when astrometric data is supplemented by densely-sampled lightcurves from the ground (see also Gould & Salim 1999).

### 6.6.2 Noise caused by microlensing

"Microlensing noise" is the name given to the weak effects of typically large impact parameter microlensing events. This can cause fluctuations in the positions of stars. There is some analogy with the effects of turbulence in the upper atmosphere, which causes wavefronts to become corrugated and hence causes sources to blur and twinkle. Microlensing noise is a fundamental limit to the accuracy to which we can know the positions of sources. For example, Sazhin et al. (1998, 2001) have pointed out that fluctuations of the angular positions of reference extragalactic radio and optical sources will be caused by the microlensing effects of stars in the Galaxy. Such angular fluctuations may range up to hundreds of microarcseconds. Sazhin et al. (1998) found a good example of a quasar with large positional uncertainties caused by the lensing effects of a nearby *Hipparcos* star; the distance of the star is very close, just 50 pcs.

Figure 6.19 shows a contour plot of number of sources which have an astrometric or photometric variation caused by microlensing of the same order of magnitude as the mission target accuracy. (Let us recall the mission target accuracy is that achieved at the end of the mission and so is the instantaneous astrometric accuracy given in the final line of Table 6.1 divided by $\sim 10$). The total number of sources having an astrometric deviation exceeding the mission target accuracy is $1.2 \times 10^5$. Many of these events will be long duration events. Any astrometric deviation will often be only slowly varying over the mission lifetime and so this will not compromise the proper motion and parallax target accuracies for Gaia. For photometry, the instantaneous number of stars affected by microlensing noise is $\sim 5.9 \times 10^3$.

Another way in which the microlensing noise manifests itself is in distortion of the point spread function (PSF). Gaia's PSF may be approximated as a biaxial Gaussian with FWHM of 300 mas and 150 mas. To investigate the likely size of the errors, we convolve the PSF with the two micro-images corresponding to an event with Einstein radius $\theta_{\rm E} = 5$ mas. These micro-images are taken as pure $\delta$-functions. The convolved PSF is then fit with the standard biaxial Gaussian. This procedure of course carries an error, which we estimate by computing the area difference between the true PSF and the fit. This is divided by the area under the PSF to give the fractional error caused by microlensing. Table 6.4 list the percentage error as a function of impact parameter. Although the error is small, it will be important as Gaia is aiming for a photometric accuracy of fractions of a percent.

## 6.7 Conclusions

Gaia is an ambitious astrometric survey satellite that is planned for launch no later than 2012 by the European Space Agency (see ESA 2000; Perryman et al. 2001). Gaia scans the whole sky, performing multi-colour and multi-epoch photometry and spectroscopy, as well as astrometry. The reference frame is tied to a global astrometric reference frame defined by extragalactic objects. For bright sources, Gaia has the capabilities to perform individual astrometric measurements with microarcsecond accuracy. Even for objects as faint as $V \approx 20$, the positions, proper motions and parallaxes will be recovered to within at worst a few hundred microarcsecs at the end of the mission.

Gaia can measure microlensing by the small excursions of the light centroid that occur during microlensing. We use a stringent definition of an astrometric microlensing event as one with a significant variation ($5\sqrt{2}\sigma_{\rm a}$) of the centroid shift, together with a closest approach during the lifetime of the Gaia mission. The all-sky averaged astrometric microlensing optical depth is $\sim 1.5 \times 10^{-5}$. This means that $\sim 15000$ sources will exhibit astrometric microlensing events with such characteristics during the course of the mission. Gaia can also measure microlensing by the photometric brightening that accompanies low impact parameter events. The all-sky averaged photometric optical depth is $\sim 5 \times 10^{-7}$, so there are $\sim 7500$ photometric microlensing events during the five year mission lifetime, most of which have only a few datapoints because of the poor sampling. However, these measurements are of a great importance.

Let us again emphasise that these numbers only refer to numbers of microlensing events with specified characteristics. Any statement as to the actual number of microlensing events that Gaia will find must take into account the number of false detections thrown up by the identification algorithm.

Our event statistics refer to the signal provided by stellar lenses in the Galactic disk and bulge. We have not taken into account dark objects in the halo (popularly called Machos). This is reasonable, as the cross-section for astrometric microlensing favours nearby lenses. The most valuable events are those for which the Einstein crossing time $t_{\rm E}$, the angular Einstein radius $\theta_{\rm E}$ and the relative parallax of the source with respect to the lens $\pi_{\rm rel}$ can all be inferred from Gaia's datastream. The mass of the lens then follows directly. If the source distance is known – for example, if Gaia itself measures the source parallax – then a complete solution of the microlensing parameters is available. Of these quantities, it is the relative parallax that is the hardest to obtain accurately. A covariance analysis is used to follow the propagation of errors and establish the conditions for recovery of the relative parallax. This happens if the angular Einstein radius $\theta_{\rm E}$ is large and the Einstein radius projected onto the observer plane $\tilde{r}_{\rm E} \sim 1$ au so that the Earth's motion about the Sun gives a substantial distortion. It is also aided if the source is bright so that Gaia's astrometric accuracy is high and if the duration of the astrometric event is long so that Gaia has time to sample it fully. These conditions favour still further lensing populations that are very close.

Gaia measurements alone will provide a sample of at least 500 stars with accurately determined masses. However, the numbers can be improved still further if Gaia observations are supplemented with ground-based photometry. The total of 1000 masses will be measured with the help of dedicated telescopes on the ground.

Monte Carlo simulations are used to establish the characteristics of the $\sim 7\%$ of events for which Gaia can recover the mass of the lens to good accuracy. The typical lens distance is $< 2$ kpc and the typical source distance is $\sim 6$ kpc. The highest quality events seen by Gaia are dominated by local lenses.

We conclude that one of the major scientific contributions of microlensing studies with Gaia will be the determination of the mass function in the solar neighbourhood. Of course, direct mass measurements are presently possible just for binary stars with well-determined orbits. Microlensing is the only technique which can measure the masses of individual stars. Gaia is the first instrument with the ability to survey the astrometric microlensing signal provided by nearby lenses. We have used Monte Carlo simulations to show that Gaia can reconstruct the mass function in the solar neighbourhood from the sample of its highest quality events. This works particularly well for masses exceeding $\sim 0.3M_\odot$. Below $0.3M_\odot$, the reconstructed mass function tends to underestimate the numbers of objects, as the highest quality events are biased towards larger angular Einstein radii.

If there are local populations of low mass black holes, or very cool halo and disk white dwarfs or very old brown dwarfs, then they will have easily eluded detection with available technology. However, the astrometric microlensing signal seen by Gaia will be sensitive to local populations of even the dimmest of these stars and the darkest of these objects. Gaia is the first instrument that has the potential to map out and survey our darkest neighbours.

## 6.8 Bibliography


Alcock C. et al. 1997, ApJ, 486, 697

Aubourg E. et al. 1995, AA, 301, 1

Aurière M. et al. 2001, ApJ, 553, L137

Bahcall J.N., Soneria R.M., 1980, ApJS, 44, 73

Binney J.J., Gerhard O.E., Stark A.A., Bally J., Uchida K.I. 1991, MNRAS, 252, 210

Binney J.J., 2000, In "Microlensing 2000: A New Era of Microlensing Astrophysics", eds J.W. Menzies, P.D. Sackett.

Boden A.F., Shao M., van Buren D., 1998, ApJ, 502, 538

Boutreux T., Gould A., 1996, ApJ, 462, 705

Burgasser A.J. et al. 2000, AJ, 120, 1100

Chen B., Vergely J.L., Valette B., Carraro G., 1998, A&A, 336, 137

Cox J.P., 2000, Allen's Astrophysical Quantities, (Springer-Verlag: New York)

D'Antona F., Mazzitelli I., 1994, ApJS, 90, 467

Dehnen W. & Binney J., 1998, MNRAS, 298, 387

Dominik M., Sahu K.C. 2000, ApJ, 534, 213

Edvardsson B., Andersen J., Gustafsson B., Lambert D.L., Nissen P.E., Tomkin J. 1993, A&AS, 102, 603

ESA 1997, The Hipparcos and Tycho Catalogues, ESA SP-1200 (ESA Publications: Noordwijk)

ESA 2000, GAIA: Composition, Formation and Evolution of the Galaxy, Technical Report ESA-SCI(2000)4

Evans N.W., 1994, ApJ, 437, L31

Evans N.W., 1995, ApJ, 445, L105

Evans N.W., Kerins E.J., 2000, ApJ, 529, 917

Gizis J.E., Kirkpatrick J.D., Wilson J.C. 2001, AJ, 121, 2185

Gould A., 1995, ApJ, 441, 77

Gould A., 2000, ApJ, 542, 785

Gould A., Bahcall J.N., Flynn C., 1997, ApJ, 482, 913

Gould A., Salim S., 1999, ApJ, 524, 794

Griest K., 1991, ApJ, 366, 412

Häfner R.M., Evans N.W., Dehnen W., Binney J.J., 2000, MNRAS, 314, 433

Høg E., Novikov I.D., Polnarev A.G. 1995, A&A, 294, 287

Holmberg J., Flynn C., 2000, MNRAS, 313, 209

Kent S.M., 1992, ApJ, 387, 181

Kerins E., Carr B.J., Evans N.W., Hewett P., Lastennet E., Le Du Y., Melchior A.-L., Smartt S., Valls-Gabaud D., 2001, MNRAS, 323, 13

Kiraga M., Paczyński B., 1994, ApJ, 430, L101

Knox R.A., Hawkins M.R.S., Hambly N.C. 1999, MNRAS, 306, 736

Kroupa P., Tout C.A., Gilmore G. 1993, 262, 545

Lindegren L., 1998, Simulation of Gaia's scanning of arbitrary directions (SAG-LL-026), unpublished

McGinn M.T., Sellgren K., Becklin E.E., Hall D.N.B. 1989, ApJ, 338, 824

Miralda-Escudé J. 1996, ApJ, 470, L113

Mihalas D., Binney J., 1981, Galactic Astronomy, (Freeman: San Francisco)

Oppenheimer B.R., Hambly N.C., Digby A.C., Hodgkin S.T., Saumon D., 2001, Science, 292, 698

Paczyński B. 1996, Acta Astron, 46, 291

Perryman M.A.C. et al. 2001, AA, 369, 339

Press W.H., Teukolsky S.A., Vetterling W.T., Flannery B.P., Numerical Recipes: The Art of Scientific Computing, (Cambridge University Press: Cambridge), chap 7.

Reid I.N., Hawley S., 2000, New Light on Dark Stars (Springer Verlag: New York), chaps 7, 8.

Saha P., 2003, *Principles of Data Analysis*, Cappella Archive

Sahu K.C., 1994, Nature, 370, 275

Sandage A., 1972, ApJ, 178, 1

Sazhin M.V., Zharov V.E., Volynkin A.V., Kalinina T.A. 1998, MNRAS, 300, 287

Sazhin M.V., Zharov V.E., Kalinina T.A. 2001, MNRAS, 323, 952

Sivia D.S., 1996, *Data Analysis: A Bayesian Tutorial*, Oxford University Press,

Strauss M.A. et al. 1999, ApJ, 522, L61

Udalski D., Szymanski M., Kaluzny J., Kubiak M., Mateo M, Krzeminski W. 1994, ApJ, 426, L69

van der Kamp P., 1967, Principles of Astrometry, (Freeman: San Francisco), p. 41.

Walker M.A. 1995, ApJ, 453, 37

Wielen R., 1996, AA, 314, 679

Zhao H.S., Evans N.W., 2000, ApJ, 545, L35

# Chapter 7

# Conclusions and Future Prospects

Variability research is entering a new era of ever more powerful instruments and ever more un-manageably vast catalogues. There is a need for a re-assessment of the current data analysis techniques and for the development of new methods. We have considered the problems of object detection, datastream simulation and information extraction in big samples of transient events. Microlensed stars and supernovae provided the examples of rare objects that – if detected in ample amounts – have the potential to provide information invaluable for our understanding of the universe. The methods were applied to the data from one successful survey that just finished its operation (MACHO) and one future ambitious project (Gaia). The main conclusions are summarized below.

## 7.1 Conclusions and summary

Chapter 2 introduces neural networks as a fast and automatic way of classifying lightcurves in massive photometric datasets. As an example, we provide a working neural network that can distinguish microlensing lightcurves from other forms of variability, such as eruptive, pulsating, cataclysmic and eclipsing variable stars. The network has five input neurons, a hidden layer of five neurons and one output neuron. The five input variables for the network are extracted by spectral analysis from the lightcurve datapoints and are optimised for the identification of a single, symmetric, microlensing bump. The output of the network is the posterior probability of microlensing. The committee of neural networks successfully passes tests on noisy data taken by the MACHO collaboration. When used to process $\sim 5000$ lightcurves on a typical tile towards the bulge, the network cleanly identifies the single microlensing event. When fed with a sub-sample of 36 lightcurves identified by the MACHO collaboration as microlensing, the network corroborates this verdict in the case of 27 events, but classifies the remaining 9 events as other forms of variability. For some of these discrepant events, it looks as though there are secondary bumps or the bump is noisy or not properly contained. Neural networks naturally allow for the possibility of novelty detection – that is, new or unexpected phenomena which we may want to follow up. The advantages of neural networks for microlensing rate calculations, as well as the future developments of massive variability surveys, are both briefly discussed.

In Chapter 3 we present two neural networks for the identification of microlensing events towards the LMC – the first detects all single-bump burst-like transients on the background of variable stars and the second distinguishes microlensing from supernovae. The inputs to the networks include parameters describing the shape and the size of the lightcurve, together with colour of the event. The network computes the posterior probability of microlensing, together with an estimate of the likely error. We propose an algorithm for direct calculation of the microlensing rate from the output of the neural networks. With the cascade of networks we re-analyze the microlensing dataset towards the Large Magellanic Cloud. The neural networks confirm the microlensing nature of only 9 of the possible 17 events identified by the MACHO collaboration. We compute upper and lower limits to the optical depth towards the LMC, which must lie in the range $3 - 8 \times 10^{-8}$. This optical depth estimate is lower by at least a factor of $\sim 2$ than claimed previously. It can be supplied by the known stellar populations in the outer Galaxy and implies that none of the dark halo is built from compact objects.

Is gravitational microlensing compatible with Galactic structure? In an attempt to answer this question in Chapter 4 we produce large-scale maps of the microlensing optical depth and the average timescale. The maps are constructed for a number of models of the galactic bar and disk, incorporating the effects of spiral structure. Freudenreich's model can reproduce the high optical depths towards the Bulge. Spiral structure tends to increase the optical depth by $\lesssim 20\%$ and the mean timescale by $\lesssim 100\%$. Different bar morphologies give characteristically different shaped contours, especially at low Galactic latitudes ($|b| < 2°$). These could be traced out with a K band microlensing survey, consuming $\sim 100$ minutes per night on a telescope like VISTA.

Gaia is the "super-*Hipparcos*" satellite scheduled for launch in 2010 by the European Space Agency. It is a scanning satellite that carries out multi-colour, multi-epoch photometry on all objects brighter than 20th magnitude. In Chapter 5 we conduct detailed simulations of supernovae (SNe) detection by Gaia. Supernovae of each type are chosen according to the observed distributions of absolute magnitudes, and located in nearby galaxies according to the local large-scale structure. Using an extinction model of the Galaxy and the scanning law of the Gaia satellite, we calculate how many SNe are detectable as a function of the phase of the lightcurve. Our study shows that Gaia will report data on $\sim 21\,400$ SNe during the five-year mission lifetime, of which $\sim 14\,300$ are SNe Ia, $\sim 1400$ are SNe Ib/c and $\sim 5700$ are SNe II. Using the simulations, we estimate that the numbers caught before maximum are $\sim 6300$ SNe Ia, $\sim 500$ SNe Ib/c and $\sim 1700$ SNe II. During the mission lifetime, Gaia will issue about 5 SNe alerts a day. The most distant SNe accessible to Gaia are at a redshift $z \sim 0.14$ and so Gaia will provide a huge sample of local SNe. There will be many examples of the rarer subluminous events, over-luminous events, SNe Ib/c and SNe II-L. SNe rates will be found as a function of galaxy type, as well as extinction and position in the host galaxy. Amongst other applications, there may be about 26 SNe each year for which detection of gravitational waves is possible and about 180 SNe each year for which detection of gamma-rays is possible. Gaia's astrometry will provide the SN position to better than milliarcseconds, offering opportunities for the identification of progenitors in nearby galaxies and for studying the spatial distribution of SNe of different types in galaxies.

Chapter 6 presents a detailed study of microlensing capabilities of the Gaia satellite. Gaia can measure microlensing by the brightening of source stars. For the broad G band photometer, the all-sky source-averaged photometric optical depth is $\sim 5 \times 10^{-7}$. There are $\sim$ 5000 photometric microlensing events for which Gaia will measure at least one datapoint on the amplified lightcurve. Gaia can also measure microlensing by the small excursions of the light centroid that occur during events. The all-sky source-averaged astrometric microlensing optical depth is $\sim 1.5 \times 10^{-5}$. Some $\sim$ 15000 sources will have a significant variation of the centroid shift, together with a closest approach, during the lifetime of the mission. A covariance analysis is used to study the propagation of errors and the estimation of parameters from realistic sampling of the Gaia datastream of transits in the along-scan direction during microlensing events. The mass of the lens can be calculated to good accuracy if the lens is nearby so that angular Einstein radius $\theta_{\rm E}$ is large; if the Einstein radius projected onto the observer plane $r_{\rm E}$ is about one astronomical unit; if the duration of the astrometric event is long ($\gtrsim$ 1 year) or if the source star is bright. Monte Carlo simulations are used to study the $\sim$ 1000 events for which the mass can be recovered with an error of $< 50\%$. These high quality events are dominated by disk lenses within 1 kiloparsec and source stars within a few kiloparsecs. We show that the local mass function can be recovered from the high quality sample to good accuracy. Gaia is the first instrument with the capabilities of measuring the mass locally in very faint objects like black holes and very cool white and brown dwarfs. For less than $\sim 10\%$ of all astrometric events will Gaia record $> 10$ photometric datapoints. There is a need for a dedicated telescope that densely samples the Galactic Centre and spiral arms, as this can improve the accuracy of parameter estimation by a factor of $\sim 10$. The total number of sources that have an astrometric microlensing variation exceeding the mission target accuracy is $\sim 10^5$.

## 7.2 Future work

Let us discuss some projects that are closely related to the work presented in this thesis.

### 7.2.1 Object classification with neural networks

We envisage that one of the many possible applications of supervised learning techniques will be the identification of planetary transit events. The essential component of the presently available detection methods is a cross-correlation analysis. This normally proceeds by generating a noise-free multi-transit signal for a lag of transit periods. In the likely event of the star being a binary, the configuration of the transit lightcurve becomes quite complicated and the search for the matched filter has to be performed in a two-dimensional space. Since the same procedure is required for $\sim 50\%$ of monitored stars, the method does not seem to be efficient enough. When using neural networks, the parameter space is searched once – during the training process. Once trained, the network generalizes from the data in the training set and gives the answer for a candidate immediately. It is important to note that conventional algorithms assume the star to be variability-quiet, i.e. the signal under investigation consists of a constant baseline with dips corresponding to planet transits plus added random noise. A more general and realistic model should allow for stellar oscillations of different frequencies and amplitudes to be mixed with the transit signal or for the surface of the star to be mottled with star-spots, and so on. It has been claimed that weak levels of stellar variability do not degrade detection efficiency in traditional methods. However, clearly these algorithms become inefficient for substantial stellar variability (i.e. require significantly larger planet radius for secure detection). With a neural network detector, however, we can be just as confident in identifying complex lightcurve candidates, provided we have enough astroseismological data in the training set.

Neural networks (or similar techniques) can be trained to process simultaneously photometric and astrometric data. The classification of photometric lightcurves and astrometric shifts for the Gaia survey presents a challenge since the temporal sampling of measurements is substantially uneven and the originally two-dimensional path of the star is recorded as a time series of one-dimensional astrometry. Neural networks can be used to distinguish between gravitational microlensing events and eclipsing systems, spotted stars and variability-induced movers. It will be interesting to analyze the efficiency of the neural network performance system on the sparsely-sampled data (the typical distance between consecutive observations is such that the most of the microlensing event can be easily missed in photometry). The photometry and astrometry on variable stars recorded and identified during the Hipparcos mission will also be useful as it will help to understand the characteristics of the future Gaia data processing.

The analysis of quasar lightcurves as well as quasar identification techniques could be enhanced with the introduction of neural networks. Most of the quasars vary; indeed optical variability is one of their characterizing features. Apart from the violent BL Lac objects flaring in the fast mode ($\sim$ 1 day) the majority of photometrically active QSOs exhibits modest amplitude variations on timescales of weeks to years. This variability has been studied by many groups (e.g. Hawkins 2002) as a means of constraining the nature of the QSO central engine, yet with a little success. For example, no consensus has been reached on the issue of lightcurve variations longer than 1 year. These long timescale light changes can be accounted for by instabilities in accretion discs around massive black holes or alternatively by microlensing by intervening dark objects. One property of QSO variability is established with a fair degree of confidence: it is aperiodic and is increasing with timescale. This fact has been employed as a selection criterion in the search for QSOs behind SMC and LMC within OGLE-II monitoring program. (Standard quasar finding methods have had rather limited results towards the Magellanic Clouds. Most of the QSO surveys avoid this region entirely due to crowding, significant dust extinction etc. Thus very few quasars are known in the direction of the SMC and the LMC, resulting in the lack of a suitable reference frame for proper motion measurements of the Clouds.) Structure functions are calculated to quantify the variability at different time-lags. Then the set of candidates pre-selected through cuts on the color-magnitude diagram is refined by applying the cut on the slope of the variogram. The actual algorithm utilized by the OGLE team required QSO variability rate $> 0.1$ for the lag $< 100$ days. This threshold is a typical example of an oversimplified decision boundary. It generates small number of false detections in the case of Gaussian noise or short periodic signals, but fails completely when presented with a Mira (period $> 200$ days) lightcurve variogram. A committee of simple neural networks with one processing (hidden) unit will perform better just by modelling the envelope of the structure functions in the training set. It is yet more advantageous to supply the network with the information on variability in different passbands (e.g. Welch-Stetson variability index).

The neural networks introduced in Chapters 2 and 3 can detect the simplest forms of microlensing events, when the lens can be approximated as a single point mass. This turns out to be the most important case for surveys like MACHO. It is interesting to extend the existing networks to permit detection of exotic microlensing events. This includes distortions caused by parallactic or finite-source size effects or by binarity and so. Importantly, some of the most ambitious ongoing microlensing experiments are working in the highly blended régime, sometimes called “pixel lensing”. For example, the POINT-AGAPE (Paulin-Henriksson et al. 2002a,b) and MEGA (Crotts et al. 2000) collaborations are all monitoring the nearby galaxy M31. In contrast to classical microlensing, in pixel lensing the source stars are unresolved. The microlensing event is detected if one of the sources contained in the detector element undergoes a brightness change sufficient enough to rise above the noise level. Even traditional cuts such as the presence of one bump in the lightcurve or the goodness of fit to the standard microlensing lightcurve can not be applied to pixel lensing data. This is because a pixel can contain tens of thousands of stellar objects some, of which very many are likely to be variable. Additionally, the pixel data provides only the upper bit of the microlensing lightcurve, thus undermining any fitting procedure. As the variety of pixel lightcurves is so enormous, it is crucial to harness the power of the neural network approach.

### 7.2.2 Astrometric microlensing on neutron stars

Little is known about the population of neutron stars in the Galaxy. The mass of an isolated neutron star has never been measured. In principle, it is possible to constrain the mass-radius ratio by measuring the gravitational redshift (Cottam, Paerels & Mendez 2002). The only neutron stars for which the mass has been measured are those in binary systems, in which one of the components is either a radio pulsar or an X-ray pulsar (e.g., Bahcall 1978; Shapiro & Teukolsky 1983; Thorsett & Chakrabarty 1999). Here, the mass is determined by application of Kepler's Third Law. This requires independent estimates of the mass of the companion star and the inclination of the orbital plane.

The total number of neutron stars in the Galaxy is also uncertain. Lyne, Manchester & Taylor (1985) estimated the density profile and luminosity function of radio pulsars from a local sample. They reckoned that the total number of pulsars born during the lifetime of the Galaxy is between 1 and $4 \times 10^8$, assuming a constant birth rate. This is a lower limit to the number of neutron stars, because the birth rate was higher in the past and because some young neutron stars may be radio-quiet (e.g., Brazier & Johnstone 1999). By following the pre-supernovae evolution of stars in the Galaxy, the total population of all neutrons stars can be estimated as $1 \times 10^9$ (Timmes, Woosely

& Weaver 1996). Nonetheless, both the masses and numbers of neutrons stars are interesting. The mass provides a direct test of the equation of state of cold nuclear matter, itself controlled by the physics of strong interactions between the particles that compose the star. The masses of radio pulsars seem to be very tightly constrained about a central value of 1.35 $M_{\odot}$ (Thorsett & Chakrabarty 1999), though this may not be typical of the wider population. The number of neutron stars provides constraints on the star-formation history of the Galaxy and tests of the theory of stellar evolution.

Gravitational microlensing provides a unique way to detect any isolated, very dark object, such as a neutron star. The photometric effect, in which a background source brightens and fades as an intervening neutron star passes close to the line of sight, has a very low probability. Schwarz & Seidel (2002) showed that photometric microlensing optical depth for lensing by neutron stars is $\sim 10^{-8}$, some two orders of magnitude lower than that for lensing by main sequence stars towards the Galactic Centre. However, microlensing also causes an additional perturbation to the proper and parallactic motion of the source. This effect favours nearby and fast moving lenses. As neutron stars are kicked at birth out of the Galactic disk, the optical depth to astrometric microlensing is substantially greater than that to photometric microlensing. All this attains importance with the advent of the Gaia satellite. Similarly to Chapter 6, the maps of the astrometric optical depth in neutron stars can be constructed. We can estimate the likely number of events detected by Gaia with neutron stars as microlenses and investigate the possibility of deriving the masses of individual neutron stars. From this the total number of neutron stars in the Galaxy can be deduced.

## 7.3 Bibliography

Bahcall J.N. 1978, ARAA, 16, 241

Brazier K.T.S, Johnston S. 1999, MNRAS, 305, 671

Cottam J., Paerels F., Mendez M. 2002, Nature, 420, 51

Crotts A., Uglesich R., Gould A., Gyuk G., Sackett P., Kuijken K., Sutherland W., Widrow L. 2000, In "Microlensing 2000: A New Era of Microlensing Astrophysics", eds. J.W. Menzies and P.D. Sackett, ASP Conference Series, vol. 239, p. 318, ASP, San Francisco. (astro-ph/0006282)

Hawkins M.R.S., 2002, MNRAS, 329, 76

Lyne A., Manchester R.N., Taylor J.H. 1985, MNRAS, 213, 613

Paulin-Henriksson S. et al. 2002a, ApJ, 576, L121

Paulin-Henriksson S. et al. 2002b, astro-ph/0207025

Schwarz D.J., Seidel D. 2002, AA, 388, 483

Shapiro S.L., Teukolsky S.A., 1978, Black Holes, White Dwarfs and Neutron Stars, Wiley-Interscience, New York

Thorsett S.E., Chakrabarty D. 1999, ApJ, 512, 288

Timmes F.X, Woosley S.E., Weaver T.A. 1996, ApJ, 457, 834

# Appendix A

# Three models of the Galaxy

Here we provide the equations that describe the three models of the Galaxy exploited in Chapter 4.

Let $x$, $y$ and $z$ be the coordinates defined by the principal axes of the galactic bulge/bar, with $x$-axis directed along the long bar axis, which is at angle $\phi_0$ from the Sun-centre line. Then the following equations describe the distribution of the mass density $\rho$ ($\rho_b$ and $\rho_d$ refer to the density contributions of the bar and the disk correspondingly) in the Milky Way galaxy in the models of Binney et al., Freudenreich and Dwek et al.

In the model of Binney et al.:

$$\rho = \Upsilon_B j_0 (f_b + f_d) \tag{A.1}$$

$$f_b = f_0 \frac{e^{-a^2/a_m^2}}{(1 + a/a_0)^{1.8}} \tag{A.2}$$

$$f_d = \left( \frac{e^{-|z|/z_0}}{z_0} + \alpha \frac{e^{-|z|/z_1}}{z_1} \right) R_d e^{-R/R_d} \tag{A.3}$$

$$a = \left( x^2 + \frac{y^2}{\eta^2} + \frac{z^2}{\zeta^2} \right)^{1/2} \tag{A.4}$$

| Binney et al. | | Freudenreich | | Dwek et al. (E2) | |
|---|---|---|---|---|---|
| $\phi_0$ | $20°$ | $\phi_0$ | $14°$ | $\phi_0$ | $24°$ |
| $\Upsilon_B$ | $3.57\ \times 10^8 \frac{M_\odot}{COBE\mathrm{unit}}$ | $\Upsilon_F$ | $0.84\ \frac{M_\odot}{L_\odot}$ | $\rho_0$ | $4.46\ \frac{M_\odot}{\mathrm{pc}^3}$ |
| $j_0$ | $0.456\ \frac{COBEunits}{\mathrm{kpc}^3}$ | $I_b$ | $1300\ \frac{L_\odot}{\mathrm{pc}^2}$ | $\Sigma$ | $50\ \frac{M_\odot}{\mathrm{pc}^2}$ |
| $f_0$ | 624 | $(a_x, a_y, a_z)$ | (1.69, 0.63, 0.42) kpc | H | 0.325 kpc |
| $a_m$ | 3.82 kpc | $(c_\perp, c_\parallel)$ | (1.55, 3.43) | $R_d$ | 3.5 kpc |
| $a_0$ | 100 pc | $(R_{bar}, h_{bar})$ | (2.97, 044) kpc | $x_0$ | 900 pc |
| $z_0$ | 210 pc | $I_d$ | $867\ \frac{L_\odot}{\mathrm{pc}^2}$ | $y_0$ | 385 pc |
| $z_1$ | 42 pc | $R_d$ | 2.5 kpc | $z_0$ | 250 pc |
| $R_d$ | 2.5 kpc | $z_0$ | 167 pc | | |
| $(\eta, \zeta)$ | (0.3,0.3) | $R_h$ | 2.94 kpc | | |
| $\alpha$ | 0.27 | $(q_h, \beta)$ | (0.87, 1.72) | | |

Table A.1: This lists the values of the parameters in the Galactic models of Binney et al. (first column), Freudenreich (second column) and Dwek et al. (third column).

In the model of Freudenreich:

$$\rho = \Upsilon_F(j_b + j_d) \tag{A.5}$$

$$j_b = \frac{I_b}{a_z} sech^2(m_b) T(R) \tag{A.6}$$

$$j_d = \frac{I_d}{2z_0} sech^2(z/2z_0) e^{-R/R_d}(1 - e^{-m_h^\beta}) \tag{A.7}$$

$$m_h \equiv \sqrt{(x^2 + q_h^2 y^2)/R_h^2} \tag{A.8}$$

$$m_b \equiv \left\{ \left[ \left(\frac{|x|}{a_x}\right)^{c_\perp} + \left(\frac{|y|}{a_y}\right)^{c_\perp} \right]^{c_\parallel/c_\perp} + \left(\frac{|z|}{a_z}\right)^{c_\parallel} \right\}^{1/c_\parallel} \tag{A.9}$$

$$T(R) \equiv \begin{cases} 1, & \text{for } R \le R_{bar} \\ e^{-(R-R_{bar})^2/h_{bar}^2}, & \text{otherwise} \end{cases} \tag{A.10}$$

In the model of Dwek et al.:

$$\rho = \rho_b + \rho_d \tag{A.11}$$

$$\rho_b = \rho_0 e^{-r_D} \tag{A.12}$$

$$\rho_d = \frac{\Sigma}{2H} e^{-(R-R_\odot)/R_d} e^{-|z|/H} \tag{A.13}$$

$$r_D = \left[ \left(\frac{x}{x_0}\right)^2 + \left(\frac{y}{y_0}\right)^2 + \left(\frac{z}{z_0}\right)^2 \right]^{1/2} \tag{A.14}$$